Defect structure and optical properties of alkaline-earth fluorides

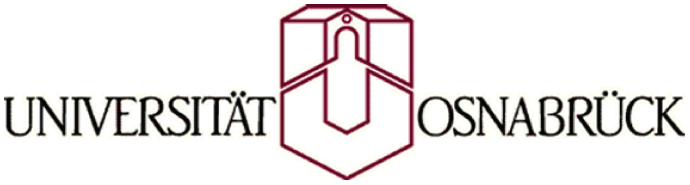

Hongting Shi

Thesis Advisor: Prof. Dr. Gunnar Borstel

Department of Physics

University of Osnabrück

A thesis submitted for the degree of

Doctor of Philosophy

February 2007

I would like to dedicate this thesis to my loving parents ...

Contents

List of Acronyms xvi

1 Introduction 1

2 Basic alkaline-earth fluorides: CaF_2 and BaF_2 3

2.1 Bulk crystals . . . 4
2.2 Defects in alkaline-earth fluorides . . . 8
2.3 Surfaces . . . 11
2.4 Motivation . . . 15

3 HF/DFT formalism and methodology 19

3.1 HF formalism . . . 20
3.1.1 Schrödinger equation . . . 20
3.1.2 The energy of a general polyelectronic system . . . 22
3.1.3 The Hartree-Fock equations . . . 22
3.1.4 The electron correlation . . . 23
3.2 Density functional theory . . . 25
3.2.1 Hohenberg-Kohn theorems . . . 25
3.2.2 Spin-polarized density functional theory . . . 28
3.2.3 Local density approximation . . . 28
3.2.4 Beyond the LDA: Gradient-corrected functionals . . . 30
3.3 Hybrid HF/DFT methods . . . 31

4 Calculations on perfect bulks and slabs of CaF_2 and BaF_2 crystals 35

4.1 Method of calculations . . . 36

4.2 Calculations on perfect CaF_2 and BaF_2 bulks 38
4.3 Calculations on perfect CaF_2 and BaF_2 slabs 46
4.3.1 Surface relaxations 46
4.3.2 Surface electronic structures 52
4.3.3 Surface energies 56

5 F centers in CaF_2 and BaF_2 bulks and the (111) slabs 61
5.1 Method of calculations 61
5.2 F centers in CaF_2 and BaF_2 bulks 62
5.3 M centers in CaF_2 and BaF_2 bulks 74
5.4 Surface F centers in CaF_2 and BaF_2 79

6 Oxygen-Vacancy dipoles in CaF_2 87
6.1 Method of calculations 87
6.2 OV dipoles in the CaF_2 bulk 88
6.2.1 Single OV dipole in the CaF_2 bulk 88
6.2.2 Aggregation of OV dipoles 95
6.3 OV centers at the CaF_2 (111) surface 97

7 Hydrogen centers in CaF_2 and BaF_2 103
7.1 Method of calculations 103
7.2 Hydrogen centers in CaF_2 and BaF_2 bulks 105
7.2.1 Calculated results for the H_s^- centers in CaF_2 and BaF_2 bulks 105
7.2.2 Calculated results for the H_i^0 centers in CaF_2 and BaF_2 bulks 110
7.3 Surface H_s^- centers in CaF_2 and BaF_2 115

8 H centers in CaF_2 and BaF_2 123
8.1 Method of calculations 123
8.2 Calculated results for the H centers in CaF_2 and BaF_2bulks . . . 124

9 Conclusions 133

A Spin-restricted/unrestricted Hartree-Fock theory **135**
A.1 The energy of a general polyelectronic system 135
A.2 Closed-shell systems 137
A.2.1 The energy of a closed-shell system 137
A.2.2 Linear combination of atomic orbitals (LCAO) in Hartree-Fock theory 138
A.2.3 The Roothaan-Hall equations 139
A.3 Open-shell systems 141
A.4 A tentative explanation to polarized band structures 144

Publications **147**

Acknowledgements **149**

References **151**

List of Figures

2.1 A cubic structure of an alkaline-earth fluoride with the formula unit MF_2, where M=Ca or Ba, and F is fluorine. The upper and lower figures correspond to T_d and O_h symmetries, respectively. . 5

2.2 Schematic band structure of a typical alkaline-earth fluoride. Using CaF_2 as an example [Rubloff (1972)]. 7

2.3 The structure of the $MF_2(111)$ surface in the top and side view. F1 and F2 indicate the fluorine atoms located at the upper and lower sublayers, respectively. 13

4.1 Charge density map of the CaF_2 bulk from the (110) side view calculated by means of the hybrid B3PW method. Isodensity curves are drawn from 0 to 0.1 e/bohr^3 with an increment of 0.001 e/bohr^3. 40

4.2 Electronic band structures of CaF_2 and BaF_2 bulks calculated by means of the hybrid B3PW method. 41

4.3 The calculated total and projected density of states (DOS) for CaF_2 and BaF_2 bulks by means of the hybrid B3PW method. . . 44

4.4 The calculated total and projected density of states (DOS) in deep energy range for the CaF_2 bulk by means of the hybrid B3PW method. 45

4.5 Schematic sketch of CaF_2 and BaF_2 (111) surface structures. Layer numbering introduced in this figure is used in Table 4.5. Arrows indicate the calculated displacement directions of Ca, Ba and F atoms. 47

4.6 Schematic sketch of the CaF_2 (110) surface structure. For the CaF_2 (110) surface, there appears an additional degree of freedom in the Y direction for atomic displacements. Layer numbering introduced in this figure is used in Table 4.6. Arrows indicate the calculated displacement directions of Ca and F atoms. 49
4.7 Schematic sketch of the CaF_2 (100) surface structure. Layer numbering introduced in this figure is used tin Table 4.7. Arrows indicate the calculated displacement directions of Ca and F atoms. . . 51
4.8 Electronic band structures of the (111), (110) and (100) CaF_2 slabs calculated by means of the hybrid B3PW method. 54
4.9 Projected density of states (DOS) for F p-orbitals in the (100) CaF_2 slab. 56
4.10 Projected density of states (DOS) for F p-orbitals in the (110) CaF_2 slab. 57
4.11 Projected density of states (DOS) for F p-orbitals in the (111) CaF_2 slab. 58

5.1 Electron charge (upper) and spin (lower) density maps of CaF_2 with an F center from the (110) side view. Isodensity curves are drawn from 0 e/bohr^3 to 0.1 e/bohr^3 with an increment of 0.001 e/bohr^3 for charge density and from -0.005 e/bohr^3 to 0.06 e/bohr^3 with an increment of 0.001 e/bohr^3 for spin density. Blue, green and red lines denote positive, negative and zero values, respectively. 64
5.2 A view of the F-center nearest-neighbor geometry in MF_2, with the indication of relaxation shifts. The position of the F center is indicated by XX. The fluorine atoms in the first shell are labeled 1, in the second shell 2 and in the third shell 3a and 3b. 66
5.3 Calculated band structure for the 48-atom supercell modeling the F center in CaF_2. α (left) and β (right) denote the majority and minority spin states, respectively. 68
5.4 Calculated band structure for the 48-atom supercell modeling the F center in BaF_2. α (left) and β (right) denote the majority and minority spin states, respectively. 69

5.5 Total and projected density of states (DOS) for the F center in the CaF_2 bulk. α and β denote the up- and down-spin states, respectively. 71
5.6 A view of the M-center nearest-neighbor geometry in CaF_2 and BaF_2 with indication of relaxation shifts. The positions of the anion vacancies are indicated by two squares. The directions of atomic displacements are shown with arrows, the values are given as % of the lattice constant in circles. 75
5.7 Charge density maps of CaF_2 and BaF_2 crystals with the periodic M center from the (1 1 0) (left) and (1 -1 0) (right) side views. Isodensity curves are drawn from 0 e/bohr^3 to 0.1 e/bohr^3 with an increment of 0.001 e/bohr^3. 76
5.8 Calculated band structures for the 96-atom supercell modeling the M centers in CaF_2 (upper) and BaF_2 (lower). 78
5.9 Schematic sketch of the (111) surface containing F centers. 80
5.10 A top view of the surface F-center nearest-neighbor geometry with the indication of relaxation shifts. The directions of atomic displacements are shown with arrows. 81
5.11 Calculated band structure for the 108-atom supercell modelling the surface F center in CaF_2. 84
5.12 Calculated band structure for the 108-atom supercell modelling the surface F center in BaF_2. 84

6.1 OV center in CaF_2 oriented along the (100) axis. The arrows show the directions of the atomic displacements surrounding the OV center, the displacement values are given in circles in % of the lattice constant $a_0 = 5.50$ Å. 89
6.2 Charge density map of a CaF_2 crystal with the periodic OV center from the (1 1 0) side view. Isodensity curves are drawn from 0 e/bohr^3 to 0.1 e/bohr^3 with an increment of 0.001 e/bohr^3. 91
6.3 A view of the OV center geometry with the indication of effective charges. 92

6.4 Calculated band structure for the 96-atom supercell modeling the OV center in the CaF_2 bulk. 93
6.5 Density of states (DOS) of the OV center in the CaF_2 bulk. . . . 94
6.6 Configurations of aggregations of the OV dipoles in the CaF_2 bulk. 96
6.7 Side view of the OV center placed at the CaF_2 (111) surface. The directions of atomic displacements in the (111) axis are shown with arrows. 97
6.8 Sketch of the OV center placed at the CaF_2 (111) surface. 98
6.9 Band structure of the OV center at the CaF_2 (111) surface for the V-O_1 case. 100

7.1 A view of the H_s^--center nearest-neighbor geometry with the indication of relaxation shifts. According to the symmetries of the atoms, different labels are defined in circles. 105
7.2 Charge density map of a CaF_2 crystal with the periodic H_s^- center from the (1 1 0) side view. Isodensity curves are drawn from 0 e/bohr^3 to 0.2 e/bohr^3 with an increment of 0.002 e/bohr^3. 107
7.3 Calculated band structure and DOS (density of states) for the 81-atom supercell modeling the H_s^- center in CaF_2. 108
7.4 Calculated band structure for the 81-atom supercell modeling the H_s^- center in BaF_2. 109
7.5 A view of the H_i^0-center nearest-neighbor geometry with the indication of relaxation shifts. 111
7.6 Electron charge (upper) and spin (lower) density map of a CaF_2 crystal with the periodic H_i^0 center from the (1 1 0) side view. Isodensity curves are drawn from 0 e/bohr^3 to 0.2 e/bohr^3 with an increment of 0.002 e/bohr^3 (charge) and drawn from -0.05 e/bohr^3 to 0.3 e/bohr^3 with an increment of 0.001 e/bohr^3 (spin). Blue and red lines in the spin density map denote positive and zero values, respectively. 112
7.7 Calculated band structure for the 82-atom supercell modeling the H_i^0 center in CaF_2. α (left) and β (right) denote the up- and down-spin states, respectively. 114

7.8 Calculated band structure for the 82-atom supercell modeling the H_i^0 center in BaF_2. α (left) and β (right) denote the up- and down-spin states, respectively. 115
7.9 Total and projected density of states (DOS) for the H_i^0 center in CaF_2 bulk. α and β denote the up- and down-spin states, respectively. 116
7.10 A top view of the surface H_s^--center nearest-neighbor geometry with the indication of the atomic displacement directions. F1 indicates the fluorine atoms located at the upper sublayer, and F2 means the fluorine atoms located at the lower sublayer. 117
7.11 Calculated band structure for the 108-atom supercell modeling the H_s^- center in the CaF_2 (upper) and BaF_2 (lower) (111) slabs. . . 120

8.1 H center oriented along the (111) axis. The arrows show the directions of the atomic displacements surrounding the H center. According to the symmetries of the atoms, different labels are defined in circles. 125
8.2 Charge density map of a CaF_2 crystal with the periodic H center from the (1 1 0) side view. Isodensity curves are drawn from 0 e/bohr^3 to 0.1 e/bohr^3 with an increment of 0.001 e/bohr^3. 128
8.3 Spin density maps of a CaF_2 crystal with the periodic H center from the (1 1 0) (upper) and (1 -1 0) (lower) side views. Isodensity curves are drawn from -0.01 e/bohr^3 to 0.1 e/bohr^3 with an increment of 0.001 e/bohr^3. Blue, green and red lines denote positive, negative and zero values, respectively. 129
8.4 Calculated band structure for the 81-atom supercell modeling the H center in CaF_2. α (left) and β (right) denote the spin-up and spin-down states, respectively. 130
8.5 Total and projected density of states (DOS) for the H center in the CaF_2 bulk. 131

A.1 The conceptual difference between the RHF and the UHF models. 143

LIST OF FIGURES

List of Tables

2.1 Theoretically calculated and experimentally observed lattice constant a_0 (Å) and bulk modulus B (GPa) for CaF_2 and BaF_2 crystals in their high-symmetry cubic phase. 17

4.1 Optimized lattice constant a_0 (Å), and bulk modulus B (GPa) for CaF_2 and BaF_2. 38

4.2 Static (Mulliken) charges (Q in e) of atoms and bond populations (P in me) for bulk CaF_2 and BaF_2 calculated by various methods. 39

4.3 The calculated optical gaps (in eV) for the CaF_2 bulk. Experimentally, the direct band gap is 12.1 eV and the indirect band gap is equal to 11.8 eV [Rubloff (1972)]. 42

4.4 The calculated optical gaps (in eV) for the BaF_2 bulk. Experimentally, the direct band gap is 11.0 eV [Rubloff (1972)]. 43

4.5 Atomic relaxations of slabs (containing 9 layers for CaF_2 and 15 layers for BaF_2) in the (111) direction (in percent of the lattice constant: $a_0 = 5.50$ Å for CaF_2; $a_0 = 6.26$ Å for BaF_2), calculated by means of the hybrid B3PW method. Positive sign corresponds to outward atomic displacement (toward the vacuum). 48

4.6 Atomic relaxations of the CaF_2 slab containing 15 layers in the (110) direction (in percent of the lattice constant: $a_0 = 5.50$ Å), calculated by means of the hybrid B3PW method. ΔY is the relative displacement (in percent of a_0) between two F atoms. Negative sign means the shortening of the F-F distance. 50

4.7 Atomic relaxations of the CaF_2 slab containing 15 layers in the (100) direction (in percent of the lattice constant: $a_0 = 5.50$ Å), calculated by means of the hybrid B3PW method. Positive sign corresponds to outward atomic displacement (toward the vacuum). 52

4.8 The calculated direct ($\Gamma \rightarrow \Gamma$) optical band gaps (eV) for the (100), (110) and (111) slabs. All calculations have been performed using the hybrid B3PW method. The last column contains the respective optical band gaps for the bulks. 55

4.9 Surface energies (J/m^2) for the CaF_2 and BaF_2 (111), (110) and (100) surfaces calculated by means of the hybrid B3PW method. The experimental surface energy for the CaF_2 (111) surface is 0.45 J/m^2 [Gilman (1960)]. 59

5.1 Formation energies, $E_{\text{formation}}$ (in eV), for an F center in CaF_2 and BaF_2 bulks for different supercells. 62

5.2 The effective charges (Q(e)) of the F center and surrounding atoms in CaF_2 and BaF_2 crystals for a supercell containing 48 atoms. ΔQ(e) is the charge difference between the defective and perfect crystals. 65

5.3 Atomic relaxations of 10 atoms surrounding an F center placed at the coordinate origin in the CaF_2 and BaF_2 48-atom supercells (in percent of the lattice constants, a_0=5.50 Å for CaF_2 , a_0=6.26 Å for BaF_2). Positive signs indicate the outward movements of the F center. 67

5.4 Direct optical gaps (eV) ($\Gamma \rightarrow \Gamma$) of the F center in CaF_2 and BaF_2 bulks. 70

5.5 Observed and calculated hyperfine constants a and b (MHz) for the F center in CaF_2. 73

5.6 Observed and calculated hyperfine constants a and b (MHz) for the F center in BaF_2. 74

5.7 Atomic relaxations of CaF_2 and BaF_2 slabs containing an F center located at the (111) surface (as a percentage of the lattice constant). Positive signs correspond to outward atomic displacements (toward the vacuum). The directions of atomic displacements in the XY-plane are indicated in Figure 5.10. Atom labels are also defined in Figure 5.10. L indicates the distance between two neighbor atoms. Positive signs correspond to repulsions. 82

5.8 The effective charges (Q(e)) of the surface F center and surrounding atoms for the supercell containing 4 layers (108 atoms). ΔQ(e) is the charge difference between the defective slab and the perfect CaF_2/BaF_2 bulk. (For the CaF_2 bulk, Ca: +1.803 e, F: -0.902 e. For the BaF_2 bulk, Ba: +1.845 e, F: -0.923 e.) 83

6.1 Direct optical gaps ($\Gamma \rightarrow \Gamma$) of the OV center in the CaF_2 bulk. V indicates the vacancy band; O_1, O_2 and O_3 are three oxygen bands. 95

6.2 Energies of three different $(OV)_2$-dimer mutual orientations with respect to configuration 0 (see Figure 6.6). 97

6.3 Direct optical gaps (eV) ($\Gamma \rightarrow \Gamma$) of the OV center at the CaF_2 (111) surface. V indicates the vacancy band; O_1, O_2 and O_3 are three oxygen bands. 99

7.1 Atomic relaxations of 10 atoms surrounding a H_s^- center in CaF_2 and BaF_2 81-atom supercells, (in percent of the lattice constants, a_0=5.50 Å for CaF_2 , a_0=6.26 Å for BaF_2). Positive signs indicate the outward movements of the H_s^- center. 106

7.2 The effective charges (Q(e)) of the H_s^- center and surrounding atoms in the CaF_2 and BaF_2 bulk. ΔQ(e) is the charge difference between the defective and perfect CaF_2/BaF_2 crystal. (For the CaF_2 bulk, Ca: +1.803 e, F: -0.902 e. For the BaF_2 bulk, Ba: +1.845 e, F: -0.923 e.) 106

7.3 Direct optical gaps (eV) ($\Gamma \rightarrow \Gamma$) of the H_s^- center in CaF_2 and BaF_2 bulks. 108

7.4 The effective charges (Q(e)) of the H_i^0 center and surrounding atoms in the CaF_2 and BaF_2 bulk. ΔQ(e) is the charge difference between the defective and perfect CaF_2/BaF_2 crystal. Spin (e) is expressed as (n_α - n_β). 110
7.5 Atomic relaxations of the atoms surrounding a H_i^0 center in CaF_2 and BaF_2. Positive signs indicate the outward movements of the H_i^0 center. 113
7.6 Direct optical gaps (eV) ($\Gamma \rightarrow \Gamma$) of the H_i^0 center in CaF_2 and BaF_2 bulks. 113
7.7 Observed and calculated isotropic hyperfine constants a and anisotropic hyperfine constants b (MHz) for the H_i^0 center in CaF_2 and BaF_2. 118
7.8 Atomic relaxation of the CaF_2 or BaF_2 slab containing an H_s^- center located at the (111) surface (as a percentage of the lattice constant). Positive signs correspond to outward atomic displacements (toward the vacuum). The directions of atomic displacements in the XY-plane are indicated in Figure 7.8. 118
7.9 The effective charges (Q(e)) of the surface H_s^- center and surrounding atoms. ΔQ(e) is the charge difference between the defective slab and perfect CaF_2/BaF_2 bulk. 119
7.10 Direct optical gaps (eV) ($\Gamma \rightarrow \Gamma$) of the (111) surface H_s^- center in CaF_2 and BaF_2. 119

8.1 Atomic relaxation of an H center oriented along the (111) axis in the CaF_2 or BaF_2 81-atom supercell (in percent of the lattice constants, a_0=5.50 Å for CaF_2, a_0=6.26 Å for BaF_2). The shell labels have been defined in Figure 8.1. 126
8.2 The effective charges (Q(e)) of the H center and surrounding atoms in CaF_2 and BaF_2 bulks. ΔQ(e) is the charge difference between the defective and perfect CaF_2/BaF_2 crystal. (For the CaF_2 bulk, Ca: +1.803 e, F: -0.902 e. For the BaF_2 bulk, Ba: +1.845 e, F: -0.923 e.) 127
8.3 Direct optical band gaps (eV) ($\Gamma \rightarrow \Gamma$) for H centers in CaF_2 and BaF_2 bulks. 130

List of Acronyms

- **BS** – Basis Set
- **BZ** – Brillouin Zone
- **CB** – Conduction Band
- **CI** – Configuration Interaction
- **DFT** – Density Functional Theory
- **DOS** – Density of States
- **ECP** – Effective Core Pseudopotential
- **ENDOR** – Electron Nuclear Double Resonance
- **EPR** – Electron Paramagnetic Resonance
- **FPLAPW** – Full-Potential Linearized Augmented Plane-Wave
- **GGA** – Generalized Gradient Approximation
- **GTF** – Gaussian Type Function
- **HF** – Hartree-Fock
- **LCAO** – Linear Combination of Atomic Orbitals
- **LDA** – Local Density Approximation
- **LEED** – Low Energy Electron Diffraction

- **LSDA** – Local Spin Density Approximation
- **LSDFT** – Local Spin Density Functional Theory
- **OLCAO** – Orthogonalized Linear Combination of Atomic Orbitals
- **QM** – Quantum Mechanical
- **RHF** – Restricted Hartree-Fock
- **SCF** – Self-Consistent-Field
- **UHF** – Unrestricted Hartree-Fock
- **UV** – Ultraviolet
- **VB** – Valence Band

Chapter 1

Introduction

Density Functional Theory (DFT) is widely used as an efficient and reliable method for computing the ground state energetics for a wide spectrum of solids. In recent years the use of functionals based on the generalized gradient approximation (GGA) has significantly improved the accuracy of computed energies when compared to the original local density approximation (LDA). However, the eigenvalues in DFT calculations do not formally correspond to excitation energies. This is particulary apparent in their use to to estimate band gaps where the non-analytic dependence of the effective potential on the density often leads to a crystalline gap which is less than half of that observed. The poor estimation of the band gap has a number of unfortunate consequences. For instance, in some systems the band gap collapses completely, and a qualitatively incorrect description of the ground state, as a metal rather than an insulator, is obtained. Consequently the utility and reliability of DFT calculations is limited, especially when properties depending explicitly on the excited state energies are of interest.

An alternative to DFT, Hartree-Fock (HF) approach gives both ground and excited states, but considerably overestimates the optical band gap. In order to study the electronic and optical properties of complex materials, an approach providing a reliable estimate of band gaps coupled with the reasonable description of the ground state is required. In the present study, the fulfillment of such requirements is clearly demonstrated using a simple *hybrid* HF/DFT scheme containing and admixture of non-local Fock exchange.

1. INTRODUCTION

In present theoretical investigations, I preformed *ab initio* calculations on CaF_2 and BaF_2 crystals in their high symmetry cubic phase ($Fm3m$). These alkaline-earth fluoride crystals present a great technological and fundamental interest due to their optical applications. Although these materials have been intensively investigated theoretically and experimentally at least in the last fifty years, a proper description of their electronic properties is still an area of active research. In order to make a contribution to the explanation of various electro-optical effects observed in alkaline-earth fluoride materials, their ground-state properties have been calculated from first principles and analyzed in the present study.

The present work is divided into three main parts. The first part, which includes Chapter 2 and 3, is concerned with the introduction into materials and different computational approaches. In Chapter 2, the selected alkaline-earth fluorides are described in detail, and the experimental and theoretical results known in the literature are presented. Chapter 3 serves to explain the DFT/HF formalism and methodology concisely. In the second part, including Chapter 4, a comparison of the effect of various approximations on the bulk properties of CaF_2 and BaF_2 calculated on equal computational grounds is presented; and as a basis for future defect calculations in the surface region of CaF_2 and BaF_2, theoretical investigations for pure (111), (110) and (100) surfaces are also reported. Finally, the third part which is the core of this thesis, including Chapter 5−8, concerns the defective alkaline-earth fluorides. Chapter 5 is dedicated to the investigations on F centers in bulks and the (111) surfaces. In Chapter 6, oxygen-vacancy (OV) dipoles in CaF_2 are concerned. Chapter 7 introduces my calculations on the other important anion impurities into CaF_2 and BaF_2, namely hydrogen centers. The last study, Chapter 8, is dealing with the hole trapped at an interstitial anion site, i.e. H center.

Chapter 2

Basic alkaline-earth fluorides: CaF_2 and BaF_2

Introduction

Alkaline-earth fluorides such as CaF_2 and BaF_2, whose band gaps are larger than 10 eV, are very important for many optical applications. As an example, a recent demand for lens materials available in short wavelength lithography is a typical application. The currently targeted wavelength is 157 nm (about 8 eV) from an F_2-excimer laser. This wavelength is far shorter than the transparent region of quartz that is the most popular optical material in the ultraviolet (UV) region. Additionally, for BaF_2, it is the fastest luminescent material that has been found to date [Kawano *et al.* (1999)]. Recently, BaF_2 has also been found to exhibit superionic conductivity by dissolving appropriate impurities into the lattice or by introducing an interface that causes the redistribution of ions in the space charge region, and is therefore considered as a candidate material for high-temperature batteries, fuel cells, chemical filters and sensors [Sata *et al.* (2000)]. Considering the high technological importance of alkaline-earth fluorides, it is not surprising, that during the last years, they have been the subject of many experimental and theoretical studies [Barth *et al.* (1990); Bennewitz *et al.* (1999); Catti *et al.* (1991); Ching *et al.* (1995); de Leeuw & Cooper (2003); de Leeuw *et al.* (2000); Foster *et al.* (2002); Gan *et al.* (1992); Jockisch *et al.* (1993); Letz & Parthier

(2006); Merawa *et al.* (2003); Puchin *et al.* (2001); Puchina *et al.* (1998); Rubloff (1972); Schmalzl *et al.* (2003); Verstraete & Gonze (2003); Wu *et al.* (2006)].

2.1 Bulk crystals

Pressure-induced phase transformations of CaF_2 have been reported by many research groups [Burnett *et al.* (2001); El'kin *et al.* (2005); Gerward *et al.* (1992); Kanchana *et al.* (2003b); Khenata *et al.* (2005); Seifert (1966); Speziale & Duffy (2002)]. In the first report of CaF_2 as a function of pressure in 1966, Seifert showed that it undergoes a pressure-induced phase transition from the fluorite structure ($Fm3m$) to an orthorhombic α-$PbCl_2$ structure ($Pnma$) in the pressure range 8−10 GPa [Seifert (1966)], which has been confirmed by other groups using various methods, such as X-ray diffraction, Raman spectra and theoretical calculations [El'kin *et al.* (2005); Gerward *et al.* (1992); Kanchana *et al.* (2003b); Khenata *et al.* (2005); Pendas *et al.* (1994); Speziale & Duffy (2002)]. Recently the initial stages of phase transformations in CaF_2 have been investigated in detail by means of the strain gauge technique in ideal hydrostatic pressure at room temperature, which indicates that the phase transition pressure is 8.01±0.01 GPa [El'kin *et al.* (2005)]. The high-pressure phase ($Pnma$) has been shown to still be stable up to 49 GPa at room temperature by X-ray diffraction and Raman spectra [Gerward *et al.* (1992); Speziale & Duffy (2002)]. The phase transition occurs at room temperature but is reversible under these conditions, with the $Pnma$ phase reverting to the $Fm3m$ during decompression. The phase change of BaF_2 from the cubic fluorite structure (β-BaF_2) to the orthorhombic α-$PbCl_2$ phase under pressure was also found by [Ayala (2001); Leger *et al.* (1995)]. This fluorite phase transition occurs at about 3 GPa [Leger *et al.* (1995)].

However, CaF_2 and BaF_2 are stable, chemically rather inert materials in moderate pressure and (or) temperature. Therefore, I only concentrate on the well-known face-centered-cubic (f.c.c) structure of alkaline-earth fluorides in this thesis.

The fluorite lattice structure is shown in Figure 2.1. In a compound MF_2 (M: metal ion), each M ion is surrounded by eight equivalent nearest-neighbor F ions forming the corners of a cube of which M is the center. Each F ion is

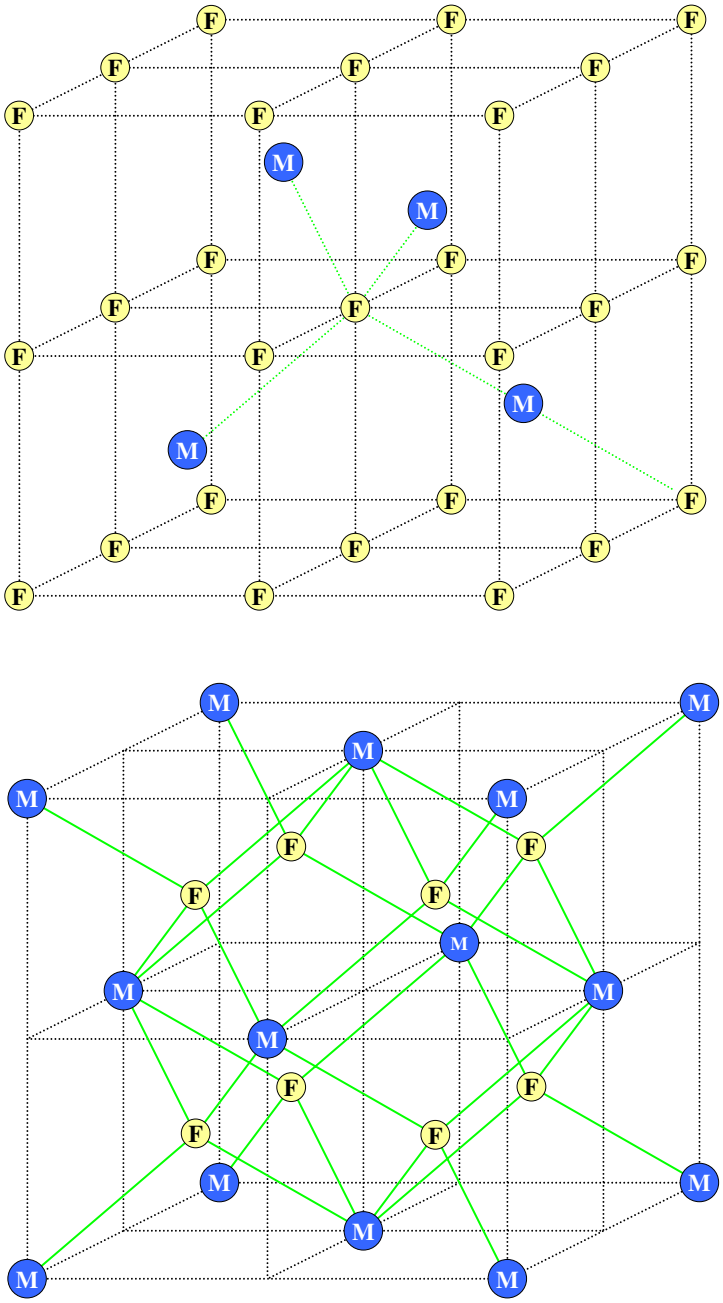

Figure 2.1: A cubic structure of an alkaline-earth fluoride with the formula unit MF_2, where M=Ca or Ba, and F is fluorine. The upper and lower figures correspond to T_d and O_h symmetries, respectively.

surrounded by a tetrahedron of four equivalent M ions. More fundamentally the structure has a f.c.c translational group and a space lattice of symmetry O_h^5. The unit cell of fluorite MF_2 includes three ions, one cation chosen as origin, and two anions that are situated at ($\frac{1}{4}a$, $\frac{1}{4}a$, $\frac{1}{4}a$) and (-$\frac{1}{4}a$, -$\frac{1}{4}a$, -$\frac{1}{4}a$), where a is the lattice constant. The site of the M ion has O_h symmetry and the site of the F ion has T_d symmetry. The interstitial site again has O_h symmetry, being at the center of a cube of eight F ions.

The bulk properties of crystals play an important role in solid state physics and are the basic measure allowing to understand how well experiments and theory correlate. These bulk properties could be mainly characterized by the lattice constant a_0 and the bulk modulus B, the theoretical and experimental values of which are collected in Table 2.1.

On the other hand, a substantial understanding of many crystalline properties requires the knowledge of the electronic structure and optical properties of the bulk material. In principle, the density of electrons at all points in the unit cell may be determined by a study of the diffraction of X-rays by the crystal. Such studies have been made on CaF_2 by Togawa (1964), by Weiss *et al.* (1957) and by Warren (1961). The crystal is built of well-defined ions with a low density of electrons between them. No evidence can be seen of a strong covalent bonding which would produce bridges of high electron density between the atoms.

A schematic band structure for CaF_2 showing the highest valence band (VB) and the lowest conduction band (CB) states is shown in Figure 2.2 [Rubloff (1972)]. Double-group notation is used for those levels where spin-orbit splitting is significant. Inclusion of the spin-orbit splitting of the F^- ions would split the upper level into two with symmetries Γ_8^- and Γ_6^-. This splitting is too small to be observed (0.03 eV), so that Γ_8^- and Γ_6^- are combined into a single level Γ_{15}. The presence of two fluorine ions in the unit cell produces the state with symmetry Γ'_{25}. Optical dipole transitions from Γ'_{25} to the conduction states with symmetries Γ_1, Γ_{12} and Γ'_{25} are forbidden by parity conservation [Starostin (1969)]. Transitions are however allowed from Γ_{15} to Γ_1. From Figure 2.2, it is clear that the excitons of lowest energy will probably be associated with the transitions of an electron from the Γ_{15} VB to the Γ_1 CB minimum of CaF_2. In the Frenkel picture this

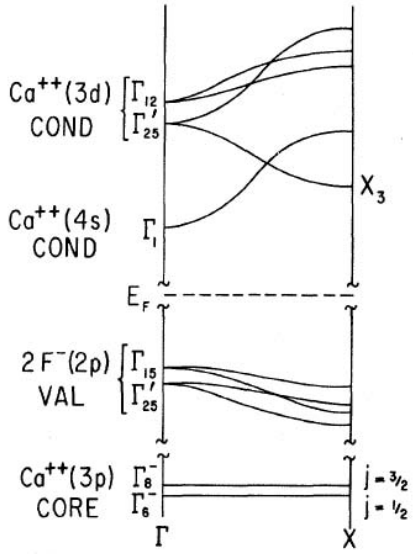

Figure 2.2: Schematic band structure of a typical alkaline-earth fluoride. Using CaF_2 as an example [Rubloff (1972)].

may be visualized as the transfer of an electron from a fluorine ion to a nearest-neighbor Ca^{2+} ion. Excitons of higher energy will be associated with the transfer of electrons from deeper core levels to the CB. The first of such transitions will generate holes in the $3p$ band of the Ca^{2+} ions. As the CB is primarily of Ca $4s$ character, these first core excitons may be regarded as an internal transition of the Ca^{2+} ion. A series of levels is indeed found to be associated with the $3p^5 3d$ and $3p^5 4s$ configuration of the free Ca^{2+} ion [Hayes (1974)].

Experimentally, the direct band gap of CaF_2 is 12.1 eV and the indirect gap is estimated to be 11.8 eV [Rubloff (1972)]. The band structure of CaF_2 also has been calculated from first-principles and published by several research groups recently. In the beginning of the 1990's, Catti *et al.* (1991) performed an all-electron *ab initio* Hartree-Fock calculation for the band structure of CaF_2. The energy-gap width between valence and conduction bands at the Γ point was about 21 eV, considerably exceeding the experimental value. From another side, it is well known that the local-density and generalized-gradient approximations (LDA and GGA) to density functional theory (DFT) systematically underesti-

mate the band gap in semiconductors and insulators; an error of a factor 2 is typical. For example, in Ref. [Verstraete & Gonze (2003)] the indirect band gap ($X \rightarrow \Gamma$) of 7.07 eV is underestimated with respect to experiment as expected in a GGA-DFT calculation. A similar result for the indirect band gap in CaF_2 (6.53 eV) using the first-principles orthogonalized linear combination of atomic orbitals (OLCAO) method in the LDA was obtained by Gan *et al.* (1992). For BaF_2, the direct band gap at the Γ point according to *ab initio* calculations performed by means of the full-potential linearized augmented plane-wave (FPLAPW) method, as implemented in the WIEN-97 code [Khenata *et al.* (2005)], is 7.49 eV, considerably less than the experimental value of 11.00 eV [Rubloff (1972)]. Jiang *et al.* (2003) predict BaF_2 to be a direct-gap material with the band gap of 7.5 eV using gradient-corrected functionals, Becke (1988a) for exchange and Perdew & Wang (1992) for correlation.

2.2 Defects in alkaline-earth fluorides

Many alkali halides provide an attractive medium for color center research because of the ease with which they can be grown in reasonably pure single-crystal form and because they may be colored by ionizing radiations. It is well known that optical and mechanical properties of crystals are strongly affected by defects and impurities unavoidably present in any real material. Contemporary knowledge of defects in solids has helped to create a field of technology, namely, *defect engineering*, which is aimed at manipulating the nature and concentration of defects in a material so as to tune its properties in a desired manner or to generate different behaviors. CaF_2 and BaF_2 could become important optical materials if one could avoid or, at least, control the photoinduced defect formation, which so far in applications degrades its optical quality. Therefore, it is important to understand the nature of defects in alkaline-earth fluorides.

Two intrinsic color centers have been observed in CaF_2 and BaF_2 by electron spin-resonance techniques. One is the F center, an electron trapped in an anion vacancy. The electron paramagnetic resonance (EPR) spectrum of F centers was identified in CaF_2 and BaF_2 by Arends (1964) who carried out his investigations on additively-colored crystals. The EPR spectrum of F centers

in additively-colored SrF_2 was subsequently described by den Hartog & Arends (1967). A description of the electron nuclear double resonance (ENDOR) spectrum of the F centers in CaF_2 was given by Hayes & Stott (1967) and in BaF_2 by Stoneham *et al.* (1968). Approximate values for the peak position of the F band in CaF_2, SrF_2 and BaF_2 were obtained by Arends (1964) and den Hartog & Arends (1967) by investigating effects of optical bleaching on the intensity of F center EPR spectra. More precise values for the peak position of the F band and values for the spin-orbit coupling constant in the excited ^2P state of the F band were obtained, using magneto-optical methods, by Cavenett *et al.* (1969). Further, optical absorption of the F centers in CaF_2 (3.3 eV) is well established experimentally [Hayes & Stoneham (1985)]. Nepomnyashchikh *et al.* (2002) measured that X-ray irradiation at 77 K of undoped BaF_2 produces F centers having absorption band at 2.3 eV. F centers in alkaline-earth fluorides also have been studied theoretically with the Xα method [Feltham (1967) and Taurian & Kai (1987)]. Puchina *et al.* (1998), using the Hartree-Fock embedded molecular cluster method, preformed calculations for the ground electronic state of the F center in CaF_2 crystal and its optical absorption energy.

The other is the V_k, or self-trapped hole. In some ionic crystals, holes may be stabilized at particular lattice sites due to strong electron-lattice interaction. These holes are described as self-trapped when no other lattice defects are involved [Hayes (1974)]. The self-trapped hole is paramagnetic and its EPR spectrum in CaF_2 was described by Hayes & Twidell (1962). The centers may be produced by X-irradiating undoped CaF_2 crystals at 77 K. Analysis of the EPR spectrum showed that the V_k center in alkaline-earth fluorides was a molecular-type center with its principal axis aligned along (100). The EPR of the V_k center in SrF_2 and BaF_2 was investigated by Tzalmona & Pershan (1969) and by Beaumont *et al.* (1970) and in BaF_2 by Kazumata (1969).

Another kind of important point defect, H center (a hole trapped at an interstitial anion site), which is relevant and similar to the V_k center, is readily formed in crystals doped with the heavier trivalent rare-earth ions (Re^{3+}). H centers produced by X-irradiation of rare-earth doped crystals have been identified in CaF_2 by Hall *et al.* (1969) and in CaF_2, SrF_2 and BaF_2 by Beaumont *et al.* (1970). In

suitably grown crystals these ions introduce charge-compensating fluorine interstitials (F_i^-) and a fraction of these are not closely associated with the rare-earth ions. When such crystals are X-irradiated at 77 K large concentrations of V_k centers are produced and a relatively small concentration of H centers. However, when the crystals are heated to induce migration of V_k centers a fraction of the moving holes are retrapped at F_i^- sites producing additional H centers. The hole is located on the interstitial fluorine and a nearest substitutional fluorine giving a (111) oriented molecular ion (X_2^-). H centers may also be produced in undoped alkaline-earth fluorides by heavy irradiation with 1 MeV electrons at 77 K. In some orientations of the external magnetic field the EPR lines of H centers produced by electron irradiation show partly resolved structure suggesting perturbation by another defect produced by the radiation [Hayes *et al.* (1974)]. For the optical absorption, Beaumont *et al.* (1970) found evidence for the existence of a absorption band of the H center peaking at about 4.03 eV in CaF_2 and at about 3.76 eV in BaF_2.

On the other hand, coloration effects in alkaline-earth fluorides are strongly influenced by some impurities. Evidence for the existence of hydroxyl and carbonate ions in CaF_2 have been obtained by infrared methods [Bontinck (1958b); Wickersheim & Hanking (1959)]. Some trivalent rare-earth ions strongly affect the colorability of crystals because of their electron-trapping properties and because of the charge-compensating defects introduced into the crystals by them. Hydrogen and oxygen are two kinds of important point impurities which affect the behavior of alkaline-earth fluorides under ionizing radiations because they act as hole traps and under certain circumstances introduce anion vacancies into the crystals.

Hydrogen-doped crystals color quickly under X-irradiation at room temperature because of rapid generation of F-aggregate centers. Using infrared methods it was shown by Elliott *et al.* (1965) that crystals treated in this way contain hydrogen dissolved as H^- ions in fluorine sites (H_s^- centers) and concentrations of H_s^- approaching 10^{20} cm^{-3} are readily achieved. The first detailed investigations of CaF_2:H crystals were carried out by Hall & Schumacher (1962) who showed, using EPR methods, that X-irradiation at room temperature produced hydrogen atoms stable in interstitial sites (H_i^0 centers). It was subsequently shown by

Bessent *et al.* (1967, 1969), using again EPR methods, that X-irradiation at 77 K produced hydrogen atoms in fluorine sites (H_s^0 centers) and that the H_s^0 centers are converted to H_i^0 centers on warming to room temperature.

Investigations by Adler & Kveta (1957) and by Bontinck (1958b) show that CaF_2 reacts readily with water vapor at high temperatures and suggest that the resulting hydrolysis gives rise to a variety of defects which includes O^{2-} ions in fluorine sites and charge-compensating fluorine vacancies (see also [Messier (1968)]). It has been suggested that absorption at about 200 nm in hydrolysed CaF_2 is associated with the presence of oxygen [Bontinck (1958a); Bruch *et al.* (1964); Feltham & Andrews (1965)]. Charge compensation of Y^{3+} and trivalent rare-earth ions in CaF_2 by O^{2-} ions is fairly well established. A first step in the understanding of the effects of ionizing radiation on CaF_2 containing oxygen was made by Bill & Lacroix (1966) who investigated hydrolysed CaF_2 by EPR methods. They found a spectrum after X-irradiation at room temperature which they assigned to O^- ions in fluorine sites. This is produced by capture of a hole by substitutional O^{2-} ions. Recently, oxygen-vacancy dipoles and dimers in CaF_2 crystals have been studied *ab initio* at DFT level and with the shell model using pair potentials by Mysovsky *et al.* (2004). Optical absorption of O^{2-}-V_A dipole have been calculated with time-dependent (TD) DFT and identified with experimental absorption bands, which appeared to have complex structure. Their calculations show that the optical transitions are split into three groups. The first one contains 5.22, 5.38 and 5.61 eV transitions from $2p$-orbitals of oxygen to the ground state of vacancy. Experimentally, the results of polarization of luminescence measurements [Archangelskaya *et al.* (1980); Radzhabov & Figura (1986)] show the 6.7 eV absorption band which consists of at least two elementary peaks with separation of 0.48 eV.

2.3 Surfaces

Laser ablation and the resistivity of optical materials against laser pulses with sub-band-gap photon energy strongly depend on the purity of the crystal and the quality of its surface. Surface defects and adsorbed species induce local electronic states in the insulator band gap, initiating optical absorption. The

absorbed energy is transferred to the lattice and may cause damage and ablation, especially when dealing with high-power laser light [Reichling (1998); Reichling *et al.* (1999)]. Information about the atomic and electronic structure of particular surface defects can be very helpful for achieving a detailed understanding the basic mechanisms of such laser degradation processes. As a promising candidate for use in high-performance optical lens systems [Hofmann (1992)] for the next generation of ultraviolet laser steppers operated a wavelength of 193 nm, CaF_2 lens systems involve a large number of surfaces and, therefore, it is an important task to understand the structural and optical properties of such surfaces.

An alkaline-earth fluorite crystal is composed of F-M-F triple layers in the (111) direction. These are the natural cleavage planes of the crystal [Hayes (1974)]. The structure of this (111) plane is shown schematically in Figure 2.3. The perfect (111) cleavage plane is F^- terminated and the topmost F^- ions form a hexagonal array. The threefold symmetry of the surface is determined by the M^{2+} and F^- ions in the second and third planes, as seen in the top view (top figure) of Figure 2.3.

A comparative study of CaF_2 (111) surfaces cleaved in air and in ultrahigh vacuum probing the density of occupied electronic states in the band gap by ultraviolet photoelectron spectroscopy reveals that there is a tail of emission extending from the valence band about 6 eV into the band gap for air-cleaved crystals, while there is no measurable band-gap emission for vacuum-cleaved crystals [Huisinga *et al.* (1998)]. This result indicates that cleavage steps do not introduce band-gap states and the density of states in the band gap for air-cleaved crystals is mainly formed during irradiation by oxygen already present at the crystal surface.

Theoretically, Puchin *et al.* (2001) investigated the atomic and electronic structure and relaxation of the perfect (111) surface and several low-index surfaces of CaF_2 by means of an *ab initio* Hartree-Fock method. According to their study for the (111) slab, the surface energy was found to be 0.47 J/m^{-2} and in good agreement with experimental data (0.45 J/m^{-2}) [Gilman (1960)]; the charges of ions in the surface layers are almost the same as in the bulk or in deeper layers of the slab; the surface band gap are almost the same as that in the bulk; and only the topmost layer introduces a small contribution to the density of states just above the bulk valence band edge. The (110) and (100)

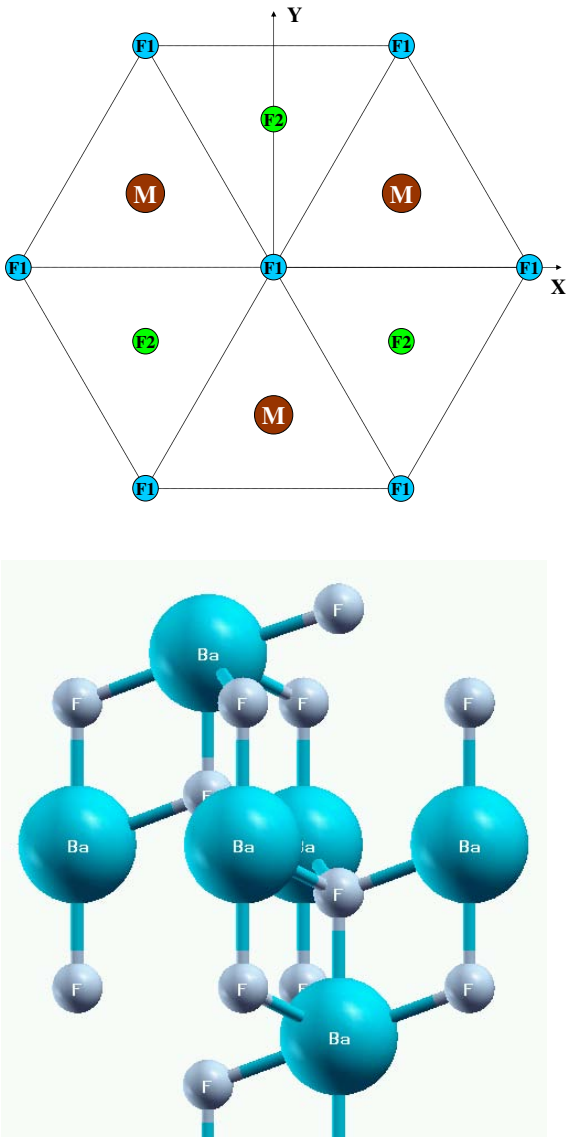

Figure 2.3: The structure of the $MF_2(111)$ surface in the top and side view. F1 and F2 indicate the fluorine atoms located at the upper and lower sublayers, respectively.

slabs have higher surface energies and the calculated values are 0.819 J/m^{-2} and 1.189 J/m^{-2} [Puchin *et al.* (2001)], respectively, which is in agreement with the fact that the (111) surface is the natural cleavage plane of the crystal.

The electronic structure of the perfect CaF_2 (111) surface has also previously been calculated using the semi-empirical LCAO method [Stankiewicz & Modrak (1995)]; however, surface relaxation effects were neglected. Earlier calculations of the surface structure and dynamics including relaxation were performed in the framework of the shell model [Jockisch *et al.* (1993); Tasker (1980)]. Both calculations predicted the reduction of the distance between the topmost fluorine and next calcium layers. However, the magnitude of this relaxation depends on the parameters of the pair potential model. It varies between 19% [Jockisch *et al.* (1993)] and 1.7% [Tasker (1980)] of the interlayer distance. Experimentally, the surface structures of CaF_2(111) and BaF_2(111) was investigated by means of low energy electron diffraction (LEED) with primary beam currents [Vogt *et al.* (2005)]. The results provide for the first time quantitative experimental information about the relaxation of this surface. The CaF_2 (111) surface deviates only insignificantly from a truncated fluorite bulk lattice with F-Ca-F layer structure, the largest displacement being the inward shift of the topmost layer of fluoride anions by 0.03±0.06 Å. The same contraction of the interlayer distance at the topmost union is displaced towards the bulk by 0.12±0.07 Å. The positions of the alkaline-earth metal cations as well as those of the second fluoride layer in this topmost F-M-F sheet are almost identical to their bulk values. The same holds for all deeper layers.

The electronic structure of CaF_2 (111) with a completely remove topmost fluorine layer, as an example of a defective surface, was calculated and for this configuration an additional half-filled band was found in the middle of the band gap [Stankievicz & Kisiel (1994)]. Band-gap states were also found in molecular cluster calculations of the electronic structure of the CaF_2 (111) with surface F centers and F-center clusters by Westin *et al.* (1990).

2.4 Motivation

As it is shown above, the electronic structure of alkaline-earth fluorides have been the subject of many experimental and theoretical investigations. The alkaline-earth fluorides have excellent transmission properties without absorption bands over a wide wavelength range and these optical properties are related to their structural and electronic properties, especially, such as a very large band gap. Therefore, obtaining the reliable prediction of the band gap in semiconductors and insulators is a well recognized problem in first-principles calculations, and still remains an obstacle in *ab initio* band-gap engineering. This is even more important for defects, since the defects level positions with respect to the band edges are of key importance for their applications.

In order to study the electronic and optical properties of alkaline-earth fluorides, an approach providing a reliable estimate of band gaps while retaining a reasonable ground state description of the GGA is required. In the present study the fact that these requirements are satisfied by a simple hybrid scheme which contains an admixture of non-local Fock exchange to the DFT scheme is clearly demonstrated.

Hybrid functional were originally developed to improve the description of the ground state energetics of small molecules [Becke (1993b)]. Subsequently, they have been demonstrated to be significantly more reliable then the best GGA functional for computing atomization enthalpies [Curtiss *et al.* (1997)], ionization potentials and electron affinites [Curtiss *et al.* (1998)], geometries and vibrational frequencies [Adamo *et al.* (2000)]. The application of these methods in periodic calculations of solids has been inhibited by difficulties in computing the non-local Fock exchange since this is not convenient within the commonly used plane-wave basis set. Nevertheless, it can be implemented readily and very efficiently within the linear combination of atomic orbitals (LCAO) technique that uses localized gaussian type functions (GTF) localized at atoms as the basis for expansion of the crystalline orbitals. Recently, a LCAO-GTF study has been performed for both bulk and surface phases of $SrTiO_3$ crystal [Heifets *et al.* (2002)]. In this study, the electronic structure of the $SrTiO_3(100)$ surface has been calculated by means of various approximations including *ab initio* HF method with electron

correlation corrections and DFT with different exchange-correlation functionals, including hybrid (B3PW, B3LYP) exchange techniques. This work demonstrated a noticeable improvement of the calculated lattice constant, bulk modulus and optical band gap of $SrTiO_3$ with respect to those experimentally observed when the hybrid B3LYP functional was applied.

For my PhD program, further *ab initio* investigations on alkaline-earth fluorides are of high interest to give the most reliable theoretical predictions for many crystal properties. Therefore the main aims of present study are the following:

- Critical choice among different Hamiltonians for the *ab initio* calculations of selected alkaline-earth fluorides.
- Using the selected method to obtain the electronic structure of the perfect and defective fluorite crystals.

Additionally, it could be noted that comparative first-principles calculations on alkaline-earth fluoride surfaces are quite scares in literature. Thus, this study is an attempt to compensate such lack of information.

Table 2.1: Theoretically calculated and experimentally observed lattice constant a_0 (Å) and bulk modulus B (GPa) for CaF_2 and BaF_2 crystals in their high-symmetry cubic phase.

	CaF_2		BaF_2	
	Theoretical	Experimental	Theoretical	Experimental
a_0	5.5252[a]	5.466[b]	6.233[l]	6.20[c]
(Å)	5.3252[a]	5.4630[d]	6.292[e]	6.20[f]
	5.563[g]		6.32[h]	
	5.444[b]		6.20[i]	
	5.3378[j]		6.08[k]	
	5.515[l]		6.196[m]	
B	77, 103[a]	81.0±1.2[n]	56.4[l]	57[c]
(GPa)	84.7, 82.7[b]	87±5[b]	57.3[e]	
	103[j]	82.0±0.7[o]	58.5[h]	
	82.14[l]	81.1[p]	79.64[k]	
		84.7[q]		

[a]reference Wu *et al.* (2006)
[b]reference Gerward *et al.* (1992)
[c]reference Leger *et al.* (1995)
[d]reference Wu *et al.* (2005)
[e]reference Jiang *et al.* (2003)
[f]reference Wyckoff (1982)
[g]reference Pendas *et al.* (1994)
[h]reference Merawa *et al.* (2003)
[i]reference Ching *et al.* (1995)
[j]reference Kanchana *et al.* (2003b)
[k]reference Kanchana *et al.* (2003a)
[l]reference Khenata *et al.* (2005)
[m]reference Levine *et al.* (2003)
[n]reference Katrusiak & Nelmes (1986)
[o]reference Speziale & Duffy (2002)
[p]reference Catlow *et al.* (1978)
[q]reference Ho & Ruoff (1967)

Chapter 3

HF/DFT formalism and methodology

Introduction

The theoretical possibility to study complex crystalline systems containing many atoms is to perform computer simulations. This can be performed with a variety of methods ranging from classical to quantum mechanical (QM) approaches. The former are force field or semi-empirical schemes, in which the forces that determine the interactions between the atoms are parameterized in order to reproduce a series of experimental data, such as equilibrium geometries, bulk modular or lattice vibrational frequencies (phonons). These schemes have reached a high level of sophistication and are often useful within a given class of materials provided good parameters are already known. If, however, such parameters are not available, or if a system shows unusual phenomena that are not yet understood, one must rely only on *ab initio* calculations. They are more demanding in terms of computer requirements and thus allow only the treatment of much smaller unit cells than semi-empirical calculations do. The advantage of first-principle methods lies in the fact that they do not require any experimental knowledge to carry out such calculations. The following presentation will be restricted to *ab initio* methods whose main characteristics will be briefly sketched.

The fact that electrons are indistinguishable and are Fermions requires that their wave functions must be antisymmetric when two electrons are permuted.

This leads to the phenomenon of exchange and correlation. There are two types of approaches for a full quantum mechanical treatment of many-atom systems: Hartree-Fock (HF) and Density Functional Theory (DFT). The traditional scheme is the HF method which is based on a wave function in a form of one Slater determinant. Exchange is treated exactly but correlation effects are neglected. The latter can be included by more sophisticated approaches such as configuration interaction (CI), but they progressively require much more computer time. As a consequence, it is only feasible to study small systems which contain a few atoms. An alternative scheme is DFT which is commonly used to calculate the electronic structure of complex systems containing many atoms such as large molecules or solids. It is based on the electron density rather than on the wave functions and treats both exchange and correlation, but both approximately. The ideal crystal is defined by the unit cell which may contain several atoms (up to about 100, in practical state-of-the-art calculations) and is repeated infinitely according to the translational symmetry. Periodic boundary conditions are used to describe an infinite crystal. The additional symmetry operations (inversion, rotation, mirror plane, etc.) that retain the ideal crystal invariant allow to simplify the calculations, which always correspond to the absolute zero temperature.

Detailed HF and DFT methods can be seen in most general physical chemistry textbooks. In this Chapter, I introduce the elementary concepts of HF and DFT methods concisely. The sketchy text mainly comes from Leach (2001).

3.1 HF formalism

3.1.1 Schrödinger equation

The starting point for any discussion of quantum mechanics is, of course, the Schrödinger equation. When the external potential $\mathscr{V}$ is independent of time then the Schrödinger equation can be written in the time-independent form:

$$\left\{-\frac{\hbar^2}{2m}\nabla^2 + \mathscr{V}\right\}\Psi(\mathbf{r}) = E\Psi(\mathbf{r}) \tag{3.1}$$

Where $\hbar$, m and E are Planck's constant, the mass of particles and the total energy of the system, respectively. The wave function of the system in coordinate space ($\mathbf{r}$) is expressed by $\Psi(\mathbf{r})$.

Solving the Schrödinger equation for atoms with more than one electron is complicated by a number of factors. The first complication is that the Schrödinger equation for such systems can not be solved exactly, even for the helium atom. The helium atom has three particles (two electrons and one nucleus) and is an example of a *three-body problem*. No exact solutions can be found for systems that involve three (or more) interacting particles. Thus, any solutions we might find for polyelectronic atoms or molecules can only be approximations to the real, true solutions of the Schrödinger equation. A second complication with multi-electron species is that we must account for electron spin. Electron spin is incorporated into the solutions to the Schrödinger equation by writing each one-electron wave function as the product of a spatial function that depends on the coordinates of the electron and spin function that depends on its spin. Such solutions are called *spin orbitals*, which we will represent using the symbol χ.

Next, what is an appropriate functional form of the wave function for a poly-electronic system with N electrons that satisfies the antisymmetry principle? A determinant is the most convenient way. In general, if we have N electrons in spin orbitals χ_1, χ_1, ..., χ_N (where each spin orbital is the product of a spatial function and a spin function) then an acceptable form of the wave function is:

$$\Psi = \frac{1}{\sqrt{N!}} \begin{vmatrix} \chi_1(1) & \chi_2(1) & \cdots & \chi_N(1) \\ \chi_1(2) & \chi_2(2) & \cdots & \chi_N(2) \\ \vdots & \vdots & \ddots & \vdots \\ \chi_1(N) & \chi_2(N) & \cdots & \chi_N(N) \end{vmatrix} \tag{3.2}$$

Where $\chi_1(1)$ is used to indicate a function that depends on the space and spin coordinates of the electron labeled $'1'$. The factor $1/\sqrt{N!}$ ensures that the wave function is normalized. This functional form of the wave function is called a *Slater determinant* and is the simplest form of an orbital wave function that satisfies the antisymmetry principle.

3.1.2 The energy of a general polyelectronic system

For a N-electron system, the Hamiltonian (in atomic units $m = \hbar = e^2 = 1$) takes the following general form:

$$\mathscr{H} = \left(-\frac{1}{2}\sum_{i=1}^{N} \nabla_i^2 - \frac{1}{r_{1A}} - \frac{1}{r_{1B}} \cdots + \frac{1}{r_{12}} + \frac{1}{r_{13}} + \cdots \right) \tag{3.3}$$

where r is the distance between two charged particles (electron or nucleus). The nuclei are labeled using capital letters A, B, C, etc., and the electrons are labeled 1, 2, 3, $\cdots$. As usual, the energy can be calculated from $E = \int \Psi \mathscr{H} \Psi$. There are three types of interaction that contribute to the total electronic energy of the system. First, there is the kinetic and potential energy of each electron moving in the field of the nuclei. The second contribution to the energy arises from the electrostatic repulsion between pairs of electrons. This interaction depends on the electron-electron distance. The third contribution to the energy is the exchange 'interaction'. This has no classical counterpart and arises because the motions of electrons with parallel spins are correlated: whereas there is a finite probability of finding two electrons with opposite (i.e. paired) spins at the same point in space, where the spins are the same then the probability is zero. This can be considered a manifestation of the Pauli principle.

3.1.3 The Hartree-Fock equations

It is well known that for many-body problems there is no 'correct' solution; we therefore require some means to decide whether one proposed wave function is 'better' than another. Fortunately, the *variation theorem* provides us with a mechanism for answering this question. The 'best' wave function is achieved when the energy is a minimum. The HF equations are obtained by using the variation theorem to the energy, subject to the constraint that the molecular orbitals remain orthonormal. This type of constrained minimization problem can be tackled using the method of Lagrange multipliers. After performing tediously mathematical calculations, we can get the HF equations taking on the standard eigenvalue form:

$$\mathscr{F}_i \chi_i = \varepsilon_i \chi_i \tag{3.4}$$

Where, the eigenvalue ε_i indicates the orbital energy of the spin orbital, χ_i, and $\mathscr{F}_i$ is called the *Fock operator*:

$$\mathscr{F}_i(1) = \mathscr{H}^{\text{core}}(1) + \sum_{j=1}^{N} \{\mathscr{J}_j(1) - \mathscr{K}_j(1)\} \tag{3.5}$$

As mentioned before, $\mathscr{H}^{\text{core}}(1)$ corresponds to the kinetic and potential operator of an electron moving in the field of the nuclei. The Coulomb operator, $\mathscr{J}_j(1)$ is written as:

$$\mathscr{J}_j(1) = \int d\tau_2 \chi_j(2) \frac{1}{r_{12}} \chi_j(2) \tag{3.6}$$

and the exchange operator, $\mathscr{K}_j(1)$ has the following expression:

$$\mathscr{K}_j(1)\chi_i(1) = \left[\int d\tau_2 \chi_j(2) \frac{1}{r_{12}} \chi_i(2)\right] \chi_j(1) \tag{3.7}$$

The general strategy of solving these equations is called a *self-consistent-field* (SCF) approach. First, a set of trial solutions χ_i to the HF eigenvalue equations are obtained. These are used to calculate the Coulomb and exchange operators. The HF equations are solved, finding a second set of solutions χ_i' which are used in the next iteration. The SCF method thus gradually refines the individual electronic solutions that correspond to lower and lower total energies until the point is reached at which the results for all the electrons are unchanged, when they are said to be *self-consistent*.

3.1.4 The electron correlation

Within the HF method, the total, antisymmetric, wave function is approximated by a single Slater determinant. At this point, it must be said that exact wave functions can not generally be expressed as single determinants. The primary deficiency of the HF procedure is inadequate description of the correlation between electrons. A priori, the single-determinant approximation takes no account of e.g. correlation between electrons with opposite spin, thus leading to a total electronic energy which does not equal the exact solution of the non-relativistic Schrödinger equation, within the Born-Oppenheimer approximation. The calculated HF limit is always above the exact energy. Using the Roothaan (1951) procedure, which

linearizes the HF problem, the so-called HF limit can be obtained, if an infinite number of basis functions is used. The correlation energy is defined as the difference between the energy in the HF limit and the exact non-relativistic energy of a system.

A certain amount of electron correlation is already considered within the HF theory, as can be seen in the electron exchange term (correlation between parallel spin electrons) of the expectation value. This prevents two parallel-spin electrons being found at the same point in space. This kind of correlation is often referred to as *Fermi correlation*. The major deficiency in the HF scheme is the neglect of the correlation between the spatial position of electrons with opposite spin due to their Coulomb repulsion. This is called *Coulomb correlation*.

Within HF theory, the interaction of one electron with the remaining $(N-1)$ electrons is approximated by the interaction of the electron with the average field generated by the $(N-1)$ electrons. This field is static and neglects the influence of the motion of the one electron on the motion of the other $(N-1)$ electrons and vice versa, that is, the motion of electrons is correlated. Considering two electrons, it can be said that the probability of finding one electron at a certain position in space, depends on the position of the other electron and vice versa. In the statistical sense, for independent electrons, the product of the density functions does not adequately describe the ′real′ situation. For small distances, the pair density is too large and similarly, too small for large distances. That is, the electrons ′avoid′ each other. If the electrons were not correlated, each electron could be described by a ′charge cloud′ (density) and the only interaction between the two electrons would be the Coulomb repulsion between these densities. However, the actual electron repulsion is less than it should be according to this model, because electrons avoid each other. That is, they never come as close together as statistically independent particles would do. This decreased repulsion, due to the correlation of the electron motion, is partly responsible for the correlation energy.

Summing up, for the correlation of the electrons in space, there are essentially two reasons. One is that an antisymmetric wave function (Pauli's principle) must be used for electrons (fermions) and the associated correlation is the Fermi

correlation. The other is the Coulomb correlation, corresponding to the Coulomb repulsion of the electrons.

3.2 Density functional theory

3.2.1 Hohenberg-Kohn theorems

Density functional theory (DFT) is an approach to the electronic structure of atoms and molecules which has enjoyed a dramatic surge of interest since the late 1980s and 1990s [Parr (1983); Wimmer (1997)]. Our approach here will be to introduce the key elements of the theory and to identify the similarities and differences between DFT and the HF approach. In HF theory the multi-electron wave function is expressed as a Slater determinant which is constructed from a set of N single-electron wave functions. DFT also considers single-electron functions. However, whereas HF theory does indeed calculate the full N-electron wave function, DFT only attempts to calculate the total electronic energy and the overall electronic density distribution. The central idea underpinning DFT is that there is a relationship between the total electronic energy and the overall electronic density. This is not a particularly new idea; indeed an approximate model developed in the late 1920s (the Thomas-Fermi model) contains some of the basic elements. However, the real break through came with a paper by Hohenberg & Kohn (1964), who showed that the ground-state energy and other properties of a system were uniquely defined by the electron density. This is sometimes expressed by stating that the energy, E, is a unique $functional$ of $\rho(\mathbf{r})$. In DFT the energy functional is written as a sum of two terms:

$$E[\rho(\mathbf{r})] = \int V_{\text{ext}}(\mathbf{r})\rho(\mathbf{r})d\mathbf{r} + F[\rho(\mathbf{r})] \tag{3.8}$$

The first term arises from the interaction of the electrons with an external potential $V_{\text{ext}}(\mathbf{r})$ (typically due to the Coulomb interaction with the nuclei). $F[\rho(\mathbf{r})]$ is the sum of the kinetic energy of the electrons and the contribution from interelectronic interactions. The minimum value in the energy corresponds to the exact ground-state electron density, so enabling a variational approach to be used (i.e. the 'best' solution corresponds to the minimum of energy and an incorrect

density gives an energy above the true energy). There is a constraint on the electron density as the number of electrons (N) is fixed:

$$N = \int \rho(\mathbf{r}) d\mathbf{r} \tag{3.9}$$

In order to minimize the energy we introduce this constraint as a Lagrangian multiplier ($-\mu$), leading to:

$$\frac{\delta}{\delta\rho(\mathbf{r})}\left[E[\rho(\mathbf{r})] - \mu\int \rho(\mathbf{r}) d\mathbf{r}\right] = 0 \tag{3.10}$$

From this we can write:

$$\left(\frac{\delta E[\rho(\mathbf{r})]}{\delta\rho(\mathbf{r})}\right)_{V_{\text{ext}}} = \mu \tag{3.11}$$

Equation (3.11) is the DFT equivalent of the Schrödinger equation. The subscript V_{ext} indicates that this is under conditions of constant external potential (i.e. fixed nuclear positions). It is interesting to note that the Lagrange multiplier, μ, can be identified with the chemical potential of an electron cloud for its nuclei.

The second landmark paper in the development of DFT was by Kohn & Sham (1965) who suggested a practical way to solve the Hohenberg-Kohn theorem for a set of interacting electrons. The difficulty with Equation (3.8) is that we do not know what the function $F[\rho(\mathbf{r})]$ is. Kohn and Sham suggested that $F[\rho(\mathbf{r})]$ should be approximated as the sum of three terms:

$$F[\rho(\mathbf{r})] = E_{\text{KE}}[\rho(\mathbf{r})] + E_{\text{H}}[\rho(\mathbf{r})] + E_{\text{XC}}[\rho(\mathbf{r})] \tag{3.12}$$

where $E_{\text{KE}}[\rho(\mathbf{r})]$ is the kinetic energy, $E_{\text{H}}[\rho(\mathbf{r})]$ is the electron-electron Coulombic energy, and $E_{\text{XC}}[\rho(\mathbf{r})]$ contains contributions from exchange and correlation. It is important to note that the first term in Equation (3.12), $E_{\text{KE}}[\rho(\mathbf{r})]$, is defined as the kinetic energy of a system of *non-interacting* electrons with the same density $\rho(\mathbf{r})$ as the real system:

$$E_{\text{KE}}[\rho(\mathbf{r})] = \sum_{i=1}^{N}\int \psi_i(\mathbf{r})\left(-\frac{\nabla^2}{2}\right)\psi_i(\mathbf{r}) d\mathbf{r} \tag{3.13}$$

The second term, $E_{\text{H}}[\rho]$, is also known as the Hartree electrostatic energy. The Hartree approach to solving the Schrödinger equation was introduced briefly before and almost immediately dismissed because it fails to recognize that electronic

motions are correlated. In the Hartree approach this electrostatic energy arises from the classical interaction between two charge densities, which, when summed over all possible pairwise interactions, gives:

$$E_{\mathrm{H}}[\rho(\mathbf{r})] = \frac{1}{2}\iint \frac{\rho(\mathbf{r}_1)\rho(\mathbf{r}_2)}{|r_1 - r_2|} d\mathbf{r}_1 d\mathbf{r}_2 \tag{3.14}$$

Combining these two and adding the electron-nuclear interaction leads to the full expression for the energy of an N-electron system within the Kohn-Sham scheme:

$$\begin{aligned} E[\rho(\mathbf{r})] &= \sum_{i=1}^{N} \int \psi_i(\mathbf{r}) \left(-\frac{\nabla^2}{2}\right) \psi_i(\mathbf{r}) d\mathbf{r} + \frac{1}{2}\iint \frac{\rho(\mathbf{r}_1)\rho(\mathbf{r}_2)}{|\mathbf{r}_1 - \mathbf{r}_2|} d\mathbf{r}_1 d\mathbf{r}_2 \\ &+ E_{\mathrm{XC}}[\rho(\mathbf{r})] - \sum_{A=1}^{M} \int \frac{Z_A}{|\mathbf{r} - \mathbf{R}_A|} \rho(\mathbf{r}) d\mathbf{r} \end{aligned} \tag{3.15}$$

This equation acts to *define* the exchange-correlation energy functional $E_{\mathrm{XC}}[\rho(\mathbf{r})]$, which thus contains not only contributions due to exchange and correlation but also a contribution due to the difference between $E_{\mathrm{KE}}^{(T)}[\rho]$, the true kinetic energy of the system, and $E_{\mathrm{KE}}[\rho]$. Therefore the exchange-correlation energy functional $E_{\mathrm{XC}}[\rho(\mathbf{r})]$ has the following expression:

$$E_{\mathrm{XC}}[\rho] = (E_{\mathrm{KE}}^{(T)}[\rho] - E_{\mathrm{KE}}[\rho]) + (E_{\mathrm{ee}}[\rho] - E_{\mathrm{H}}[\rho]) \tag{3.16}$$

Here, $E_{\mathrm{ee}}[\rho]$ is the true electron-electron interaction.

Kohn and Sham wrote the density $\rho(\mathbf{r})$ of the system as the sum of the square moduli of a set of one-electron orthonormal orbitals:

$$\rho(\mathbf{r}) = \sum_{i=1}^{N} |\psi_i(\mathbf{r})|^2 \tag{3.17}$$

By introducing this expression for the electron density and applying the appropriate variational condition the following one-electron Kohn-Sham equations result:

$$\left\{-\frac{\nabla_1^2}{2} - \left(\sum_{A=1}^{M} \frac{Z_A}{r_{1A}}\right) + \int \frac{\rho(\mathbf{r}_2)}{r_{12}} d\mathbf{r}_2 + V_{\mathrm{XC}}[\mathbf{r}_1]\right\} \psi_i(\mathbf{r}_1) = \varepsilon_i \psi_i(\mathbf{r}_1) \tag{3.18}$$

In Equation (3.18) we have written the external potential in the form appropriate to the interaction with M nuclei. ε_i are the orbital energies and V_{XC} is known

as the exchange-correlation functional, related to the exchange-correlation energy by:

$$V_{\mathrm{XC}}[\mathbf{r}] = \left(\frac{\delta E_{\mathrm{XC}}[\rho(\mathbf{r})]}{\delta \rho(\mathbf{r})} \right) \tag{3.19}$$

The total electronic energy is then calculated from Equation (3.15).

To solve the Kohn-Sham equations, a self-consistent approach is taken. An initial guess of the density is fed into Equation (3.18) from which a set of orbitals can be derived, leading to an improved value for the density, which is then used in the second iteration, and so on until convergence is achieved.

3.2.2 Spin-polarized density functional theory

Local spin density functional theory (LSDFT) is an extension of 'regular' DFT in the same way that restricted and unrestricted HF extensions were developed to deal with systems containing unpaired electrons. In this theory, both the electron density and the spin density are fundamental quantities with the net spin density ($\sigma(\mathbf{r})$) being the difference between the density of up-spin and down-spin electrons:

$$\sigma(\mathbf{r}) = \rho_{\uparrow}(\mathbf{r}) - \rho_{\downarrow}(\mathbf{r}) \tag{3.20}$$

The total electron density is just the sum of the densities for the two types of electron. The exchange-correlation functional is typically different for the two cases, leading to a set of spin-polarized Kohn-Sham equations:

$$\begin{aligned} \left\{ -\frac{\nabla_1^2}{2} - \left(\sum_{A=1}^{M} \frac{Z_A}{r_{1A}} \right) + \int \frac{\rho(\mathbf{r}_2)}{r_{12}} d\mathbf{r}_2 + V_{\mathrm{XC}}[\mathbf{r}_1, \sigma] \right\} \psi_i^{\sigma}(\mathbf{r}_1) &= \varepsilon_i^{\sigma} \psi_i^{\sigma}(\mathbf{r}_1) \\ \sigma &= \alpha, \beta \end{aligned} \tag{3.21}$$

This leads to two sets of wave functions, one for each spin, similar to spin-unrestricted Hartree-Fock (UHF) theory of Pople & Nesbet (1954). The brief introduction of UHF theory is shown in Appendix A.

3.2.3 Local density approximation

The exchange-correlation functional is clearly key to the success of the density functional approach. One reason why DFT is so appealing is that even relatively

simple approximations to the exchange-correlation functional can give favorable results. The simplest way to obtain this contribution uses the so-called *local density approximation* (LDA; the acronym LSDA is also used, for local spin density approximation), which is based upon a model called the uniform electron gas, in which the electron density is constant throughout all space. Thomas (1927) and Fermi (1928) independently studied the uniform electron gas in the early 1920s. Further, the dependence of the kinetic and exchange energy on the density of the electron gas was extracted by Dirac (1930) and expressed in terms of a local functions of the density. This suggests that in an inhomogeneous system, it is possible to approximate the functional as an integral over a local function of the charge density. Using the kinetic and exchange energy densities of the non-interacting uniform electron gas leads to

$$E_{\mathrm{KE}}[\rho(\mathbf{r})] = 2.87 \int \rho^{5/3}(\mathbf{r}) d\mathbf{r} \tag{3.22}$$

and

$$E_{\mathrm{XC}}[\rho(\mathbf{r})] = 0.74 \int \rho^{4/3}(\mathbf{r}) d\mathbf{r} \tag{3.23}$$

These results are highly suggestive of a representation for E_{XC} in an inhomogeneous system. The total exchange-correlation energy, E_{XC}, for our system can then be obtained by integration over all space:

$$E_{\mathrm{XC}}[\rho(\mathbf{r})] = \int \rho(\mathbf{r}) \varepsilon_{\mathrm{XC}}(\rho(\mathbf{r})) d\mathbf{r} \tag{3.24}$$

$\varepsilon_{\mathrm{XC}}(\rho(\mathbf{r}))$ is the exchange-correlation energy per electron as a function of the density in the uniform electron gas. The exchange-correlation functional is obtained by differentiation of this expression:

$$V_{\mathrm{XC}}[\mathbf{r}] = \rho(\mathbf{r}) \frac{d\varepsilon_{\mathrm{XC}}(\rho(\mathbf{r}))}{d\rho(\mathbf{r})} + \varepsilon_{\mathrm{XC}}(\rho(\mathbf{r})) \tag{3.25}$$

In the LDA it is assumed that at each point $\mathbf{r}$ in the inhomogeneous electron distribution (i.e. in the system of interest) where the density is $\rho(\mathbf{r})$ then $V_{\mathrm{XC}}[\rho(\mathbf{r})]$ and $\varepsilon_{\mathrm{XC}}(\rho(\mathbf{r}))$ have the same values as in the homogeneous electron gas. In other words, the real electron density surrounding a volume element at position $\mathbf{r}$ is replaced by a constant electron density with the same value as at $\mathbf{r}$. However, this 'constant' electron density is different for each point in space.

The exchange-correlation energy per electron of the uniform electron gas is known accurately for all densities of practical interest from various approaches such as quantum Monte Carlo methods [Ceperley & Alder (1980)]. In order to be of practical use, this exchange-correlation energy density is then expressed in an analytical form that makes it amenable to computation. It is usual to express $\varepsilon_{\mathrm{XC}}(\rho(\mathbf{r}))$ as an analytical function of the electron density and to consider the exchange and correlation contributions separately. However, some analytical expressions for the combined exchange and correlation energy density do exist, such as the expression of Gunnarsson & Lundqvist (1976). The relatively simple expression of Slater (1974) is commonly used for the exchange-only energy under the LDA. In general, more attention has been paid to the correlation contribution, for which there is no such simple functional form. Perdew & Zunger (1981) suggested the parametric relationship for the correlation contribution. This result applies when the number of up spins equals the number of down spins and so is not applicable systems with an odd number of electrons. The correlation energy functional was also considered by Vosko *et al.* (1980), whose expression has a very complex form.

The overall procedure to achieve self-consistency, the general strategy of solving the Kohn-Sham equations, is very reminiscent of that used in HF theory, involving first an initial guess of the density by superimposing atomic densities, construction of the Kohn-Sham and overlap matrices, and diagonalization to give the eigenfunctions and eigenvectors from which the Kohn-Sham orbitals can be constructed and thus the density for the next iteration. This cycle continues until convergence is achieved.

3.2.4 Beyond the LDA: Gradient-corrected functionals

The most important feature of DFT is probably the way in which it directly incorporates exchange and correlation effects; the latter in particular are only truly considered in the more complex, post-HF approaches such as configuration interaction (CI) or many-body perturbation theory. Despite its simplicity the LDA performs surprisingly well. However, the LDA has been shown to be clearly inadequate for some problems and for this reason extensions have been developed.

The most common method is to use gradient-correct, 'non-local' functionals which depend upon the gradient of the density at each point in space and not just on its value. These gradient corrections are typically divided into separate exchange and correlation contributions. A variety of gradient corrections have been proposed in the literature. One of the popular gradient correction is generalized gradient approximation (GGA) which is proposed by Langreth & Perdew (1980) and by Perdew & Wang (1986, 1992), labeled 'PW86' and 'PW91' in general computational codes. In the GGA, a functional form is adopted which ensures the normalization condition and that the exchange hole is negative definite [Perdew & Wang (1986)]. This leads to an energy functional that depends on both the density and its gradient but retains the analytic properties of the exchange correlation hole inherent in the LDA. The typical form for a GGA functional is:

$$E_{\mathrm{XC}}[\rho(\mathbf{r})] \approx \int \rho(\mathbf{r})\varepsilon_{\mathrm{XC}}(\rho, \nabla\rho)d\mathbf{r} \tag{3.26}$$

The gradient correction to the exchange functional proposed by Becke is also popular [Becke (1988a, 1992)] and this correction corrects the local spin density approximation (LSDA) result. Two particular features of this corrected functional form are that in limit $r \to \infty$ the limiting form of the exchange-correlation integral is correctly achieved and that it uses just a single parameter. The correlation functional of Lee, Yang and Parr is also widely used [Lee *et al.* (1988)]. In their scheme, the expression of the corrected correlation functional provides both local and non-local components within a single expression and the gradient contribution to second order. A combination of the standard LSDA exchange result with the Becke gradient-exchange correction and the Lee-Yang-Parr correlation functional is currently a popular choice, commonly abbreviated to BLYP.

3.3 Hybrid HF/DFT methods

As we stated earlier, a key feature of DFT is the way in which correlation effects are incorporated from the beginning, unlike HF theory. However, it is important to recognize that HF theory does provide an essentially exact means of treating the exchange contribution. One potentially attractive option is thus to add a

correlation energy derived from DFT (e.g. the LDA) to the HF energy. In such an approach, the exchange-correlation energy is written as a sum of the exact exchange term together with the correlation component from the LDA. This 'exact' exchange energy is obtained from the Slater determinant of the Kohn-Sham orbitals. Becke has proposed a strategy which does seem to have much promise Becke (1993a,b). In his approach the exchange-correlation energy E_{XC} is written in the following form:

$$E_{\mathrm{XC}} = \int_0^1 \mathcal{U}_{\mathrm{XC}}^{\lambda} d\lambda \tag{3.27}$$

Equation (3.27) contains a coupling parameter λ, which takes values from 0 to 1. A value of zero corresponds to a system where there is no Coulomb repulsion $\mathcal{U}_{\mathrm{XC}}$ between the electrons (i.e. the Kohn-Sham non-interacting reference state). As λ increases to 1 the interelectronic Coulomb repulsion is introduced until $\lambda = 1$, which corresponds to the 'real' system with full interactions. For all values of λ the electron density is the same and equal to the density of the real system. It is not practical to perform this integral analytically and so it must be approximated. The simplest approximation is a linear interpolation:

$$E_{\mathrm{XC}} = \frac{1}{2}(\mathcal{U}_{\mathrm{XC}}^{0} + \mathcal{U}_{\mathrm{XC}}^{1}) \tag{3.28}$$

When $\lambda = 0$ we have $\mathcal{U}_{\mathrm{XC}}^{0}$, which is the exchange-correlation potential energy of the non-interacting reference system. As there are no electronic interactions in this system, there is no correlation term and so $\mathcal{U}_{\mathrm{XC}}^{0}$ corresponds to pure exchange energy of the Kohn-Sham determinant and can be determined exactly. $\mathcal{U}_{\mathrm{XC}}^{1}$ is the exchange-correlation potential energy of the full-interacting real system. Becke proposed that this should be calculated using the LSDA. This potential energy (note that it is not the total energy, E) is available from:

$$\mathcal{U}_{\mathrm{XC}}^{1} \approx \mathcal{U}_{\mathrm{XC}}^{\mathrm{LSDA}} = \int u_{\mathrm{XC}}[\rho_{\alpha}(\mathbf{r}), \rho_{\beta}(\mathbf{r})] d\mathbf{r} \tag{3.29}$$

u_{XC} is the exchange-correlation potential energy density of an electron gas for which appropriate expressions are available.

This so-called 'half-and-half' theory proved to be significantly better than the alternative methods based on mixing exact exchange and correlation energies.

In a refinement of the scheme, Becke recognized that there were problems with the model when $\lambda = 0$. These problems arise because the electron gas model is not appropriate near this exchange-only limit for molecular bonds. Hence a key feature of Becke's modified model is to eliminate the term $\mathcal{U}_{\mathrm{XC}}^{0}$ and to write the exchange-correlation energy as the following linear combination:

$$E_{\mathrm{XC}} = E_{\mathrm{XC}}^{\mathrm{LSDA}} + a_0(E_{\mathrm{X}}^{\mathrm{exact}} - E_{\mathrm{X}}^{\mathrm{LSDA}}) + a_{\mathrm{X}}\Delta E_{\mathrm{X}}^{\mathrm{GC}} + a_{\mathrm{C}}\Delta E_{\mathrm{C}}^{\mathrm{GC}} \tag{3.30}$$

In Equation (3.30), $E_{\mathrm{X}}^{\mathrm{exact}}$ is the exact exchange energy (obtained from the Slater determinant of the Kohn-Sham orbitals), $E_{\mathrm{X}}^{\mathrm{LSDA}}$ is the exchange energy under the LSDA, $\Delta E_{\mathrm{X}}^{\mathrm{GC}}$ is the gradient correction for exchange and $\Delta E_{\mathrm{C}}^{\mathrm{GC}}$ is the gradient correction for correlation. a_0, a_{X} and a_{C} are empirical coefficients obtained by least-squares fitting to experimental data. Their values are $a_0 = 0.20$, $a_{\mathrm{X}} = 0.72$ and $a_{\mathrm{C}} = 0.81$. Hybrid functionals of this type are now very widely used in chemical applications with the B3LYP or B3PW functionals (in which the parameterisation is as given above but with a different GGA treatment of correlation [Lee *et al.* (1988); Perdew & Wang (1992)] being the most notable). In Becke's original paper, his own gradient correction for exchange was used together with a gradient correction for correlation suggested by Perdew and Wang and the resultant three parameter energy functional is:

$$E_{\mathrm{XC}} = E_{\mathrm{XC}}^{\mathrm{LSDA}} + 0.2(E_{\mathrm{X}}^{\mathrm{exact}} - E_{\mathrm{X}}^{\mathrm{LSDA}}) + 0.72\Delta E_{\mathrm{X}}^{\mathrm{B88}} + 0.81\Delta E_{\mathrm{C}}^{\mathrm{PW91}} \tag{3.31}$$

where $\Delta E_{\mathrm{X}}^{\mathrm{B88}}$ and $\Delta E_{\mathrm{C}}^{\mathrm{PW91}}$ are widely used GGA corrections [Becke (1988b); Perdew & Wang (1992)] to the LDA exchange and correlation energies respectively. This hybrid B3PW method is the most important tool for my forthcoming theoretical works.

Chapter 4

Calculations on perfect bulks and slabs of CaF_2 and BaF_2 crystals

Introduction

In this Chapter, firstly, in order to compare the various type Hamiltonians, the results of detailed calculations for bulk properties and the electronic structure of the cubic phase of CaF_2 and BaF_2 alkaline-earth fluoride crystals are documented and discussed. These are obtained using both *ab inito* Hartree-Fock (HF) and density functional theory (DFT) applying a number of different exchange-correlation functionals including hybrid (B3PW and B3LYP) exchange techniques. Results, obtained for seven methods, are compared with available experimental data. Great attention is paid to the calculated optical band gap which is responsible for many observed crystal properties (*e.g.* optical absorption). According to the comparison among these seven theoretical methods, I chose the best method which gives the best agreement with experiment for the lattice constant, bulk modulus and optical band gap for future calculations.

In a second part of this chapter, as a basis for forthcoming defect calculations in the surface regions of CaF_2 and BaF_2, I also presented theoretical investigations using the hybrid B3PW method for the pure (111), (110) and (100) surfaces.

4.1 Method of calculations

All numerical calculations dealing with the CaF_2 and BaF_2 electronic structures were performed by the CRYSTAL-2003 computer code [Saunders *et al.* (2003)]. In my calculations, I used several quite different methods: ′pure′ HF and different DFT type *a posteriori* electron correlation corrections to the total energy [Causa & Zupan (1994)]. In DFT computations, the local density approximation (LDA) scheme with the Dirac-Slater exchange [Dirac (1930)] and Vosko-Wilk-Nusair correlation [Vosko *et al.* (1980)] energy functionals have been used as well as a set of generalized gradient approximation (GGA) exchange and correlation functionals as suggested by Perdew and Wang (PW) [Perdew & Wang (1986, 1992)], by Perdew, Burke and Ernzernhof (PBE) [Burke & Ernzerhof (1996)], and lastly by the Becke exchange potential [Becke (1988b)] combined with the correlation potential by Lee, Yang and Parr (BLYP) [Lee *et al.* (1988)]. Also calculations using the hybrid functionals [Becke (1993a)] mixing the Fock exchange and Becke's gradient corrected exchange functional have been performed. Two versions of the gradient corrected correlation potentials together with hybrid exchange potentials have been employed: by Perdew and Wang (B3PW), or by Lee, Yang and Parr (B3LYP).

The CRYSTAL-2003 code employs Gaussian-type functions (GTF) localized at atoms as the basis for an expansion of the crystalline orbitals. In order to employ the LCAO-GTF (linear combination of atomic orbitals) method, it is desirable to have optimized basis sets (BS). In my calculations for CaF_2, I applied the basis sets developed by Catti *et al.* (1991). The basis set of F atoms, for BaF_2, is the same as that in CaF_2. For Ba, the BS optimization for $BaTiO_3$ perovskite was developed and discussed in [Eglitis *et al.* (2004); Piskunov *et al.* (2004)]. The Hay-Wadt small-core effective core pseudopotential (ECP) was adopted for the Ba atom [Hay & Wadt (1985)]. The small-core ECP replaces only inner core orbitals, but orbitals for subvalence electrons as well as for valence electrons are calculated self-consistently. In the present thesis, I used this BS for the Ba atom. The basis sets are believed to be transferable, so that, once determined for some chemical constituents, they may be applied successfully in calculations for a variety of chemical substances where the latter participates. Besides giving

a reasonable lattice constant [Piskunov *et al.* (2004)], the basis set for Ba also allowed us to achieve excellent results for the $BaTiO_3(001)$ surface relaxation and surface band structure [Eglitis *et al.* (2004)].

I performed band-structure calculations with $8 \times 8 \times 8 = 512$ k points in the Brillouin zone (BZ). The calculation thresholds N (i.e., the calculation of integrals with an accuracy of 10^{-N}) were chosen as a compromise between the accuracy of the calculations and the large computational time for large cells. They are 7, 8, 7, 7 and 14 for the Coulomb overlap, Coulomb penetration, exchange overlap, the first-exchange pseudo-overlap and the second-exchange pseudo-overlap, respectively [Pisani (1996)]. The convergence criteria for the self-consistent field (SCF) energy and eigenvalues were set to 10^{-10} and 10^{-12} a.u., respectively. An additional advantage of the CRYSTAL-2003 code is that it treats isolated two-dimensional (2D) slabs, without an artificial periodicity in the Z direction perpendicular to the surface, and thereby is a very convenient tool for modeling of CaF_2 and BaF_2 surfaces.

Unlike the (111) neutral surface, the problem in modeling the (100) polar surface is that it consists of charged planes F-F or Ca/Ba. If one assumes fixed ionic charges F^- and Ca^{2+}/Ba^{2+} (which is the case for shell model calculations or ideal ionic crystals), then modeling of the (100) surface exactly as would be obtained from a perfect-crystal cleavage leads either to an infinite macroscopic dipole moment perpendicular to the surface, when the slab is terminated by planes of different kinds (F_2 and Ca/Ba), or to an infinite charge, when it is terminated by the same type of crystalline planes (F_2-F_2 or Ca-Ca/Ba-Ba). It is known that such crystal terminations make the surface unstable [Noguera (2000); Tasker (1979)]. In real quantum-mechanical calculations for a finite-thickness slab terminated by the different kinds of planes, the charge redistribution near the surface arising during the self-consistent-field procedure, could, in principle, compensate the macroscopic dipole moment. On the other hand, in the calculations of slabs terminated by similar planes, the charge neutrality could be easily retained by setting in the computer input an appropriate number of electrons or just put the net charge of the unit cell to zero. However, careful studies [Bottin *et al.* (2003); Noguera (2000); Pojani *et al.* (1999)] demonstrate that these two options are energetically expensive with respect to the dipole moment elimination

via introduction of vacancies. This is why in my calculations I removed half of the F atoms from the F_2-terminated CaF_2 and BaF_2 (100) surfaces.

4.2 Calculations on perfect CaF_2 and BaF_2 bulks

Table 4.1: Optimized lattice constant a_0 (Å), and bulk modulus B (GPa) for CaF_2 and BaF_2.

	Method	LDA	PWGGA	PBE	BLYP	B3PW	B3LYP	HF	Expt
CaF_2	a_0	5.34	5.51	5.52	5.56	5.50	5.52	5.52	5.46[a]
	B	103	88	90	79	85	91	93	82.71[b]
BaF_2	a_0	6.11	6.27	6.28	6.34	6.26	6.30	6.35	6.20[c]
	B	73	63	63	60	61	62	53	57[c]

[a]reference Weast (1976)
[b]reference Nicolav (2000)
[c]reference Leger *et al.* (1995)

As a starting point of my calculations, I have tested how different methods reproduce the experimentally observable bulk properties – the lattice constant a_0 and the bulk modulus B [Leger *et al.* (1995); Nicolav (2000); Weast (1976)]. For CaF_2, the LDA calculation underestimates a_0 by 2.2% and overestimates B by 24.5%. The HF method without any correlation corrections to the total energy overestimates both a_0 (by 1.1%) and B (by 12.4%). DFT with the GGA correction overestimates a_0 by 0.9% and B by 6.4%. Lastly, the hybrid B3PW method gives the best result for the lattice constant a_0 (overestimates only by 0.7%) and also for B (overestimates by 2.7%) (see Table 4.1). For the BaF_2 bulk, the PWGGA and PBE calculations, like the CaF_2 case, overestimate both a_o and B. However, the pure HF method, unlike the CaF_2 case, overestimates a_o by 2.4% and underestimates B by 7.0%. Finally, although we can't determine the best theoretical method for BaF_2 calculations like the CaF_2 case, as a whole, the hybrid B3PW method gives the better results for the lattice constant (overestimates by 1.0%) and the bulk modulus (overestimates by 7.0%) (see Table 4.1).

Table 4.2: Static (Mulliken) charges (Q in e) of atoms and bond populations (P in me) for bulk CaF_2 and BaF_2 calculated by various methods.

Atom	Q (e) P (me)	LDA	PWGGA	PBE	BLYP	B3PW	B3LYP	HF
Ca^{2+}	Q	+1.728	+1.769	+1.771	+1.776	+1.803	+1.805	+1.895
F^-	Q	-0.864	-0.885	-0.886	-0.888	-0.902	-0.903	-0.948
F-Ca	P	-28	-8	-6	-8	-10	-12	-18
F-F	P	-38	-20	-18	-18	-22	-22	-24
Ba^{2+}	Q	+1.827	+1.828	+1.827	+1.844	+1.845	+1.859	+1.906
F^-	Q	-0.914	-0.914	-0.914	-0.922	-0.923	-0.930	-0.953
F-Ba	P	-52	-34	-32	-28	-38	-36	-42
F-F	P	-2	0	+2	+2	-2	0	-2

To characterize the chemical bonding and covalency effects, I used a standard Mulliken population analysis for the effective atomic charges Q and other local properties of electronic structures (bond orders, atomic covalencies and full valencies) as described e.g. in Refs. [Bochicchio & Reale (1993); Catlow & Stoneham (1983)]. Table 4.2 presents the calculated results of the effective atomic charges and bond populations in CaF_2 and BaF_2 bulks. The effective charges for Ca/Ba and F ions are only slightly smaller than the formal ionic charges (+2 e and -e, respectively). This arises due to the high ionic nature of the Ca/Ba - F chemical bonding. Note that these results are close for all methods used. The most obvious difference is between the effective charges for the metal ions calculated by LDA (Ca: +1.728 e; Ba: +1.827 e) and HF (Ca: +1.895 e; Ba: +1.906 e). According to the calculations of the effective atomic charges, we can see that BaF_2 has a higher ionic degree than CaF_2 and it is in agreement with the fact that the metallic property of Ba is stronger than that of Ca. Obviously, there is practically no chemical bonding between Ca/Ba-F or F-F, since the relevant bond populations are even negative, which indicates a repulsion. Figure 4.1 shows the charge density map of the CaF_2 bulk from the (110) side view obtained with the hybrid

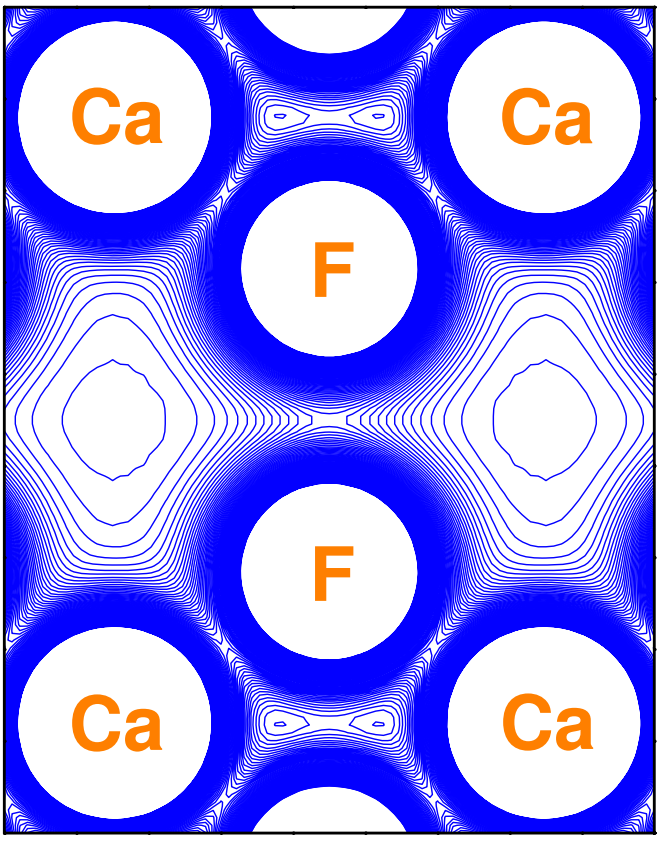

Figure 4.1: Charge density map of the CaF_2 bulk from the (110) side view calculated by means of the hybrid B3PW method. Isodensity curves are drawn from 0 to 0.1 e/bohr^3 with an increment of 0.001 e/bohr^3.

B3PW method. Figure 4.1 confirms that the charge density between atoms is very small and in agreement with the charge and bond population calculations, reflecting the high degree of ionic bonding in this crystal.

The optical band gaps of two alkaline-earth fluorides obtained using various functionals are summarized in Tables 4.3 and 4.4. Experimentally, the direct band gap for the CaF_2 bulk is 12.1 eV and the indirect band gap is estimated to be 11.8 eV [Rubloff (1972)]. It is a well-known fact that the DFT-LDA calculation underestimates the band gap by a factor of typically two. According to my calculations, the indirect band gap (X $\rightarrow$ Γ) using the LDA method is 8.44 eV

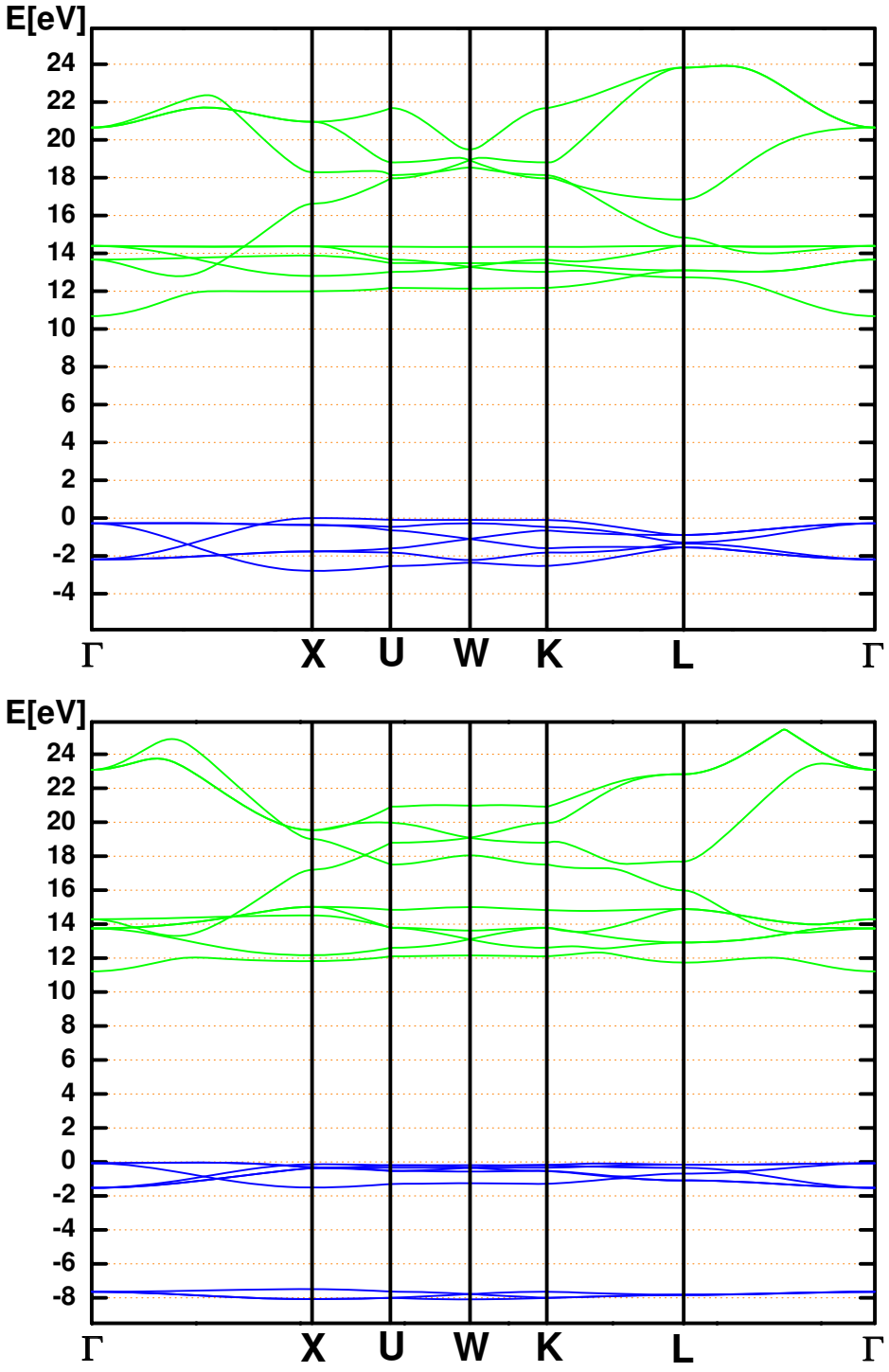

Figure 4.2: Electronic band structures of CaF_2 and BaF_2 bulks calculated by means of the hybrid B3PW method.

Table 4.3: The calculated optical gaps (in eV) for the CaF_2 bulk. Experimentally, the direct band gap is 12.1 eV and the indirect band gap is equal to 11.8 eV [Rubloff (1972)].

	Optical gap	LDA	PWGGA	PBE	BLYP	B3PW	B3LYP	HF
CaF_2	$\Gamma \rightarrow \Gamma$	8.72	8.51	8.45	8.40	10.96	10.85	20.77
	$X \rightarrow X$	9.30	9.33	9.30	9.28	11.99	11.93	22.72
	$U \rightarrow U$	9.60	9.58	9.55	9.52	12.27	12.20	23.07
	$W \rightarrow W$	9.56	9.55	9.52	9.49	12.23	12.16	23.00
	$L \rightarrow L$	11.41	10.82	10.77	10.64	13.63	13.54	24.90
	$X \rightarrow \Gamma$	8.44	8.22	8.20	8.16	10.68	10.57	20.43
	$U \rightarrow \Gamma$	8.55	8.34	8.29	8.24	10.78	10.67	20.53
	$W \rightarrow \Gamma$	8.54	8.33	8.28	8.24	10.78	10.66	20.55
	$L \rightarrow \Gamma$	9.34	9.07	9.02	8.96	11.58	11.46	21.50

(see Table 4.3), considerably less than the value obtained experimentally. On the other hand, the band gap obtained through the pure-HF calculation usually greatly overestimates the experimental value [Pisani (1996)]. Indeed, the result of our pure-HF calculation for indirect band gap ($X \rightarrow \Gamma$) (20.43 eV) confirms this rule (see Table 4.3). In Chapter 3, I introduced a possible solution of this problem, the use of so-called hybrid functionals (a combination of the non-local HF exchange, DFT exchange and the GGA correlation functional). Examples are so-called B3PW and B3LYP, which nowadays are extremely popular in quantum chemistry of molecules and recently have been applied to periodic-structure *ab inito* calculations of a wide range of crystalline materials [Muscat *et al.* (2001)]. Also for the CaF_2 band structure, the hybrid B3PW and B3LYP methods give the best results (see Table 4.3). Namely, according to my calculations, the indirect band gap ($X \rightarrow \Gamma$) using B3PW is 10.68 eV (see Figure 4.2), and 10.57 eV by the B3LYP functional, in good agreement with experiment. For BaF_2, the direct band gap ($\Gamma \rightarrow \Gamma$) calculated by means of the hybrid methods B3PW (11.30 eV) and B3LYP (11.19 eV) are much better agreement with experiment

Table 4.4: The calculated optical gaps (in eV) for the BaF_2 bulk. Experimentally, the direct band gap is 11.0 eV [Rubloff (1972)].

	Optical gap	LDA	PWGGA	PBE	BLYP	B3PW	B3LYP	HF
BaF_2	$\Gamma \rightarrow \Gamma$	8.94	8.85	8.81	8.75	11.30	11.19	20.82
	$X \rightarrow X$	9.61	9.54	9.50	9.53	11.97	11.94	21.64
	$U \rightarrow U$	9.92	9.87	9.83	9.85	12.29	12.27	21.94
	$W \rightarrow W$	9.98	9.91	9.87	9.92	12.35	12.34	22.14
	$L \rightarrow L$	9.77	9.49	9.44	9.41	11.91	11.88	21.48
	$X \rightarrow \Gamma$	9.03	8.90	8.85	8.78	11.36	11.24	20.96
	$U \rightarrow \Gamma$	9.04	8.96	8.91	8.83	11.40	11.28	20.91
	$W \rightarrow \Gamma$	9.10	8.95	8.90	8.83	11.42	11.30	21.01
	$L \rightarrow \Gamma$	8.97	8.95	8.91	8.86	11.39	11.28	20.86

(11.00 eV) [Rubloff (1972)], such as my calculations using other methods and the recent result of Khenata *et al.* (2005) (7.49 eV) using the FPLAPW (full-potential linearized augmented-plane wave) method. My result for the BaF_2 band gap is also in line with the early conclusion by Muscat *et al.* (2001) that the hybrid scheme allows us to achieve the best agreement with experiment for the band gaps of a variety of materials.

I calculated the total and partial density of states (DOS) of the cubic CaF_2 and BaF_2 using the hybrid B3PW method. As they are seen in Figure 4.3, the upper valence bands (VB) mainly consist of F *p*-orbitals, whereas the conduction band (CB) bottom consists essentially of Ca/Ba *d*-orbitals. The orbital contribution from F atoms is small in this energy range. This conclusion fits to the previous theoretical study [Catti *et al.* (1991)], but it contrasts with the results of Evarestov *et al.* (1989), which show major contributions from Ca *s*- and F *s*-orbitals. My DOS calculations also have a small difference to the results of Rubloff (1972), which show the CB bottom at Γ point is primarily of Ca 4*s* character, but the second conduction band at Γ point and the CB bottom at X point mainly consist of Ca 3*d* orbitals, as mentioned in Chapter 2. My calculations

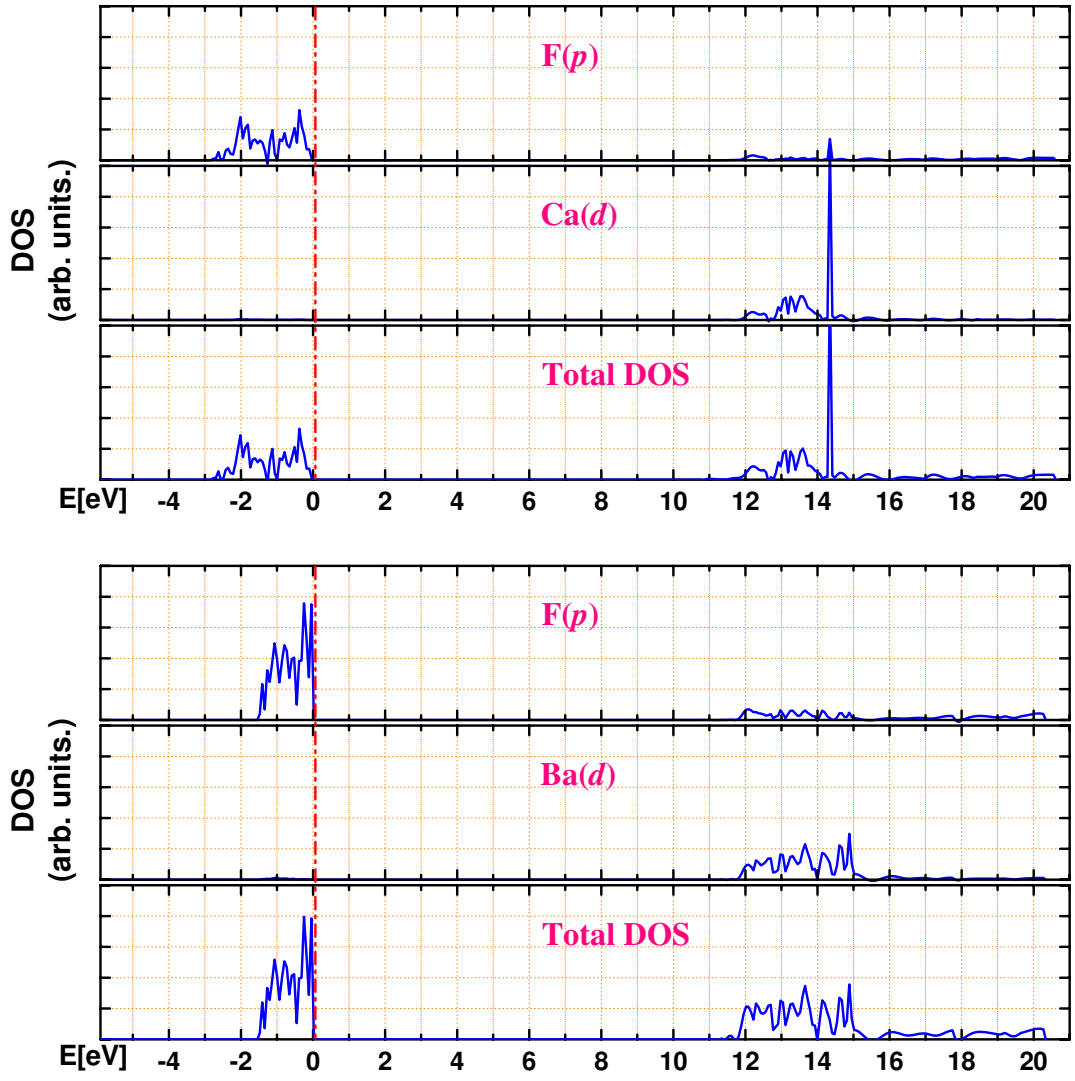

Figure 4.3: The calculated total and projected density of states (DOS) for CaF_2 and BaF_2 bulks by means of the hybrid B3PW method.

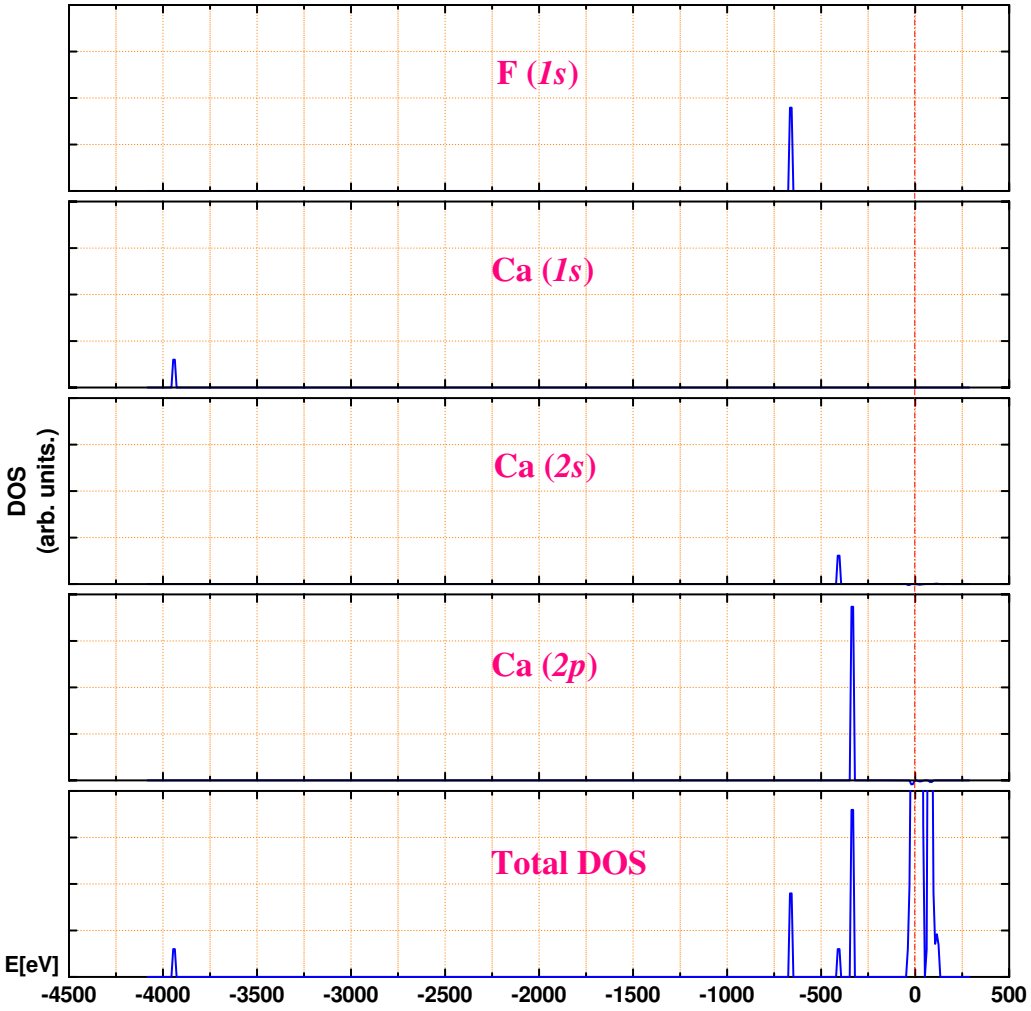

Figure 4.4: The calculated total and projected density of states (DOS) in deep energy range for the CaF_2 bulk by means of the hybrid B3PW method.

are based on the LCAO-GTF within both HF and DFT methods, in which the basis sets don't describe the atomic orbitals as the true atomic orbitals in real crystals. We can't say that one band consists of one type orbital (e.g. 1s, 2s, 2p, ...) completely, and we can only say that one type orbitals do the *most* or *main* contributions to one band, especially for CB and outer VB. My DOS calculations for CB bottom show that there is also a small contribution from Ca outer *s*-orbitals. However, this contribution is much smaller than that of Ca *d*-orbitals. In order to investigate more detailed electronic information, I also calculated the DOS in the deeper energy range for the CaF_2 bulk, as we can see in Figure 4.4. The analysis of DOS calculations shows that, Ca 1*s*- and F 1*s*-orbitals form the deepest (about -4000 eV) and second-deepest (around -700 eV) bands, respectively, and the bands located at around -300 eV consist of Ca 2*s*- and 2*p*-orbitals. For these deeper bands are very narrow, we can consider that these bands are formed by a single type of atomic orbitals approximately.

4.3 Calculations on perfect CaF_2 and BaF_2 slabs

4.3.1 Surface relaxations

I started my calculations from the case of the CaF_2 and BaF_2 (111) surfaces, which are known to be experimentally stable. Let us, for the analysis, look at the particular B3PW results, since they gave the best agreement with experiment for the lattice constant and bulk modulus. The structure of the CaF_2 (111) surface and directions of atomic displacements are illustrated in Figure 4.5. I found, in contrast to Puchin *et al.* (2001), that the atomic displacements for the (111) surface are not fully negligible. The calculated displacements of the atoms by the HF method are < 0.01 Å in Ref.[Puchin *et al.* (2001)], whereas according to my B3PW calculations, F atoms in the upper sublayer of the top (111) surface layer are relaxed inward by 0.05 Å (see Table 4.5). Recently the CaF_2 (111) surface structure was investigated by means of low energy electron diffraction (LEED) approach [Vogt *et al.* (2005)]. The CaF_2 (111) surface deviates only insignificantly from a truncated fluorite bulk lattice with F-Ca-F layer structure, the largest displacement was the inward shift of the topmost layer of fluorine anions by

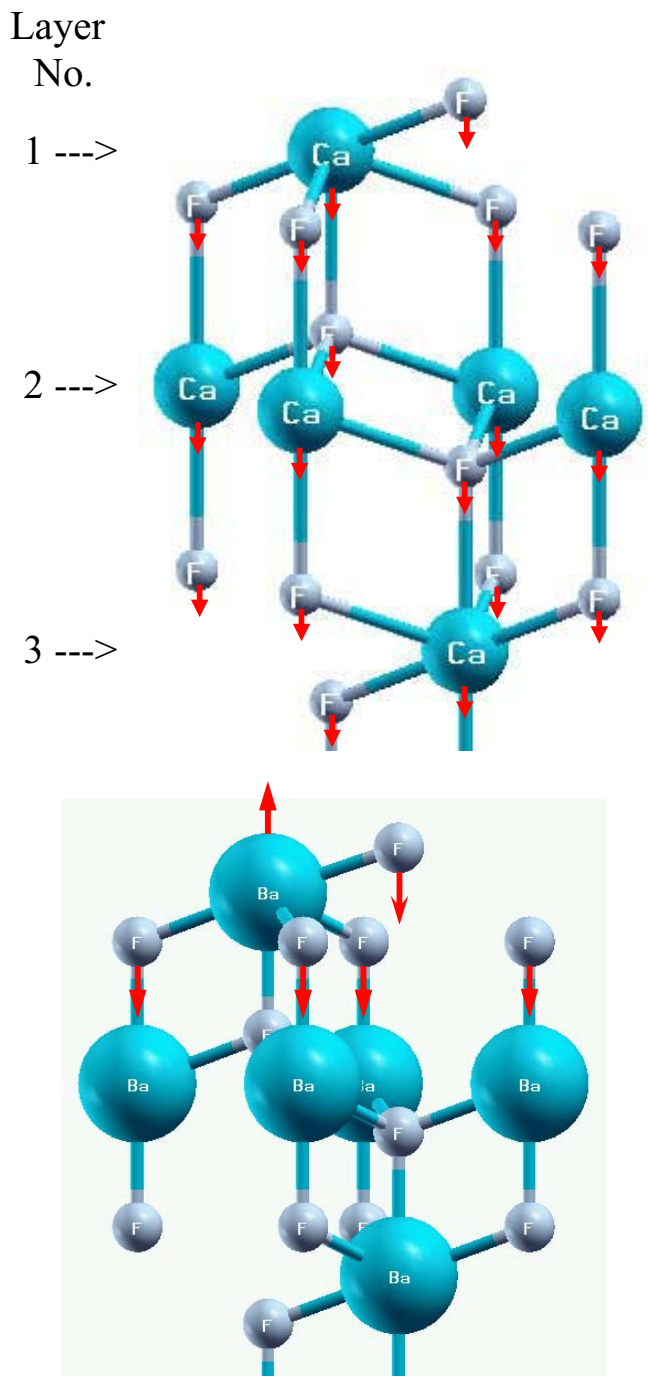

Figure 4.5: Schematic sketch of CaF_2 and BaF_2 (111) surface structures. Layer numbering introduced in this figure is used in Table 4.5. Arrows indicate the calculated displacement directions of Ca, Ba and F atoms.

Table 4.5: Atomic relaxations of slabs (containing 9 layers for CaF_2 and 15 layers for BaF_2) in the (111) direction (in percent of the lattice constant: $a_0 = 5.50$ Å for CaF_2; $a_0 = 6.26$ Å for BaF_2), calculated by means of the hybrid B3PW method. Positive sign corresponds to outward atomic displacement (toward the vacuum).

Layer	Atom	CaF_2: ΔZ (%)	BaF_2: ΔZ (%)
1	F	-0.90	-0.87
	M (Ca/Ba)	-0.68	+0.17
	F	-0.78	-0.37
2	F	-0.34	+0.73
	M (Ca/Ba)	-0.41	+0.19
	F	-0.36	-0.07
3	F	-0.34	+0.25
	M (Ca/Ba)	-0.28	+0.01
	F	-0.23	-0.15
4	F	-0.19	—
	M (Ca/Ba)	-0.14	—
	F	-0.09	—

0.03±0.06 Å. The structure of the BaF_2 (111) surface and directions of atomic displacements is also shown in Figure 4.5. The calculated atomic displacements in the upper three layers (nine sublayers) are listed in Table 4.5. According to my calculations, the relaxation of F atoms in the upper sublayer of the top (111) surface layer is inward by 0.054 Å, and is comparable with the experiment (0.12±0.07 Å) [Vogt *et al.* (2005)]. The experiment also shows that the positions of Ba atoms as well as those of the second fluoride sublayer in this topmost F-Ba-F sheet are almost identical to their bulk values. My results of the displacements of Ba atoms and lower F atoms in the topmost F-Ba-F layer are in agreement with this experiment. The surface-layer relaxation of F atoms in the BaF_2 upper sublayer has the same direction and comparable magnitude as I found for CaF_2. However, the direction of atomic displacements for Ba atoms in the topmost

F-Ba-F sheet is opposite to the relevant CaF_2 case (see Figure 4.5).

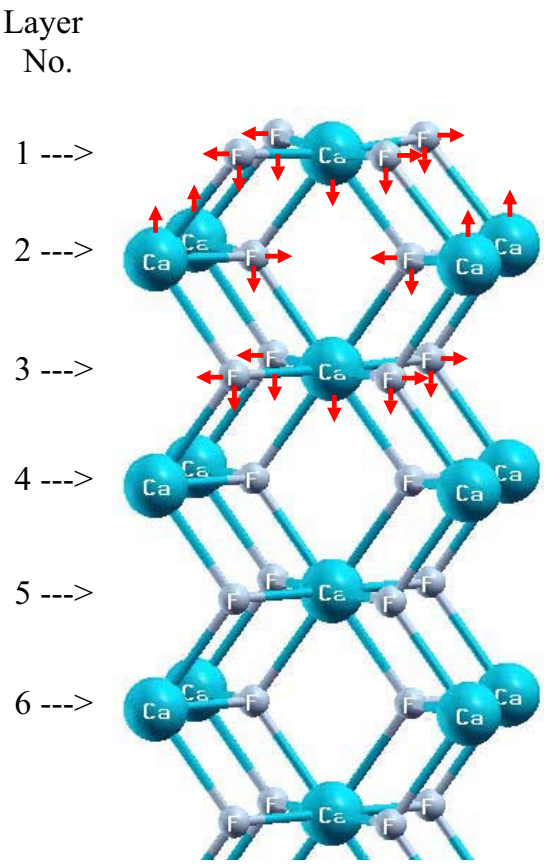

Figure 4.6: Schematic sketch of the CaF_2 (110) surface structure. For the CaF_2 (110) surface, there appears an additional degree of freedom in the Y direction for atomic displacements. Layer numbering introduced in this figure is used in Table 4.6. Arrows indicate the calculated displacement directions of Ca and F atoms.

As a next step, I optimized the slab atomic structure for the case of the CaF_2 (110) surface. I performed the geometry relaxation for a slab containing 15 layers (see Table 4.6). For the CaF_2 (110) surface there appears an additional degree of freedom for the atomic displacements in the direction Y (see Figure 4.6). Ca atoms at the CaF_2 (110) surface upper layer move inward (toward the bulk) by 3.35% of a_0, whereas the displacement of upper layer Ca atoms in the case of

Table 4.6: Atomic relaxations of the CaF_2 slab containing 15 layers in the (110) direction (in percent of the lattice constant: a_0 = 5.50 Å), calculated by means of the hybrid B3PW method. ΔY is the relative displacement (in percent of a_0) between two F atoms. Negative sign means the shortening of the F-F distance.

Layer	Atom	ΔY (%)	ΔZ (%)
1	F	+3.21	-0.87
	Ca	0	-3.35
2	F	-0.14	-0.83
	Ca	0	+0.80
3	F	+0.08	-0.26
	Ca	0	-0.88
4	F	-0.03	-0.40
	Ca	0	-0.13
5	F	+0.03	-0.22
	Ca	0	-0.33
6	F	-0.03	-0.18
	Ca	0	-0.13
7	F	+0.03	-0.08
	Ca	0	-0.09

the CaF_2 (111) termination was only 0.68% of a_0 toward the bulk. Also for the deeper layers, the magnitudes of atomic displacements in the case of the CaF_2 (110) surface are considerably larger than for the CaF_2 (111) surface, see Tables 4.5 and 4.6 for comparison.

Next, I calculated the relaxation of the CaF_2 (100) surface using a slab containing 15 layers (see Figure 4.7). I found, that the relaxation of the CaF_2 (100) surface is considerably stronger than for the (111) and (110) surfaces. F atoms at the upper surface layer are relaxed most noticeably, by 5.65% of a_0 toward the bulk, but also F atoms even at the seventh layer are still considerably displaced, by 0.82% of a_0 inward and by 0.76% of a_0 outward (see Table 4.7). Here, we

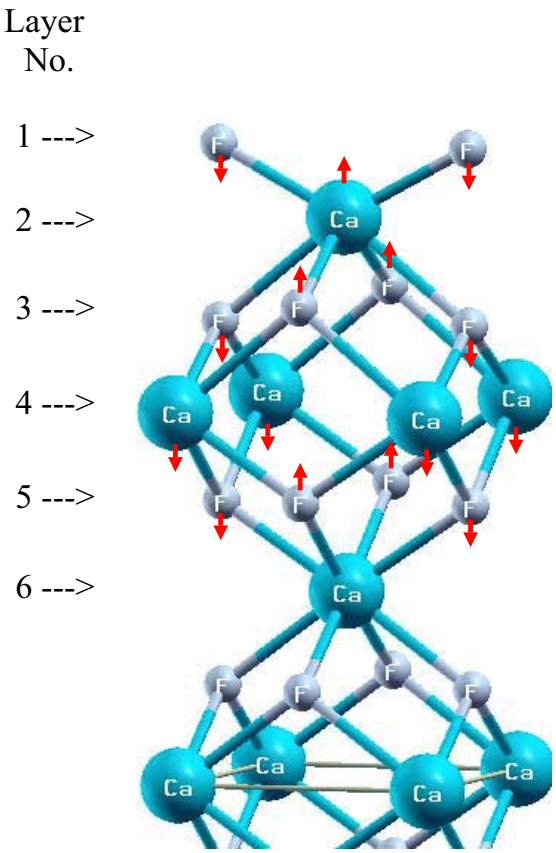

Figure 4.7: Schematic sketch of the CaF_2 (100) surface structure. Layer numbering introduced in this figure is used tin Table 4.7. Arrows indicate the calculated displacement directions of Ca and F atoms.

should note that the two F atoms in deeper layers for each unit cell slab are not equivalent due to the removing of half of F atoms from the F_2-terminated (100) surfaces for avoiding an infinite macroscopic dipole moment or an infinite charge slab (see Figure 4.7).

I also calculated the geometry relaxation for the BaF_2 (110) and (100) slabs. For the (110) surface, Ba atoms in the top layer move inward (towards the bulk) by 3.15% of a_0, whereas the displacement of upper layer Ba atoms in the case of the BaF_2 (111) termination was only 0.17% of a_0 (see Table 4.5 for comparison) backwards from the bulk. Also, for the deeper layers, the magnitudes of atomic

Table 4.7: Atomic relaxations of the CaF_2 slab containing 15 layers in the (100) direction (in percent of the lattice constant: a_0 = 5.50 Å), calculated by means of the hybrid B3PW method. Positive sign corresponds to outward atomic displacement (toward the vacuum).

Layer	Atom	ΔZ (%)
1	F	-5.63
2	Ca	+0.34
3	F	-3.20
	F	+4.03
4	Ca	-0.03
5	F	+1.49
	F	-1.53
6	Ca	-0.07
7	F	-0.82
	F	+0.76

displacements in the case of the (110) surface are considerably larger than for the (111) surface. For the (100) case, F atoms in the top layer are relaxed most noticeably, by 6.53% of a_0 towards the bulk. According to my calculations, like CaF_2, the relaxation of the (100) surface is considerably stronger than for the (111) and (110) surfaces.

4.3.2 Surface electronic structures

All electronic properties for the CaF_2 and BaF_2 slabs in the (111), (110) and (100) have been calculated by means of the hybrid B3PW method. Firstly, let us focus on effective charge and bond population analysis. The cation effective charges in two top CaF_2 (111) surface layers (+1.797 e) and (+1.802 e) turn out to be smaller than in the bulk (+1.803 e), whereas the F charges (-0.891 e) in the upper sublayer of the top surface layer is by 0.011 e larger than in the bulk (-0.902 e). For BaF_2, the charges of Ba atoms in the top (111) surface layer (+1.838 e)

are smaller than in the bulk (+1.845 e) and the F charges (-0.918 e) in the upper sublayer of the top surface layer are larger by 0.005 e than in the bulk (-0.923 e). Changes in the atomic charges in the deeper layers become very small.

The charges of the CaF_2/BaF_2 (110) surface upper-layer F atoms are -0.882 e/-0.908 e, and increase by 0.020 e/0.015 e in comparison to the bulk, and by 0.009 e/0.010 e relative to the (111) surface upper-layer F atoms. The largest charge change is for the CaF_2/BaF_2 (110) surface upper-layer Ca/Ba atoms. Their charges are reduced by 0.041 e/0.042 e in comparison to the bulk charge (+1.803 e/+1.845 e) and are equal to +1.762 e/+1.803 e. Charges in the (110) surface deeper layers become very close to the relevant Ca/Ba and F charges in the bulk.

Static Mulliken charges of atoms for the CaF_2 (100) surface differ from the bulk charges by +0.055 e for the top-layer F atoms and by -0.52 e for the second-layer Ca atoms, which is considerably more than in the cases of the (110) and (111) surfaces. For BaF_2, the top-layer F charge increases by 0.047 e in comparison to the bulk and the charges of Ba atoms in the second layer are reduced by 0.051 e with respect to the bulk.

Bond population analysis between neighbor atoms for the CaF_2 (111) surface shows that the major effect observed here is a strengthening of the Ca-F chemical bond near the surface. The bond population between Ca and F atoms in the upper sublayer of the first surface layer by +12 *me* exceeds the respective bond population value between Ca and F atoms in the bulk. At deeper layers of the CaF_2 (111) surface, the bond population between Ca and F atoms is practically the same as in the bulk. The similar effect, a strengthening of the Ti-O chemical bond near the $SrTiO_3$ (001) surface, was also observed by Heifets *et al.* (2001). We also can observe an increase of the Ca-F chemical bond population near the CaF_2 (100) surface by +18 *me* in comparison to the CaF_2 bulk and thereby a strengthening of the Ca-F chemical bonding. The strengthening of the chemical bonding between Ca and F atoms in the upper surface layer is more pronounced for the CaF_2 (100) surface than for the CaF_2 (111) termination.

I also computed the electronic energy-band structures for the (100), (110) and (111) surfaces using the hybrid B3PW method. The band-structure pictures for CaF_2 are shown in Figure 4.8 and data on the optical band gaps for the (100),

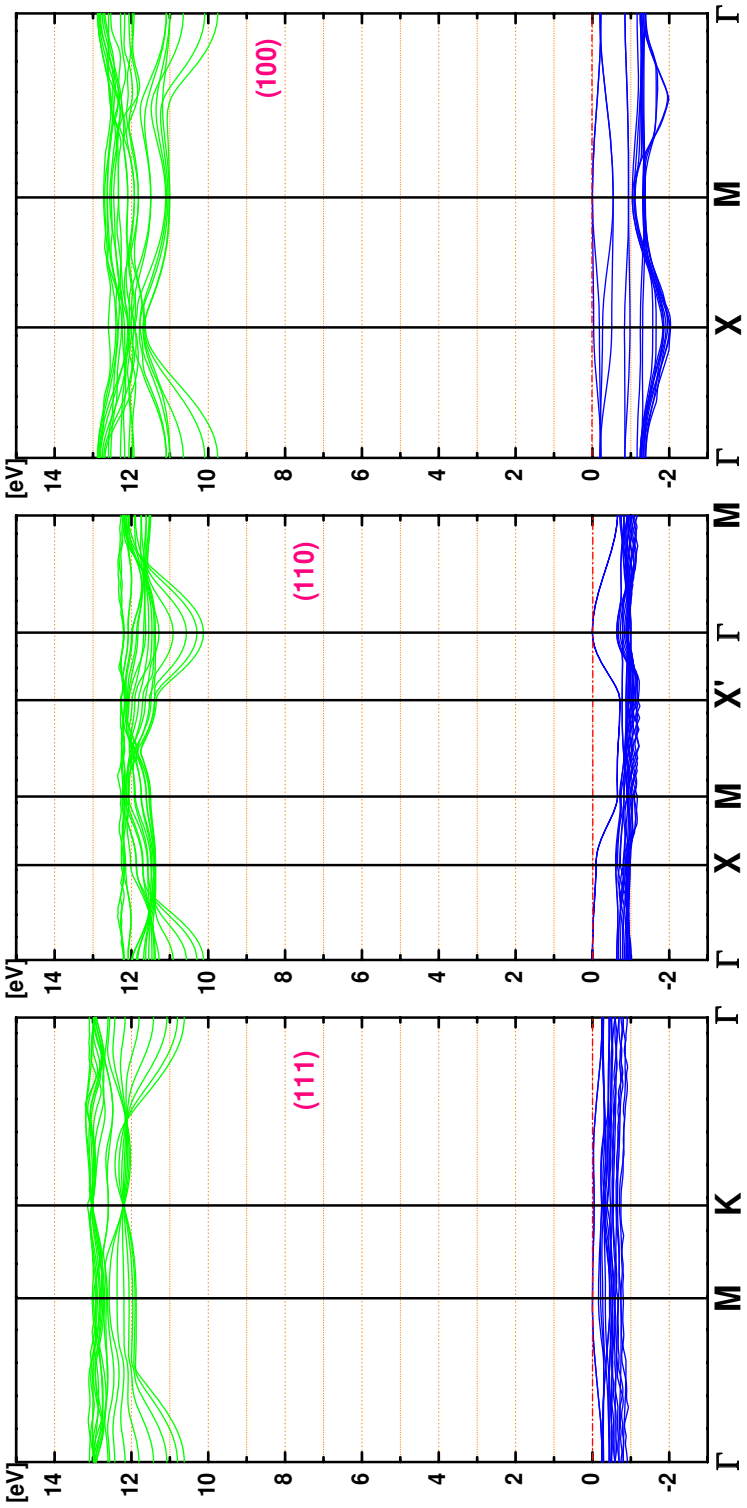

Figure 4.8: Electronic band structures of the (111), (110) and (100) CaF_2 slabs calculated by means of the hybrid B3PW method.

Table 4.8: The calculated direct ($\Gamma \rightarrow \Gamma$) optical band gaps (eV) for the (100), (110) and (111) slabs. All calculations have been performed using the hybrid B3PW method. The last column contains the respective optical band gaps for the bulks.

Slabs	(100)	(110)	(111)	Bulk
CaF_2	9.95	10.13	10.87	10.96
BaF_2	10.29	10.77	10.94	11.30

(110) and (111) CaF_2 and BaF_2 surfaces are collected in Table 4.8. Since the surface band-structure properties for BaF_2 look quite similar to CaF_2, I mainly focus on CaF_2 discussion here. The direct optical band gap for the (111) surface (10.87 eV) is close to the relevant optical band gap value for the CaF_2 bulk (10.96 eV). The direct optical band gaps for the CaF_2 (100) and (110) surfaces (9.95 eV and 10.13 eV, respectively) are considerably reduced in comparison to the CaF_2 bulk.

The DOS calculated using the hybrid B3PW method for the CaF_2 (100), (110) and (111) surfaces are illustrated in Figures 4.9, 4.10 and 4.11, respectively. As we can see in Figure 4.9, the calculated DOS for the CaF_2 (100) surface shows that the (100) surface upper-layer F p-orbitals move upward, toward the Fermi energy, with respect to the F p-orbitals at deeper layers, and this leads to the narrowing of the (100) surface band gap. This finding is in line with the narrowing of the band gaps at the $SrTiO_3$, $BaTiO_3$ and $PbTiO_3$ perovskite (100) surfaces reported by Eglitis *et al.* (2004) and Heifets *et al.* (2001, 2002) and by Padilla and Vanderbilt for the $SrTiO_3$ and $BaTiO_3$ (100) surfaces [Padilla & Vanderbilt (1997, 1998)]. The calculated DOS for the CaF_2 (110) surface shows that the (110) surface first layer F p-orbitals have some states near the Fermi energy, but their magnitudes are rather small (see Figure 4.10). Thereby they contribute to some narrowing of the band gap, but this effect is not so well pronounced than in the case of the CaF_2 (100) surface. From the calculated DOS for the CaF_2 (111) surface, we can conclude that the F p-orbitals in the upper layer of the CaF_2 (111) surface have one large peak near the Fermi energy, whereas the F (p) DOS has two peaks at deeper layers, and with a growing number of layers, they

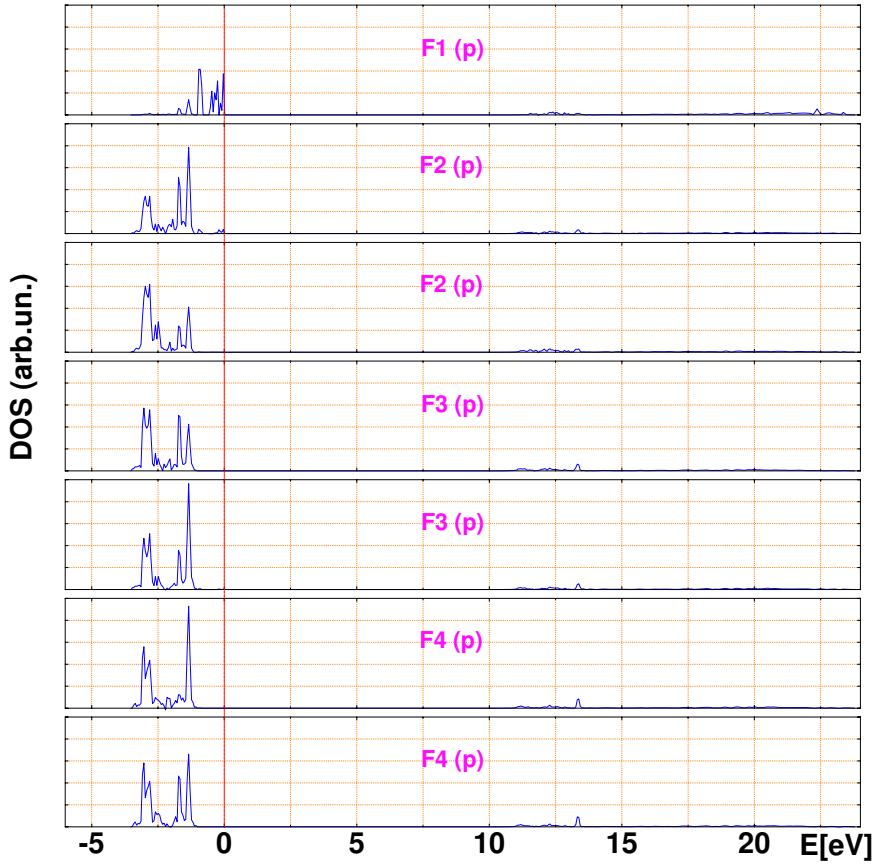

Figure 4.9: Projected density of states (DOS) for F p-orbitals in the (100) CaF_2 slab.

become more and more close to the relevant F (p) DOS for the CaF_2 bulk (see Figure 4.11).

4.3.3 Surface energies

Next, we discuss the surface energetics. The surface energy, i.e. an energy per unit area, was calculated as the difference between the total energy per unit cell of the slab and the normalized energy of the bulk:

$$E_{\text{surface}} = \frac{1}{2\sigma}[E_{\text{slab}}^{(relax)} - nE_{\text{bulk}}] \tag{4.1}$$

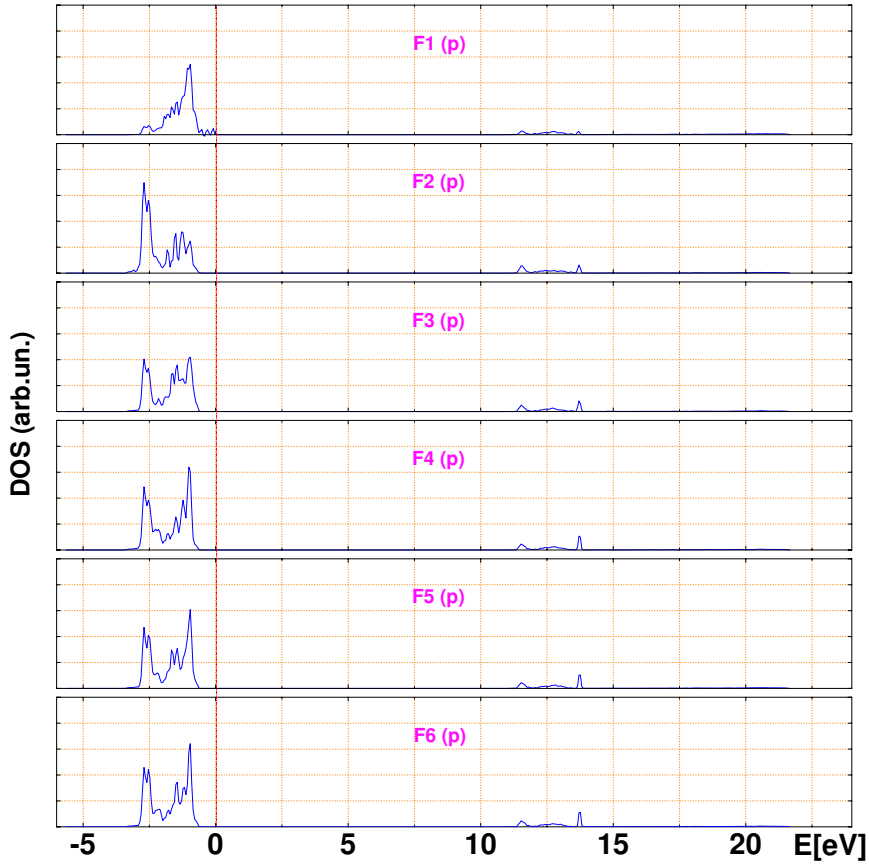

Figure 4.10: Projected density of states (DOS) for F p-orbitals in the (110) CaF_2 slab.

where n is the number of bulk primitive cells in the slab. σ is the surface area of the unit cell. E_{bulk} is the total energy per bulk unit cell, and $E_{\text{slab}}^{(relax)}$ is the total energy for a relaxed slab containing n layers. My calculated surface energies for the (111), (110) and (100) surfaces containing a different number of layers, using the hybrid B3PW functional, are collected in Table 4.9. As we can see from the results of my calculations, for CaF_2, the (111) surface energy is the lowest (0.437 J/m^2) for the slab containing seven layers, thereby indicating that the (111) surface is the most stable one among the (100), (110) and (111) surfaces, in agreement with experiment. For the CaF_2 (111) slab containing nine layers, according to my calculation, the surface energy is practically the same (0.438

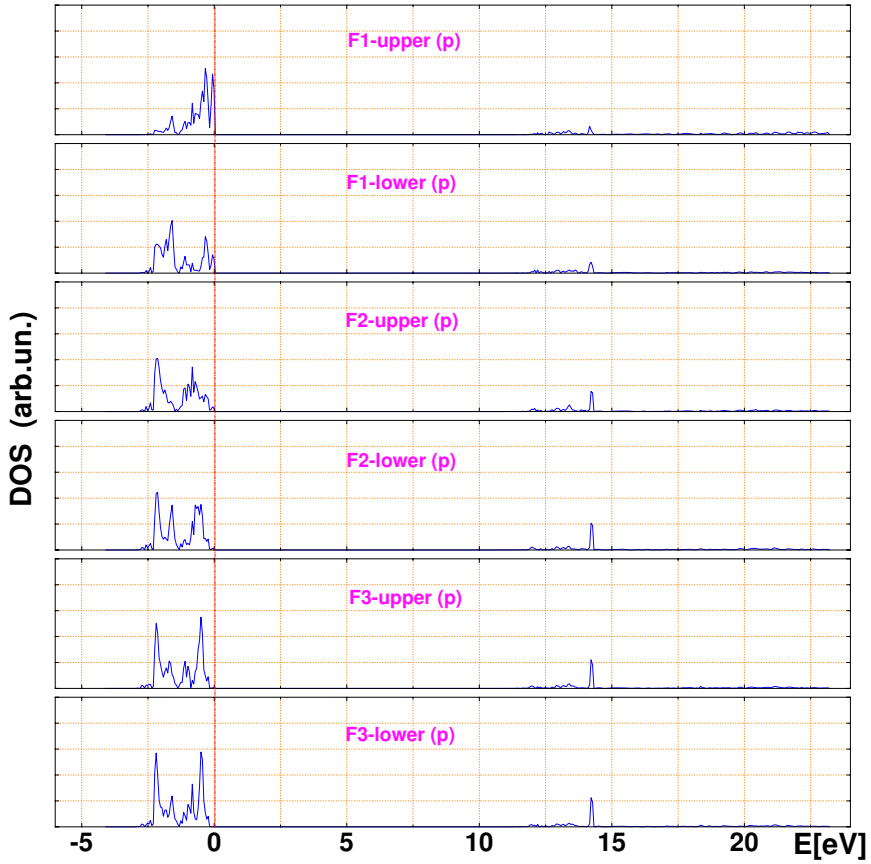

Figure 4.11: Projected density of states (DOS) for F p-orbitals in the (111) CaF_2 slab.

J/m^2) and has converged for the seven-layer slab. The calculated (111) surface energy is close to the (111) surface energy calculated earlier by Puchin *et al.* (2001), using the *ab inito* HF method, and is in good agreement with the only experimental estimation to my knowledge available (0.45 J/m^2) [Gilman (1960)]. My calculated surface energy for the CaF_2 (110) surface is considerably larger (0.719 J/m^2) than for the (111) surface. Finally, my calculations show that the CaF_2 (100) surface energy is the largest one (0.979 J/m^2) and also agrees qualitatively with the only previous *ab initio* (HF) calculation mentioned in Ref. [Puchin *et al.* (2001)] (1.189 J/m^2).

The calculated surface energy for the BaF_2 (111) is 0.334 J/m^2 and in agree-

Table 4.9: Surface energies (J/m^2) for the CaF_2 and BaF_2 (111), (110) and (100) surfaces calculated by means of the hybrid B3PW method. The experimental surface energy for the CaF_2 (111) surface is 0.45 J/m^2 [Gilman (1960)].

	Slabs	Number of layers	Surface energies
CaF_2	(111)	9	0.438
		7	0.437
	(110)	15	0.719
		9	0.717
	(100)	15	0.979
		9	0.957
BaF_2	(111)	15	0.334
		17	0.334
	(110)	15	0.494
		17	0.494
	(100)	15	0.666
		17	0.666

ment with the experiment value of 0.280 J/m^2 [Balik *et al.* (1982)]. The calculated surface energies for the (110) and (100) surfaces are 0.494 J/m^2 and 0.666 J/m^2, respectively. The (111) surface is also the energetically most favorable one. In comparison with my calculations for CaF_2, I predict that the BaF_2 (111) surface (0.334 J/m^2) is slightly more stable than the CaF_2 (111) surface (0.438 J/m^2).

Conclusions

Summing up, a comparison of *ab inito* HF and DFT calculations employing different exchange-correlation functionals clearly demonstrates that the best agreement with experiment for the lattice constant, bulk modulus, as well as the band structure is possible to achieve by the hybrid B3PW functional.

According to my calculations, the direct optical band gaps for CaF_2 and BaF_2

bulks are narrowed for the (111), (110) and (100) surfaces. This narrowing effect is mainly due to the F p orbitals at the surface layers. The (111) surface energy is the smallest one among these three terminations, indicating that the (111) surface is the most stable one, in good agreement with the available experimental result. The relaxation of F atoms in the upper sublayer of the top (111) surface layer is inwards and is comparable with the LEED experimental results.

Chapter 5

F centers in CaF_2 and BaF_2 bulks and the (111) slabs

Introduction

In this Chapter, I used the hybrid B3PW method to simulate F centers in CaF_2 and BaF_2. Firstly, I present theoretical investigations for the electronic structure, atomic geometry and formation energy of the F center in bulks. In the second part of this chapter, my calculation results for the simplest F-center aggregate, namely M center, were reported. Finally, as an extension of my study dealing with F centers in bulks, I performed calculations for surface F centers located at the (111) surface.

5.1 Method of calculations

To investigate F centers in CaF_2 and BaF_2, I used the first-principles DFT-B3PW method, according to my previous study dealing with CaF_2 and BaF_2 perfect crystals, which gave the best agreement with experiment for the lattice constant, bulk modulus and optical band gaps. The reciprocal space integration was performed by sampling the Brillouin zone of the unit cell with the $8 \times 8 \times 8$ Pack-Monkhorst net [Monkhorst & Pack (1976)].

To simulate F centers, I started with a 48-atom supercell with one of the

fluorine atoms removed. The 48-atom supercell is obtained by exploiting the transformation matrix that transforms the conventional f.c.c unit cell (3 atoms) into the primitive b.c.c cubic supercell (48 atoms). After the fluorine atom is removed, the atomic configuration of the surrounding atoms is re-optimized via a search of the total energy minimum as a function of the atomic displacements from the regular lattice sites. The basis sets for F, Ca and Ba atoms are the same as previous calculations. In order to have an accurate description of the F center, a basis set has been added at the fluorine vacancy, corresponding to the *ghost* atom. For the *ghost* atom, I used the same basis set as that used for the F^- ions of the bulk CaF_2 and BaF_2. For the M-center system, I used a 96-atom supercell with two of the neighbor fluorine atoms removed. The transformation matrices for the 48- and 96-atom supercells are expressed as:

$$\mathbf{T_{48}} = \begin{pmatrix} 3 & -1 & -1 \\ -1 & 3 & -1 \\ -1 & -1 & 3 \end{pmatrix} \qquad \mathbf{T_{96}} = \begin{pmatrix} -2 & 2 & 2 \\ 2 & -2 & 2 \\ 2 & 2 & -2 \end{pmatrix} \tag{5.1}$$

5.2 F centers in CaF_2 and BaF_2 bulks

Table 5.1: Formation energies, $E_{\text{formation}}$ (in eV), for an F center in CaF_2 and BaF_2 bulks for different supercells.

Number of atoms	CaF_2	BaF_2
12	7.88	7.82
24	7.87	7.82
48	7.87	7.82

F center, an electron trapped in an anion vacancy, is created on removal of the anion by irradiation or by additive colouration. As a starting point of my F-center calculations, I calculated the formation energy of the fluorine vacancy in CaF_2 and BaF_2 crystals. The formation energies of vacancies were calculated from the total energies of the supercells, based on the standard formalism by Mattila *et al.* (1997) and Zhang & Northrup (1991). For compound systems, formation energies of vacancies depend on the atomic chemical potentials. In addition, formation

energies of charged defects also vary with the electron chemical potential. For a vacancy with a charge state q, the formation energy is given by

$$E_{\text{formation}} = E_T(defect:q) - N_M\mu_M - N_F\mu_F + q(\varepsilon_F + E_{VBM}) \tag{5.2}$$

where $E_T(defect:q)$ is the total energy of the supercell containing a vacancy in a charge state q. Here N_M and N_F are the numbers of metal (M: Ca or Ba) and F atoms in the supercell, respectively. μ_M and μ_F are the atomic chemical potentials, and ε_F is the Fermi energy measured from the valence band maximum (VBM). In the supercell calculations for an isolated vacancy in alkaline-earth fluorides, Eq.5.2 can be rewritten using total energy of the perfect supercell $E_T(perfect)$ as follows:

$$E_{\text{formation}} = E_T(defect:q) - [E_T(perfect) - n_M\mu_M - n_F\mu_F] + q(\varepsilon_F + E_{VBM}) \tag{5.3}$$

Here n_M and n_F are the numbers of M and F atoms removed from the perfect supercell to introduce an isolated vacancy. We can modify Eq.5.3 for the formation energy of a neutral (the charge of total supercell is neutral) F center in fluorite as follows:

$$E_{\text{formation}} = E(\text{Fluorine}) + E(F) - E(\text{perfect}) \tag{5.4}$$

where E(Fluorine) is the energy for the isolated fluorine atom, $E(F)$ and E(perfect) are the energies of the defective crystal containing the F center and the perfect crystal, respectively. The fluorine vacancy formation energy, calculated using the hybrid B3PW method, going from the 12-atom supercell to the 48-atom supercell, as shown in Table 5.1, is reduced only by 0.01 eV and equals to 7.87 eV for the supercell containing 48 atoms in the CaF_2 case, and for BaF_2, the corresponding formation energies equal to 7.82 eV for the 12-, 24- and 48-atom supercells. It practically shows that the formation energy has converged.

The analysis of the effective charges shows that the electron associated with the removed F atom is well localized (-0.752 e) (see Table 5.2) inside the fluorine vacancy (V_F), -0.04 e is localized on the four nearest Ca atoms and -0.09 e on the six second-nearest neighbor fluorine atoms. The charge density map of the F center in CaF_2 (see Figure 5.1) also shows that in CaF_2 the F-center charge is well localized inside the V_F and the deformation of the neighbor ions from their

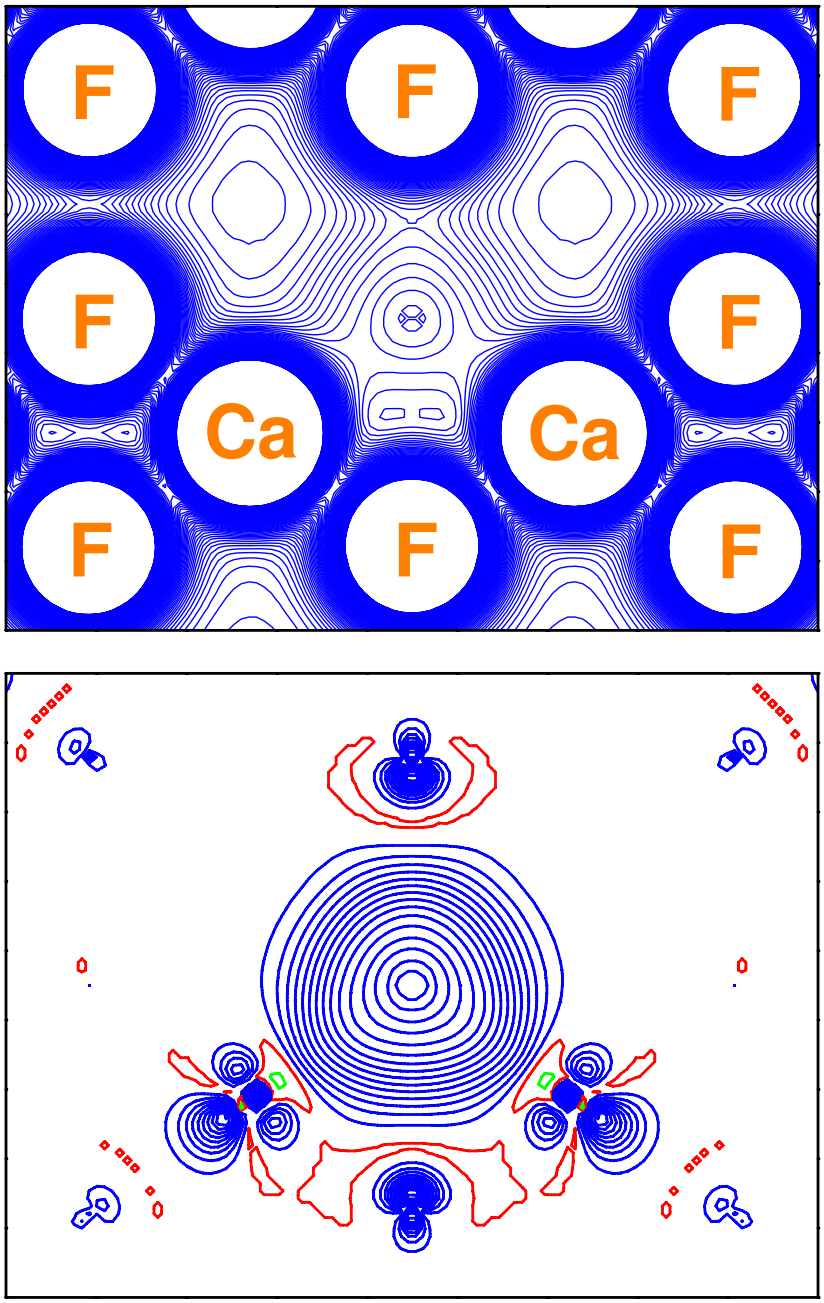

Figure 5.1: Electron charge (upper) and spin (lower) density maps of CaF_2 with an F center from the (110) side view. Isodensity curves are drawn from 0 e/bohr^3 to 0.1 e/bohr^3 with an increment of 0.001 e/bohr^3 for charge density and from -0.005 e/bohr^3 to 0.06 e/bohr^3 with an increment of 0.001 e/bohr^3 for spin density. Blue, green and red lines denote positive, negative and zero values, respectively.

Table 5.2: The effective charges (Q(e)) of the F center and surrounding atoms in CaF_2 and BaF_2 crystals for a supercell containing 48 atoms. ΔQ(e) is the charge difference between the defective and perfect crystals.

	Atom (ith-nearest)	Q (e)	Δ Q(e)	Spin ($n_\alpha - n_\beta$) (e)
CaF_2	XX	-0.752	+0.150	0.716
	Ca(1)	+1.793	-0.010	0.035
	F(2)	-0.917	-0.015	0.019
	F(3)	-0.902	0	0.001
	Ca(4)	+1.802	-0.001	0
BaF_2	XX	-0.801	+0.122	0.747
	Ba(1)	+1.828	-0.017	0.045
	F(2)	-0.929	-0.006	0.008
	F(3)	-0.923	0	0
	Ba(4)	+1.845	0	0

spherical shapes is negligible. My effective charge calculations for each basis set shell show that the inner part of the basis set, describing the 1s (0 e) and 2s (0.013 e and 0.018 e for CaF_2 and BaF_2, respectively) electrons of F^-, is obviously useless. Further analysis of the effective charges indicates that the unpaired electron inside the V_F is more diffuse than the valence electrons in the F^- valence shell and p-orbitals give just a minor contribution, as a consequence both of their different symmetry (s for the F center and p for the valence electrons of F^-) and of lack of nuclear attraction at the vacancy. Eventually, we can predict that the defect wave function can be described by a single, diffuse s Gaussian function very accurately. On the other hand, the localization of the unpaired electron at the V_F is clearly evident at the center of the spin map (Figure 5.1, lower) and the spin polarization of the nearest neighboring atoms is also appreciable. According to the results of my calculations, the experimentally measurable F-center spin density is equal to 0.716 e. Unfortunately, I did not find the experimental data for the F-center spin density in CaF_2 in literature. The calculated results of

effective charges for the BaF_2 F-center crystal are also reported in Table 5.2. The F-center charge for the BaF_2 bulk is -0.801 e and even more localized inside the V_F than in the CaF_2 case. This phenomena is in line with the fact that Ba has more metallic property than that of Ca.

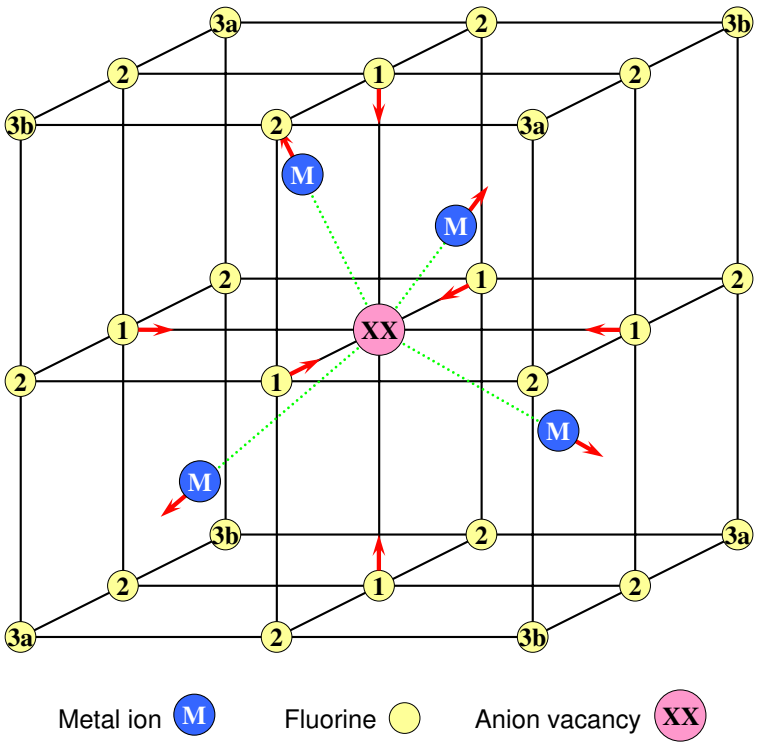

Figure 5.2: A view of the F-center nearest-neighbor geometry in MF_2, with the indication of relaxation shifts. The position of the F center is indicated by XX. The fluorine atoms in the first shell are labeled 1, in the second shell 2 and in the third shell 3a and 3b.

The fluorine vacancy site (F center) is surrounded in the ideal lattice by four metal (M) atoms forming a tetrahedron (see Figure 5.2). The next-nearest neighbor shell is formed by six fluorine atoms. The positions of 10 atoms surrounding the F center in alkaline-earth fluorides with point group symmetry T_d after lattice relaxation to the minimum of the total energy are calculated by means of the hybrid B3PW method. The atomic relaxations of 10 atoms surrounding the

Table 5.3: Atomic relaxations of 10 atoms surrounding an F center placed at the coordinate origin in the CaF_2 and BaF_2 48-atom supercells (in percent of the lattice constants, a_0=5.50 Å for CaF_2 , a_0=6.26 Å for BaF_2). Positive signs indicate the outward movements of the F center.

		CaF_2	BaF_2
Atom	Number of atoms	D (% a_0)	D (% a_0)
M	4	+0.15	+0.03
F1	6	-0.28	-0.23

F center in CaF_2 and BaF_2 bulks are reported in Table 5.3. The conclusion is that the repulsions of the four nearest M atoms from the F center by 0.15 % of a_o for CaF_2 and 0.03 % of a_o for BaF_2, and inward displacements of the second-nearest neighbor F atoms by 0.28 % of a_0 and 0.23 % of a_o for CaF_2 and BaF_2, respectively, are small, since the effective charge of the F center is close to the effective charge of the fluorine ions in the perfect crystals.

The defect-defect coupling is also seen in the CRYSTAL-B3PW calculations. For the CaF_2 case, the width of the *defect band* is 1.13 eV for the 12-atom supercell, 0.23 eV for the 24-atom supercell and 0.07 eV for the 48-atom supercell. In these supercells the distance between the periodically repeated F centers varies from 5.50 Å (12-atom supercell) to 9.53 Å (48-atom supercell). On the other hand, the width of the *defect band* is only 0.016 eV for the BaF_2 48-atom supercell. The defect-defect coupling due to the periodically repeated defects in our supercell model is practically negligible for the 48-atom supercell, since the width of the *defect band* is very small.

As mentioned in Chapter 2, alkaline-earth fluorides exhibit optical absorption, centered around 3.3 eV for CaF_2 [Arends (1964)] and 2.3 eV for BaF_2 [Nepomnyashchikh *et al.* (2002)]. My results for defect levels (see Figure 5.3 and 5.4) suggest a possible mechanism for this optical absorption. In the ground state, the defect band in the α graph is occupied and is unoccupied in the β figure (see Figure 5.3 and 5.4). The optical absorption corresponds to an electron transition from the F-center ground state to the conduction band (CB). Because of the spin difference between α and β states and the selection rules, the electron transition

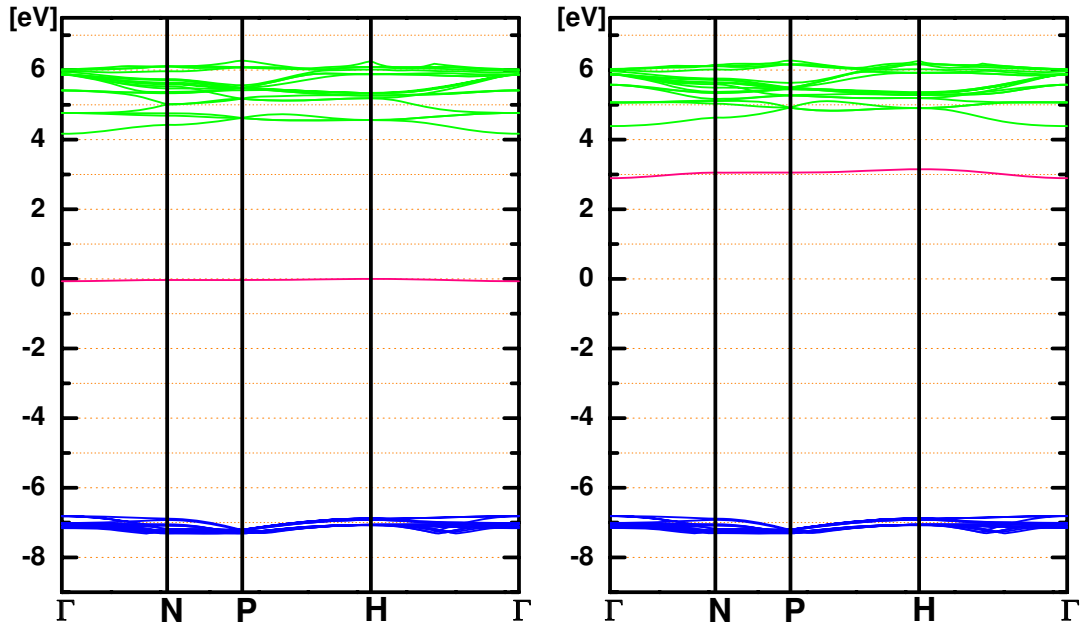

Figure 5.3: Calculated band structure for the 48-atom supercell modeling the F center in CaF_2. α (left) and β (right) denote the majority and minority spin states, respectively.

from the α occupied band to the β unoccupied band is impossible. The calculated optical band gaps for the F centers in CaF_2 and BaF_2 bulks are collected in Table 5.4. The experimentally observed optical absorption could be due to an electron transfer from the F-center ground state, located at Γ point 6.75 eV for CaF_2 and 7.01 eV for BaF_2 above the valence band (VB) top, to the conduction band bottom. The corresponding calculated values in CaF_2 and BaF_2 are 4.24 eV and 4.27 eV, respectively, which, however, still differ considerably from the experimental results. It is well known that only the highest occupied one-electron level has a strict physical meaning in exact DFT, which is merely a formalism for the electronic ground state [Jones & Gunnarsson (1989)]. This discrepancies may be caused by the reason, that I calculated the optical absorption energy as a difference between occupied and unoccupied one-electron energies, which in general is a very crude approximation, but could be justified in our case by the fact, that my calculated band gaps are reasonable and close to the experimental

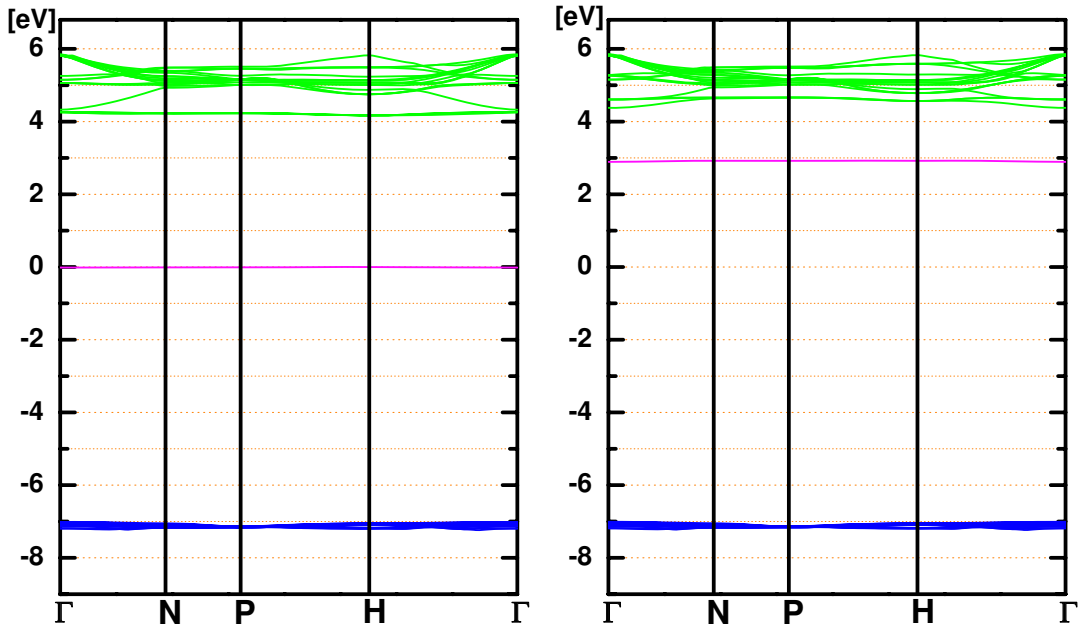

Figure 5.4: Calculated band structure for the 48-atom supercell modeling the F center in BaF_2. α (left) and β (right) denote the majority and minority spin states, respectively.

values.

The presence of an unpaired electron is also revealed by the band structure of the defective system, given in Figure 5.3 and 5.4. The bound unpaired electron level lies in the gap; the corresponding unoccupied level appears in the β spin structure, again in the gap but at positive energies. Unlike unpolarized band structure curves whose states can be occupied by two electrons, only one electron occupies one state in Figure 5.3, and 5.4.

At this point, I should address the question of the band-gap difference between α and β states. From Table 5.4, we can see that the band gaps between VB and CB in the α case for the F-center systems are very close to the gaps in perfect crystals (10.96 eV for CaF_2 and 11.30 eV for BaF_2), and the gaps in the β case are slightly larger than in the α case. The reason is that there is more exchange energy for the α case due to the more number of the α-spin electrons and the exchange contribution is negative. The detailed discussion about this problem

Table 5.4: Direct optical gaps (eV) ($\Gamma \rightarrow \Gamma$) of the F center in CaF_2 and BaF_2 bulks.

	CaF_2		BaF_2	
Optical Gaps	α	β	α	β
$V_F \rightarrow$ CB	4.24	—	4.27	—
VB $\rightarrow$ CB	10.99	11.20	11.28	11.39
VB $\rightarrow V_F$	—	9.71	—	9.91

can be seen in Appendix A.

To get more detailed electronic structure information of the defect bands, total and projected DOS for the F center in the CaF_2 bulk was calculated and shown in Figure 5.5. The analysis of DOS calculations shows that, the defect bands between the VB and CB mainly consist of V_F s-orbitals, and d-orbitals of the nearest Ca atoms, s- and p-orbitals of the second-nearest F atoms also do a few contributions to the defect bands. Further investigation of DOS calculations indicates that the outer s-orbitals of the V_F do more contributions. This is also supported by the Mulliken charge analysis, which gives charges very close to zero for the two inner shells of the basis set of the V_F.

Next, I researched the hyperfine structure of the F center in CaF_2 and BaF_2. A hyperfine structure of the electron paramagnetic resonance (EPR) spectra can be detected, due to the interaction between the unpaired spin and the spin of neighboring nuclei. This information gives better insight into the structure of the defect. The isotropic hyperfine interaction is caused by the non-zero probability of an electron being in the position of a given nucleus. This is only true for the s type orbitals (they are the only ones which do not become zero at the origin). The anisotropic contribution is due to the presence of higher order poles, and it is indicative of the deformation of the electronic density with respect to the spherical distribution [Saunders *et al.* (2003)].

The electron and nuclear spin coupling term $\mathcal{H}_S$ in the Hamiltonian is defined as:

$$\mathcal{H}_S = \widetilde{\mathbf{S}} \cdot \mathbf{A} \cdot \mathbf{N} \tag{5.5}$$

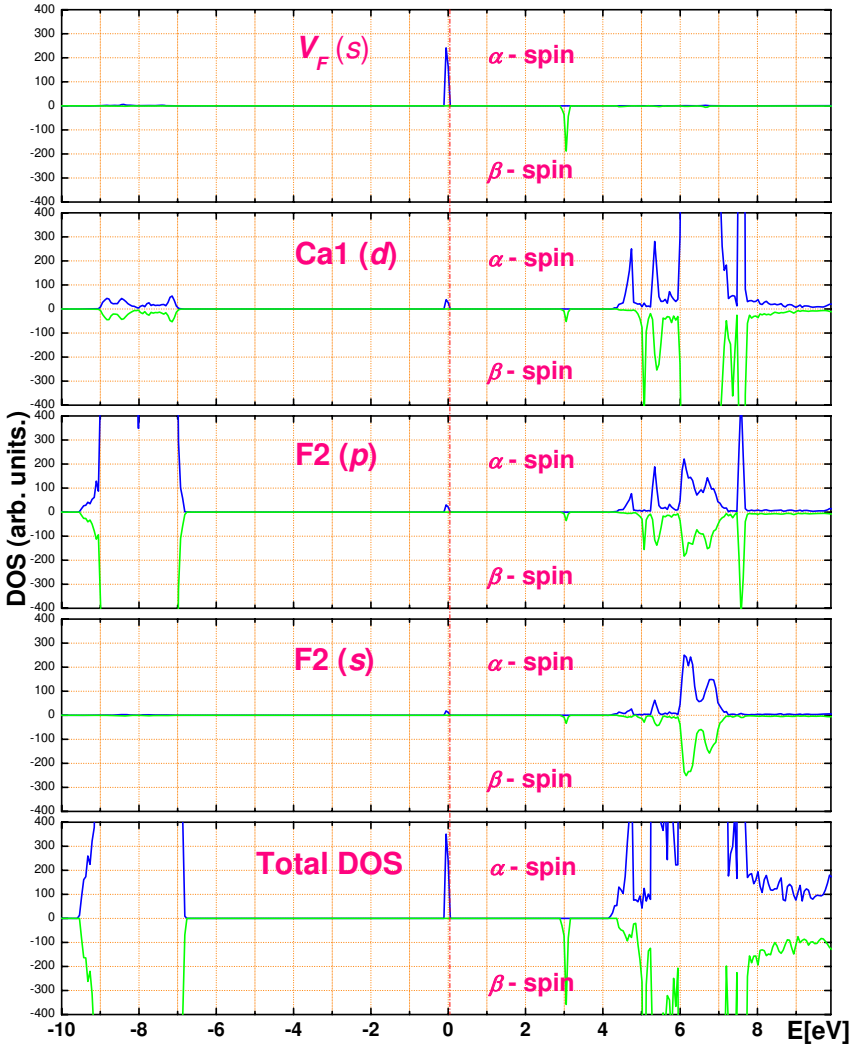

Figure 5.5: Total and projected density of states (DOS) for the F center in the CaF_2 bulk. α and β denote the up- and down-spin states, respectively.

where **S** and **N** denote the electron and the nuclear spin vector operators, respectively, $\widetilde{\mathbf{S}}$ is the transpose of **S** and **A** is known as the hyperfine parameter matrix. The symmetry properties of **A** allow its decomposition into two terms as follows:

$$\mathbf{A} = A_0\mathbf{I_3} + \mathbf{T} \tag{5.6}$$

T being a traceless tensor, $\mathbf{I}_3$ a 3×3 identity matrix and A_0 a scalar quantity. Thus, substituting Eq.5.6 into Eq.5.5, $\mathcal{H}_S$ can be written as the sum of an isotropic (iso) and an anisotropic or dipolar (dip) component:

$$\mathcal{H}_S = \mathcal{H}_{iso} + \mathcal{H}_{dip} \tag{5.7}$$

with

$$\mathcal{H}_{iso} = A_0\widetilde{\mathbf{S}} \cdot \mathbf{N} \tag{5.8}$$

and

$$\mathcal{H}_{dip} = \widetilde{\mathbf{S}} \cdot \mathbf{T} \cdot \mathbf{N} = -\frac{\mu_0}{4\pi} g\beta_e g_N \beta_n \left(\frac{\widetilde{\mathbf{S}} \cdot \mathbf{N}}{r^3} - \frac{3\widetilde{\mathbf{S}} \cdot \mathbf{r} \quad \mathbf{N} \cdot \mathbf{r}}{r^5} \right) \tag{5.9}$$

Usually, the experimental hyperfine coupling data are reported in terms of the isotropic a and anisotropic b hyperfine coupling constants. For each nucleus N, they (in MHz) are expressed as [Weil *et al.* (1994)]:

$$a = \frac{2\mu_0}{3h} g\beta_e g_N \beta_n \rho^{\alpha-\beta}(0) \tag{5.10}$$

$$b = \frac{\mu_0}{4\pi h} g\beta_e g_N \beta_n [T_{11} - \frac{1}{2}(T_{22} + T_{33})] \tag{5.11}$$

where the spin density $\rho^{\alpha-\beta}$ at N, the elements of the hyperfine coupling tensor **T**, and the electron g factor are the only terms that depend on the electronic structure of the system. All other multiplicative factors in Eq.5.9, 5.10 and 5.11 are tabulated constants [Lide (1991); Weil *et al.* (1994)] (h is the Planck constant, β_e and β_n the electronic and nuclear magnetons, μ_0 the permeability of the vacuum, and g_N the nuclear g factor). **T** is a tensor of rank 2, which is obtained as the field gradient of the spin density at N. Its generic element has the form:

$$T_{ij}^N = \sum_{\mu\nu} \sum_{\mathbf{G}} P_{\mu\nu\mathbf{G}}^{\text{spin}} \int \varphi_\mu(\mathbf{r}) \left(\frac{r^2\delta_{ij} - 3r_i r_j}{r^5} \right) \varphi_\nu(\mathbf{r} - \mathbf{G}) d\mathbf{r} \tag{5.12}$$

where the origin of the Cartesian reference system is at nucleus N, r_i denotes the i-th component of $\mathbf{r}$ and $\varphi_\nu(\mathbf{r}\text{-}\mathbf{G})$ is the ν-th atomic orbital centered in cell $\mathbf{G}$. $P^{\text{spin}}_{\mu\nu\mathbf{G}}$ is the direct space spin density matrix element connecting the μ-th atomic orbital in the zero cell (the reference cell) to the ν-th one in cell $\mathbf{G}$.

Table 5.5: Observed and calculated hyperfine constants a and b (MHz) for the F center in CaF_2.

Atom (*shell*) (a)	My results	Expt[a]	Theory[a]	Theory[b]
F(1)	147.11	182.51	245.5	279.16
F(2)	5.83	10.85	16.4	38.75
F(3a)	23.24	21.33	2.33	43.92
F(3b)	1.57	3.72	2.33	1.10
Atom (*shell*) (b)	My results	Expt[a]	Theory[a]	
F(1)	16.63	24.55	26.7	
F(2)	1.30	1.81	2.58	
F(3a)	3.41	3.00	0.87	
F(3b)	0.64	0.90	0.87	

[a]Reference Stoneham *et al.* (1968)
[b]Reference Bartram *et al.* (1971)

The calculated and experimental values of a for the coupling of the unpaired electron spin to nuclear spins are presented in Table 5.5 and 5.6. For F(1), our calculation underestimates the experimental value by nearly 19% for CaF_2 and 45% for BaF_2, but it is much better than other theoretical results [Bartram *et al.* (1971); Stoneham *et al.* (1968)]. The evaluation of F(3a) is in good agreement with the experiment, but F(2) and F(3b) are underestimated considerably. A comparison of my hybrid B3PW calculation for the anisotropic hyperfine constants b with other theoretical studies and experimental results [Stoneham *et al.* (1968)] is also presented in Table 5.5 and 5.6. The agreement for b constants is better than for a. From Table 5.5 and 5.6, we can find it is difficult to give good theoretical results of hyperfine constants for F-center systems, unlike lattice

Table 5.6: Observed and calculated hyperfine constants a and b (MHz) for the F center in BaF_2.

Atom (*shell*) (a)	My results	Expt[a]	Theory[a]	Theory[b]
F(1)	29.46	53.8	149.0	174.70
F(2)	0.66	5.1	7.7	23.09
F(3a)	46.38	42.6	0.89	28.52
F(3b)	0.09	2.2	0.89	1.20
Atom (*shell*) (b)	My results	Expt[a]	Theory[a]	
F(1)	6.59	7.0	15.5	
F(2)	0.51	1.1	1.45	
F(3a)	6.00	5.4	0.55	
F(3b)	0.36	0.5	0.55	

[a]Reference Stoneham *et al.* (1968)
[b]Reference Bartram *et al.* (1971)

constant, bulk modulus and band gaps for the perfect crystals. However, on the whole, my results for hyperfine coupling look reasonable. In Chapter 8, the hyperfine calculations dealing with hydrogen centers in alkaline-earth fluorides are in much better agreement with experimental data than in this F-center case. I suggest that the reason should be the choice of the basis sets of the point defects. Additionally, the results of hyperfine coupling calculations for CaF_2 look better than for BaF_2. I suggest that it is due to the ECP adoption for Ba basis set.

5.3 M centers in CaF_2 and BaF_2 bulks

F centers in additively-colored alkaline-earth fluoride crystals readily aggregate forming more complex centers [Hayes (1974)]. The simplest aggregate, the M center (see Figure 5.6), is composed of two F centers. I computed a 96-atom supercell with two of the neighbor fluorine atoms removed.

I calculated the redistribution of the electrons after the M-center formation.

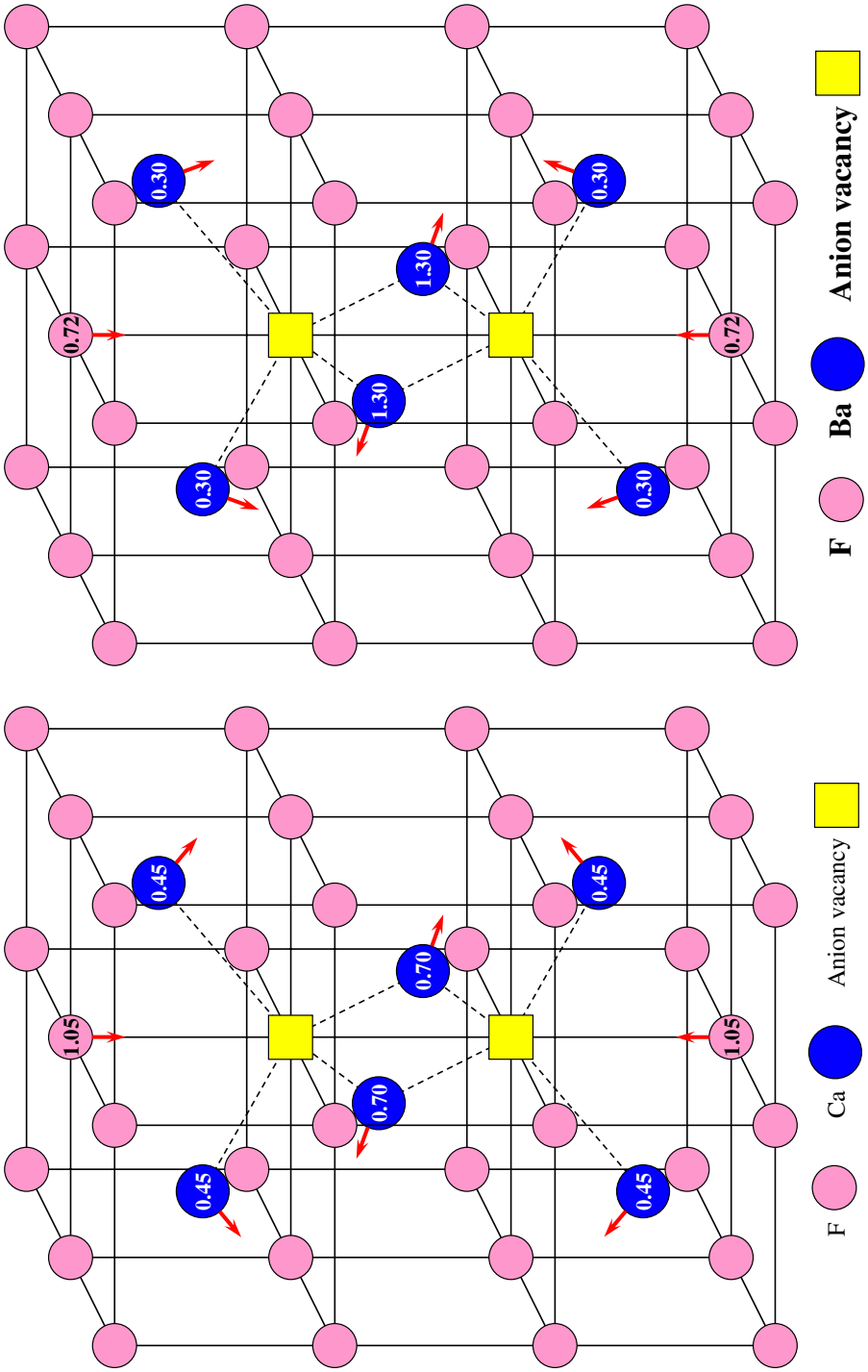

Figure 5.6: A view of the M-center nearest-neighbor geometry in CaF_2 and BaF_2 with indication of relaxation shifts. The positions of the anion vacancies are indicated by two squares. The directions of atomic displacements are shown with arrows, the values are given as % of the lattice constant in circles.

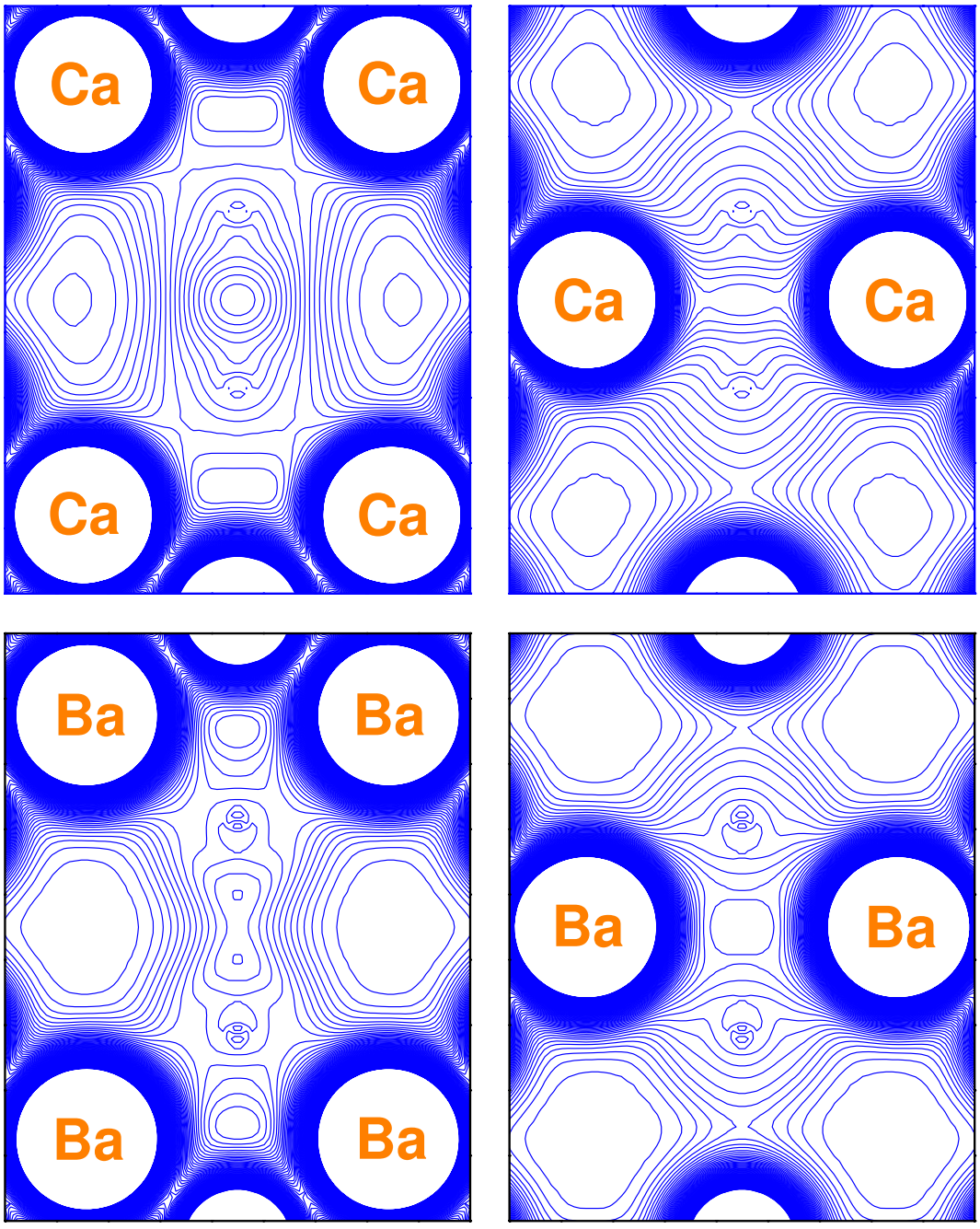

Figure 5.7: Charge density maps of CaF_2 and BaF_2 crystals with the periodic M center from the (1 1 0) (left) and (1 -1 0) (right) side views. Isodensity curves are drawn from 0 e/bohr^3 to 0.1 e/bohr^3 with an increment of 0.001 e/bohr^3.

For CaF_2, the effective charges of the anion vacancies in the M-center case are -0.759 e and decrease slightly by 0.007 e in comparison with the F-center case (-0.752 e) (see Table 5.2). The charge value and charge density map (see Figure 5.7) of the M center show that the charges are well localized inside the M center. Bond population analysis between vacancy-vacancy (+274 me) in the M-center system and F-F bond population (-22 me) in the perfect CaF_2 bulk shows that the major effect observed here is a considerable increase of the chemical bonding covalency. For BaF_2, the charge of one anion vacancy in the M center is -0.794 e and increase slightly by 0.007 e in comparison with the F-center case. Similar to CaF_2, bond population vacancy-vacancy (+142 me) in the M-center system shows a considerable covalency.

The displacement values of six metal atoms surrounding the M center after the lattice relaxation to the minimum of the total energy are given in Figure 5.6. According to my calculations, the relaxations of other atoms surrounding the M center are small and the displacements are all less than 1% of a_0. These slight relaxations of atoms near the M center in alkaline-earth fluorides can be explained by the fact that the M-center charge is close to the double of fluorine charge in the perfect bulk.

According to our previous research dealing with F centers, because of an unpaired electron in the single F center, the band structure of the F-center system is polarized and is separated into two spin band structures, namely α (up-spin) spin structure and β (down-spin) spin structure. The bound unpaired electron level lies in the gap; the corresponding electron-hole level appears in the β spin structure, again in the gap but at positive energies. Unlike unpolarized band structure curves whose one state can be occupied by two electrons, only one electron occupies one state in the polarized band structure. In the ground state, the defect band in the α spin structure is occupied and is unoccupied in the β spin band. The optical absorption corresponds to an electron transition from the F-center ground state to the conduction band. Because of the spin difference between α and β states and the selection rules, the electron transition from the α occupied band to the β unoccupied band is impossible. The β band absorption is predominantly due to the presence of M centers [Hayes (1974)]. In the M-center case, the two original unpaired electrons of two neighbor F centers form a pair,

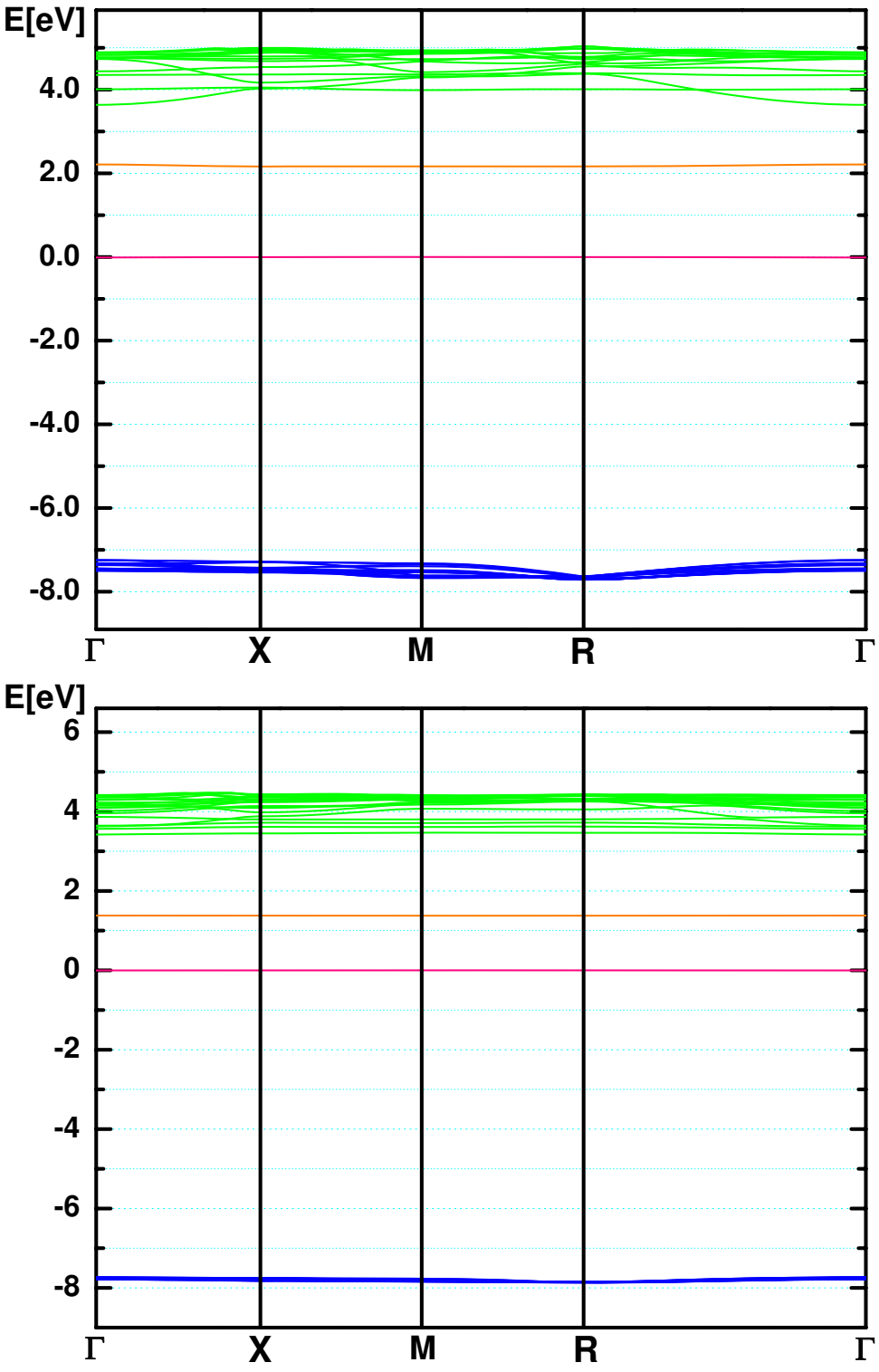

Figure 5.8: Calculated band structures for the 96-atom supercell modeling the M centers in CaF_2 (upper) and BaF_2 (lower).

so there is no unpaired electrons in the supercell. The α band can be occupied by two electrons due to unpolarized band structure, so the electron transition from α band to β band is possible. M centers contribute to absorption in the β band and this band will sometimes be referred to as the M band. My calculation of the direct optical gap ($\Gamma \rightarrow \Gamma$) for M centers in CaF_2 is 2.22 eV (see Figure 5.8) and is much smaller than the corresponding value in the F-center case (4.24 eV). A similar phenomenon, a decrease in the optical gap for M centers, was also observed for SrF_2 [Hayes (1974)] and BaF_2 (1.38 eV). Experimentally, the β band is located 2.38 eV above the α band for CaF_2 [Hayes (1974)]. It means that my calculated result is in good agreement with the experiment. Compared with the band structure of F centers, the α band in the M-center systems move upward (toward the gap) (Γ point) by 0.48 eV and 0.74 eV for CaF_2 and BaF_2, respectively. It is due to the extra Coulomb energy between the paired electrons of the M center. The detailed discussion can be seen in Appendix A.

5.4 Surface F centers in CaF_2 and BaF_2

As an extension of my study dealing with F centers in alkaline-earth fluoride bulks, I performed calculations for CaF_2 and BaF_2 surface F centers. The atomic and electronic structure of surface F centers, is practically unknown, and according to my knowledge has never been addressed in literature.

In the present work, I have studied the surface F centers on the (111) surface, which is the most stable one among the (111), (110) and (100) terminated surfaces according to my previous discussion about the pure slabs. I considered the surface F centers located in the upper sublayer of the first surface layer (see Figure 5.9). I performed my surface F-center investigations for a slab containing 4 layers. Each layer consists of 3 sublayers, containing 9 atoms. Thereby I performed the surface F-center calculations for supercells containing 108 atoms.

According to the results of my calculations, for CaF_2, the formation energy of the surface F center located at the surface was found to be 7.10 eV. The conclusion can be drawn that the defect formation in the CaF_2 (111) surface is by 0.77 eV smaller than in the bulk (7.87 eV). This is similar to what has been obtained for other materials and is due to the reduced coordination at the surface

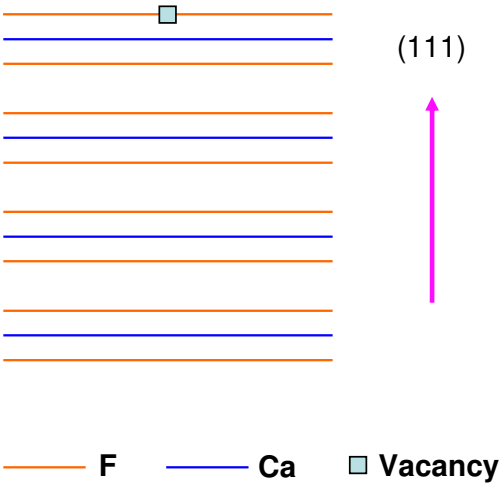

Figure 5.9: Schematic sketch of the (111) surface containing F centers.

[Carrasco *et al.* (2004)]. The formation energy of the F center at the surface for BaF_2 equals to 7.48 eV and is also smaller than in the bulk by 0.34 eV. The lower formation energy for the surface F center shows the preference of F centers locating near the surface.

The relaxation of the atoms nearest to the surface F center is calculated and depicted in Figure 5.10 and Table 5.7. The Ca atoms located at the middle sublayer of the first surface layer is repulsed from the surface F center by 0.66% of a_0. The displacement of Ca atoms exceeds by a factor of four than that in the bulk. The three fluorine atoms located at the lower sublayer of the first surface layer, due to the surface effect and an additional degree of freedom in the Z direction, are repulsed from the surface F center by 0.34% of a_0. The magnitude of this displacement is comparable with fluorine atoms attraction to the F center in the CaF_2 bulk, but the displacement direction is opposite. For BaF_2, unlike the slight repulsion in the bulk F-center case, the nearest three Ba atoms located at the second sublayer of the top surface layer approach the surface F center by 0.13% of a_0. The three neighbor F atoms located at the lower sublayer of the first surface layer are attracted to the surface F center by

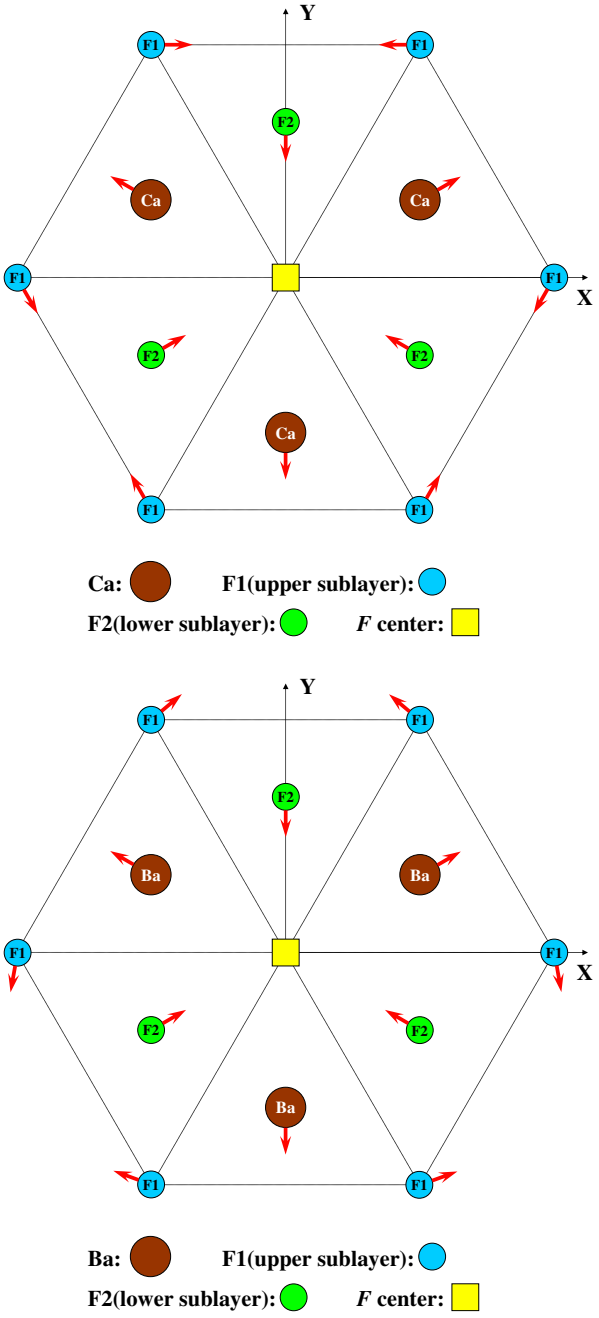

Figure 5.10: A top view of the surface F-center nearest-neighbor geometry with the indication of relaxation shifts. The directions of atomic displacements are shown with arrows.

Table 5.7: Atomic relaxations of CaF_2 and BaF_2 slabs containing an F center located at the (111) surface (as a percentage of the lattice constant). Positive signs correspond to outward atomic displacements (toward the vacuum). The directions of atomic displacements in the XY-plane are indicated in Figure 5.10. Atom labels are also defined in Figure 5.10. L indicates the distance between two neighbor atoms. Positive signs correspond to repulsions.

		CaF_2		BaF_2	
Atoms	Number	XY (% a_0)	Z (% a_0)	XY (% a_0)	Z (% a_0)
F1	6	0.15	-0.75	0.22	-0.35
M(Ca/Ba)	3	0.37	-0.92	0.02	+0.46
F2	3	0.20	-0.87	0.47	-0.02
		XX – Ca	XX – F2	XX – Ba	XX – F2
L (Å)		2.4181	2.7689	2.7025	3.1068
ΔL (% a_0)		+0.66	+0.34	-0.13	-0.37

0.37% of a_0. The magnitude of this displacement is larger than that in the bulk F-center case (0.23%) by around 60%.

With respect to the electronic structure of the surface F center in alkaline-earth fluorides, the effective charge analysis shows, that the electronic density around it is slightly more delocalized than that corresponding to the bulk F center. Table 5.8 shows the effective charge values of the F center and the nearest atoms. The effective charge localized inside the surface F center in CaF_2 is -0.744 e, by 0.008 e less than for the bulk F center (-0.752 e) in CaF_2 (see Table 5.2). According to my calculations, the decrease of the surface F-center charge is mainly due to outer p-orbitals and the charge movement from $3s$ to $4s$-orbitals leads the surface F center to be more diffuse. The charges of the nearest Ca atoms of the surface F center (+1.775 e) are reduced by 0.018 e in comparison with the charges of the respective Ca atoms (+1.793 e) near the bulk F center. Bond populations between the surface F center and the nearest Ca atoms are calculated. The major effect observed here is a strengthening of the surface F center and Ca chemical bond. The surface F center – Ca bond population is 36

Table 5.8: The effective charges (Q(e)) of the surface F center and surrounding atoms for the supercell containing 4 layers (108 atoms). ΔQ(e) is the charge difference between the defective slab and the perfect CaF_2/BaF_2 bulk. (For the CaF_2 bulk, Ca: +1.803 e, F: -0.902 e. For the BaF_2 bulk, Ba: +1.845 e, F: -0.923 e.)

		CaF_2		BaF_2	
Atoms	Number	Q (e)	ΔQ (e)	Q (e)	ΔQ (e)
XX	1	-0.744	+0.158	-0.790	+0.133
F1	6	-0.893	+0.009	-0.920	+0.003
M(Ca/Ba)	3	+1.775	-0.028	+1.813	-0.032
F2	3	-0.923	-0.021	-0.930	-0.007

me, which is larger than the relevant value (10 me) in the bulk by 26 me. The effective charge values of the surface F center and surrounding atoms for BaF_2 also can be found in Table 5.8. A similar effect to CaF_2, a strengthening of the F center – Ba bond population was also found. In the BaF_2 case, the corresponding bond population equals to 28 me and is larger than the relevant value (18 me) in the BaF_2 bulk by 10 me.

The α energy band corresponding to the surface F center at Γ point is located 7.00 eV (by 0.25 eV higher than in the bulk F-center case) for CaF_2 and 6.83 eV (by 0.18 eV lower than in the bulk F-center case) for BaF_2 above the VB top and is separated from the CB bottom by 3.81 eV and 3.98 eV for CaF_2 and BaF_2, respectively (see Figure 5.11 and 5.12). Because of the surface effect, these gaps are smaller than the corresponding values in the bulk F-center cases (4.24 eV for CaF_2 and 4.27 eV for BaF_2). On the other hand, the β band lies 10.16 eV for CaF_2 and 9.83 eV for BaF_2 above the VB top. Negligible dispersion effect of the defect band for 108-atom supercell means that the defect-defect interaction is practically eliminated, thus approaching the desired isolated single F center limit.

Here, we should note the question of the defect-band shift with respective to the VB top. As discussion above, the charge movement from 3s to 4s-orbitals

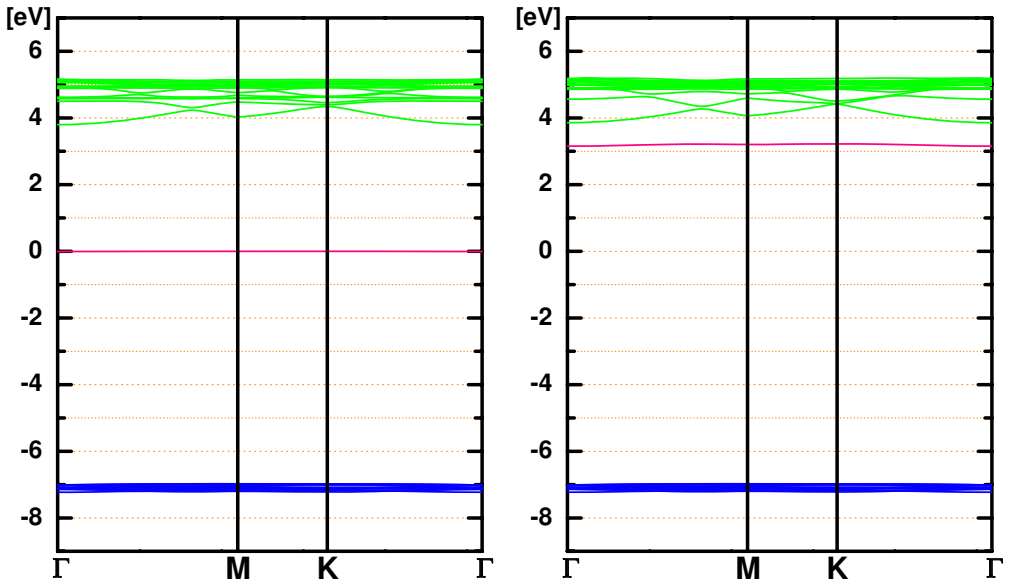

Figure 5.11: Calculated band structure for the 108-atom supercell modelling the surface F center in CaF_2.

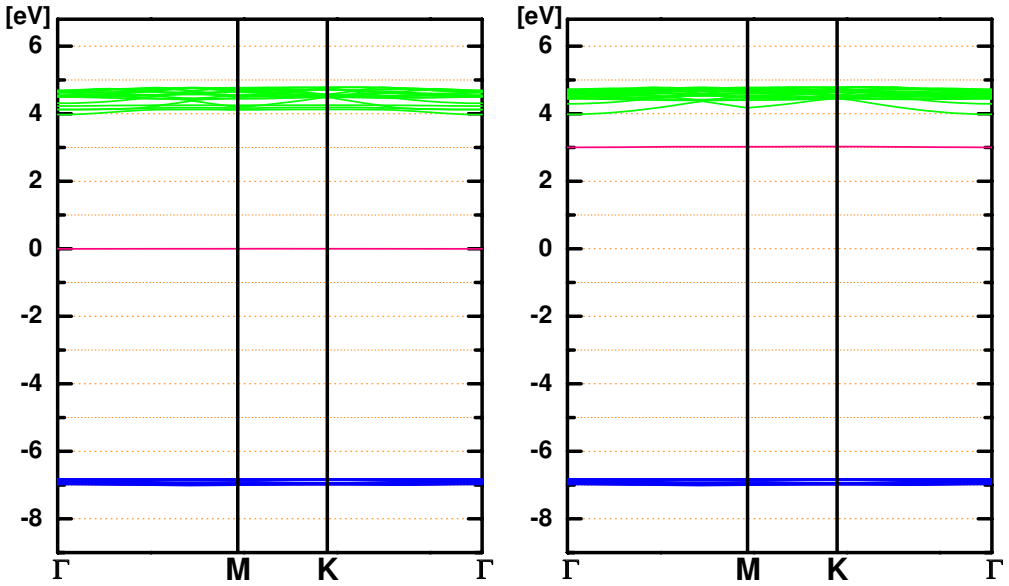

Figure 5.12: Calculated band structure for the 108-atom supercell modelling the surface F center in BaF_2.

indicating more diffused surface F center, which should lead the defect band move away (toward the gap) from the VB top. However, for the BaF_2 case, the distance between the defect band and the VB top narrows. We can explain this narrowing by the fact that the DOS of p-orbitals of the surface fluorine atoms move toward the gap more remarkably due to the surface effect, as mentioned in the discussion dealing with perfect slabs in Chapter 4.

Conclusions

The characterization of native point defects in alkaline-earth fluorides has important technological implications. In this Chapter, I applied the first-principles approach to the calculations of F centers in CaF_2 and BaF_2. I found, that the vacancy formation energies in CaF_2 and BaF_2 are 7.87 eV and 7.48 eV, respectively. The charge density map of the F center and effective charge calculation show, that the charge is well localized inside the V_F. My theoretical hyperfine coupling constants are in qualitative agreement with the experimental results. The relaxation of atoms surrounding the F center, according to my calculations, is small. The creation of a neutral V_F in CaF_2 and BaF_2 results in a new F-center defect band located at the Γ point 6.75 eV and 7.01 eV, respectively, above the VB top. I suggest that the optical absorption energy, experimentally observed in the CaF_2 crystal at around 3.3 eV and in the BaF_2 crystal at around 2.3 eV, can be due to an electron transfer from the F-center ground state to the CB.

The β band absorption in alkaline-earth fluorides is predominantly due to the presence of M centers. According to my calculations, the direct optical gap ($\Gamma \rightarrow \Gamma$) for M centers in CaF_2 is 2.22 eV, which is in good agreement with the experimental value of 2.38 eV, and much smaller than the corresponding value in the F-center case. The relevant optical gap in the BaF_2 M-center case is 1.38 eV and is also much smaller than in the F-center case.

The formation energies for the (111) surface F center in CaF_2 (7.10 eV) and BaF_2 (7.48 eV) are by 0.77 eV and 0.34 eV, respectively, smaller than in the bulks. The lower formation energy for a surface F center implicates the preference for F centers located near the surface.

5. F CENTERS IN CaF_2 AND BaF_2 BULKS AND THE (111) SLABS

Chapter 6

Oxygen-Vacancy dipoles in CaF_2

Introduction

In this Chapter, performing first principles calculations, I intend, firstly, to clarify the electronic structure, atomic geometry and band structure of Oxygen-Vacancy (OV) dipoles and, secondly, to study the aggregation of the OV dipoles in CaF_2 bulk. Finally, as an extension of my study dealing with OV dipoles in the bulk, I performed *ab inito* calculations of surface OV centers in CaF_2.

6.1 Method of calculations

I performed calculations for OV centers in CaF_2 using the hybrid B3PW method, which gives the best agreement with experiment for the lattice constant, bulk modulus and optical band gap (see Chapter 4).

In this Chapter, I used the same basis sets for the Ca and F atoms as in my previous study dealing with the CaF_2 electronic structure and F centers therein. For the O atom I used the basis set given in the Basis Sets Library [Saunders *et al.* (2003)]. The The reciprocal space integration was performed by sampling the Brillouin zone of the unit cell with the $6 \times 6 \times 6$ Pack-Monkhorst net [Monkhorst & Pack (1976)].

In order to calculate the OV center, I removed one fluorine atom from a 96-atom supercell and replaced a second fluorine atom with an oxygen atom.

After the fluorine atom is removed or replaced with an oxygen atom, the atomic configuration of the surrounding atoms is re-optimized via a search of the total energy minimum as a function of the atomic displacements from the regular lattice sites. In order to have an accurate description of the anion vacancy, a basis set has been added at the fluorine vacancy, corresponding to the *ghost* atom. For the *ghost* atom, like the F-center case, I used the same basis set as that used for F atoms.

As an approximation only, the optical absorption energies I calculated as a difference between occupied and unoccupied one-electron energies. In my calculations, I used periodic boundary conditions. Since I used a very large supercell containing 96 atoms, the interaction between periodically translated defects was negligible.

6.2 OV dipoles in the CaF_2 bulk

6.2.1 Single OV dipole in the CaF_2 bulk

One of the big unsolved problems in the context of the application of CaF_2 as an optical material is oxygen contamination in the bulk and at the surface. Oxygen is readily incorporated into the bulk during crystal growth and it is very difficult to avoid this contamination or to remove contaminants after growth [Mysovsky *et al.* (2004)]. Investigations by Adler & Kveta (1957) and by Bontinck (1958b) show that CaF_2 reacts readily with water vapor at high temperatures and suggest that the resulting hydrolysis gives rise to a variety of defects which includes O^{2-} ions in fluorine sites and charge-compensating fluorine vacancies (see also Messier (1968)).

A first step in the understanding of the OV centers in CaF_2, I performed the geometry relaxation of the atoms surrounding the OV dipole oriented along the (100) axis in CaF_2 (see Figure 6.1). Firstly, the oxygen impurity atom is strongly displaced by 3.02% of the lattice constant (a_0) towards the vacancy. The four nearest fluorine atoms located in the plane containing oxygen are displaced from the oxygen by 1.69% of a_0. The nearest neighbor fluorine atom located above the oxygen is even stronger displaced by 1.92% of a_0 from the oxygen. The four

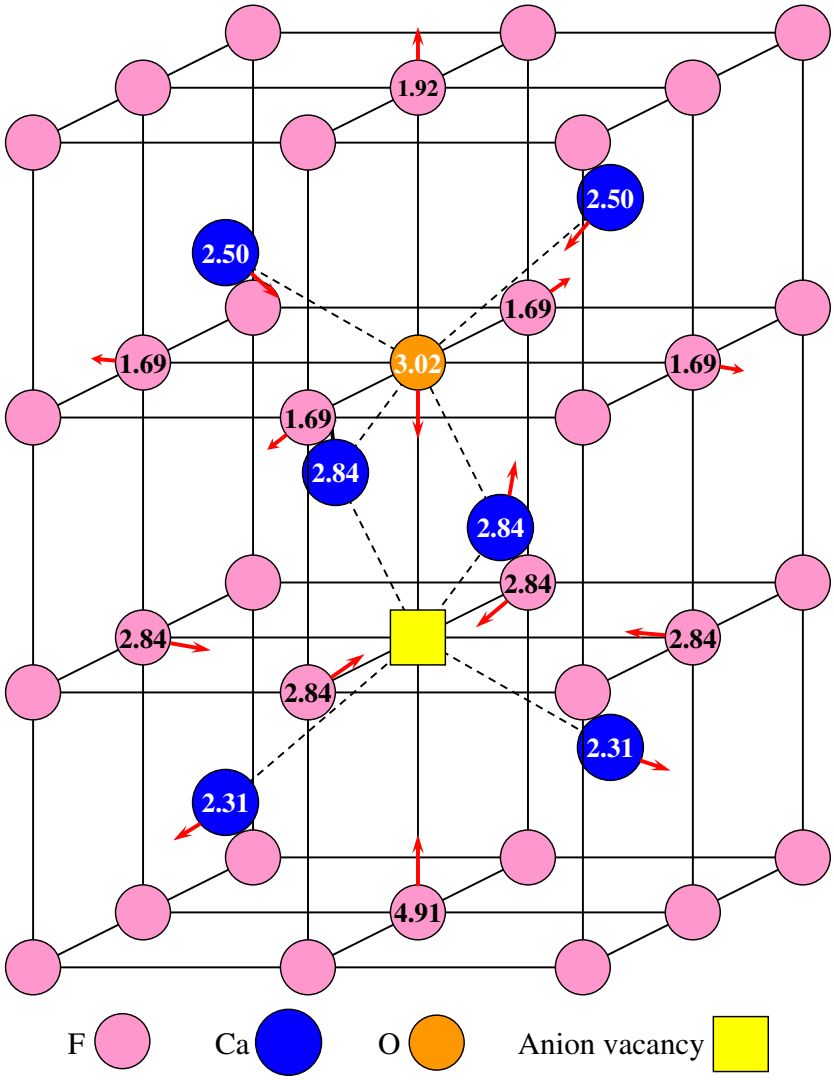

Figure 6.1: OV center in CaF_2 oriented along the (100) axis. The arrows show the directions of the atomic displacements surrounding the OV center, the displacement values are given in circles in % of the lattice constant $a_0 = 5.50$ Å.

nearest Ca atoms are strongly attracted by the oxygen impurity atom. So the two Ca atoms located at the plane above the oxygen atom move towards the oxygen impurity by 2.50% of a_0. The two Ca atoms located at the plane below the oxygen atom are even more strongly shifted by 2.84% of a_0 towards the oxygen impurity. According to my calculation, I found that the relaxation of the four Ca atoms surrounding the fluorine vacancy is much stronger than for the F-center case in CaF_2.

I also calculated the OV dipole oriented along the (110) direction. I found, that the total energy for the (110) case is by 0.32 eV larger than for the (100) case, i.e., the OV orientation along the (100) direction is energetically more favorable, with respect to the (110) case. Also according to the calculation of Mysovsky *et al.* (2004), the OV dipole (100) orientation is by 0.45 eV more stable as the (110) OV direction. Therefore, I focus my current research on the investigation of the (100) case.

The charge density map for the OV center in the CaF_2 bulk is shown in Figure 6.2. The analysis of the effective charges of the OV center and surrounding atoms shows that, unlike the well localized F center in CaF_2, only -0.082 e is localized inside the fluorine vacancy (see also Figure 6.2). Further investigation to the vacancy charge shows that almost all the charges occupy the outer-shell orbitals of the vacancy basis set. As mentioned before, the stronger relaxation of the four Ca atoms surrounding the fluorine vacancy also can be explained by the delocalized nature of the electron centered at the anion vacancy. The effective charge values of the OV center and surrounding atoms are shown in Figure 6.3. The effective charge of the impurity oxygen atom, which replaces a fluorine at the regular crystal site is -1.598 e and far from the ideal ionic value of -2 e. The effective charges (+1.809 e) of the two Ca atoms located above the oxygen impurity atom are by 0.006 e lager than in the perfect CaF_2 bulk (+1.803 e). For the Ca atoms located between the oxygen impurity and the fluorine vacancy, and below the fluorine vacancy, their effective charges are +1.775 e and +1.769 e, respectively. Both values are smaller than in the perfect CaF_2 bulk. The effective charge (-0.908 e) of the apical fluorine atom located above the oxygen impurity is by 0.006 e less than in the CaF_2 bulk (-0.902 e). The effective charges of the four fluorine atoms located at the same plane as oxygen ion are -0.901 e. The effective

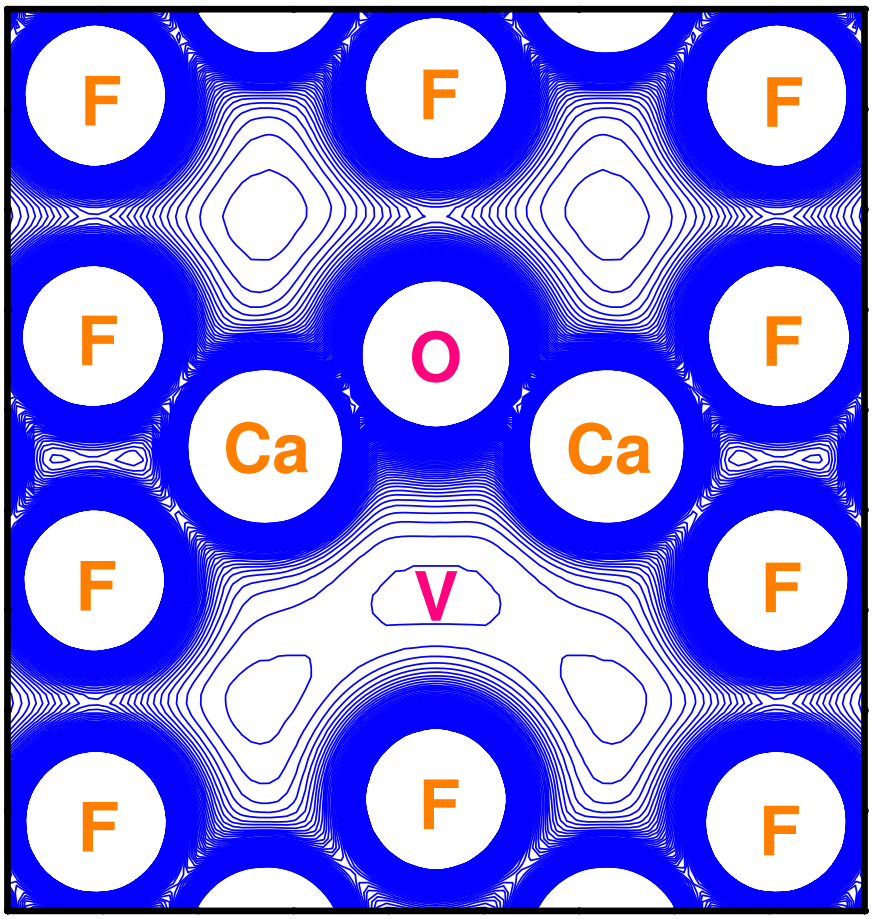

Figure 6.2: Charge density map of a CaF_2 crystal with the periodic OV center from the (1 1 0) side view. Isodensity curves are drawn from 0 e/bohr^3 to 0.1 e/bohr^3 with an increment of 0.001 e/bohr^3.

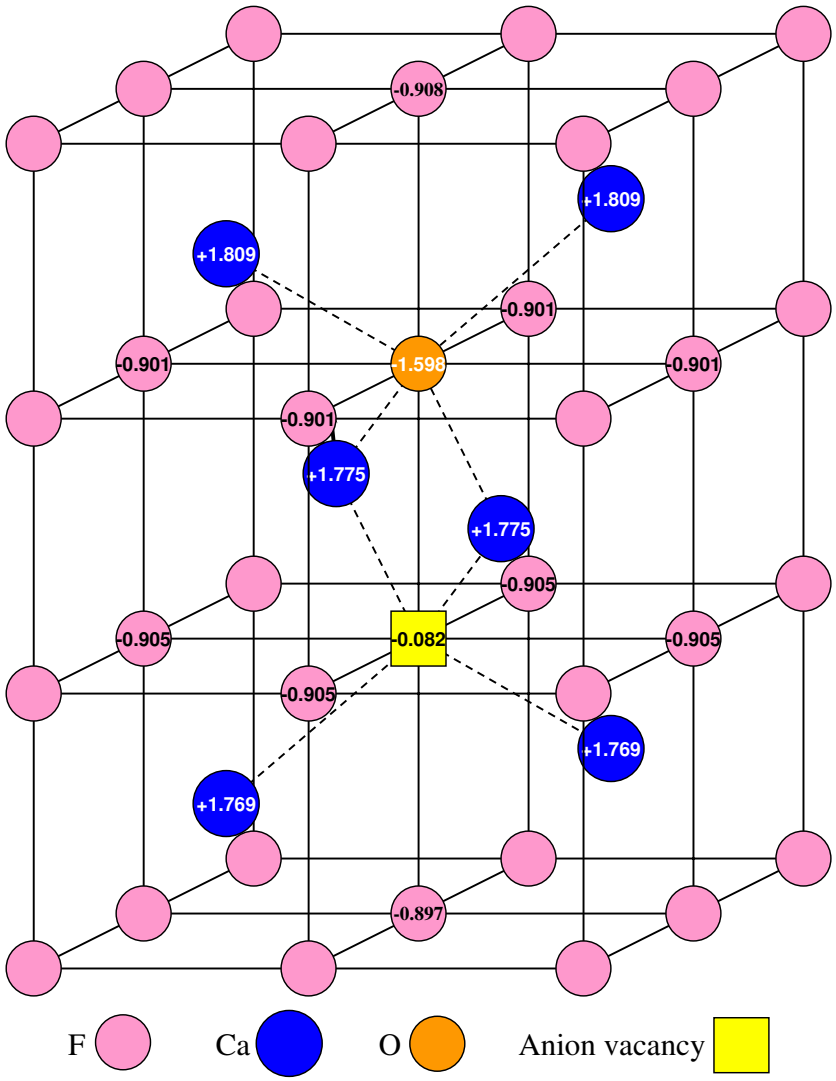

Figure 6.3: A view of the *OV* center geometry with the indication of effective charges.

charges of the four fluorine atoms located at the same plane as fluorine vacancy are -0.905 e. Finally the effective charge of the fluorine atom located below the fluorine vacancy is -0.897 e and increases by 0.005 e in comparison with the CaF_2 bulk. The total charge of the OV center, estimated as a sum of the O and V charges, equals to -1.680 e, smaller than double of the F charge in the perfect CaF_2 bulk. Thereby, part of the charges of the OV dipole diffuses to the surrounding atoms. Bond population analysis shows that the bond population between the oxygen impurity atom and the fluorine vacancy (+62 me) is strongly increased with respect to the bond population between two neighbor fluorine atoms (-22 me) in the perfect CaF_2 crystal.

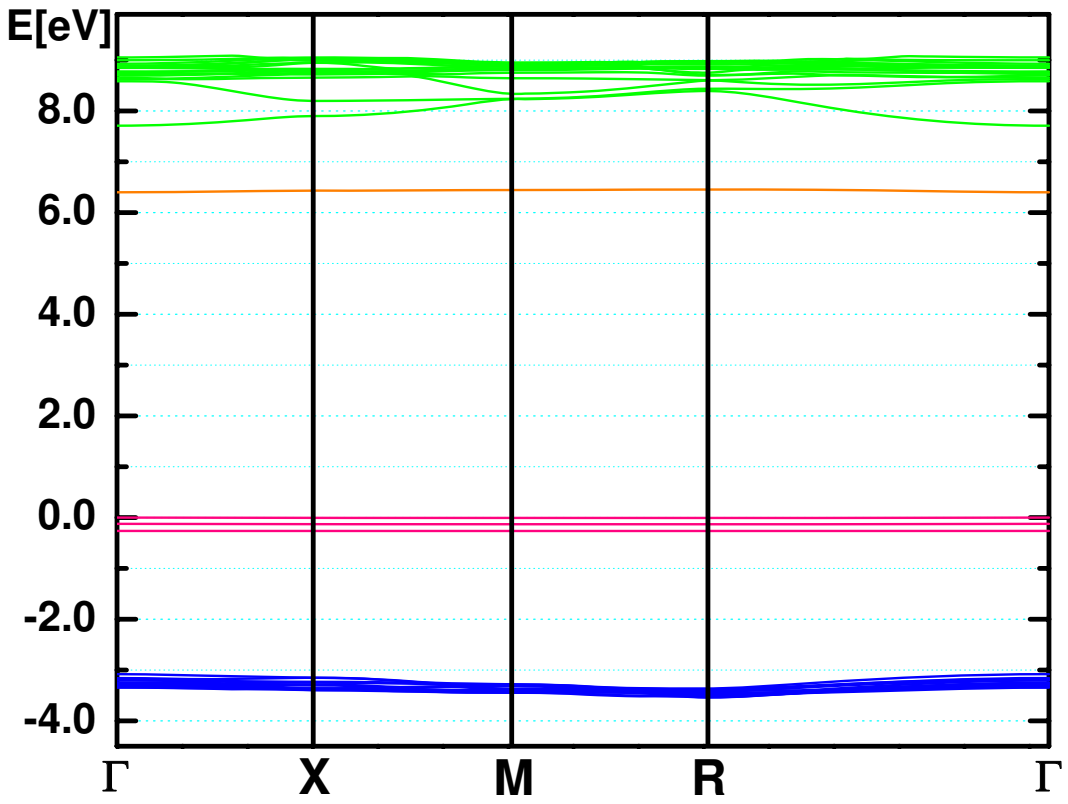

Figure 6.4: Calculated band structure for the 96-atom supercell modeling the OV center in the CaF_2 bulk.

As a next step, I calculated the band structure of the OV center oriented along

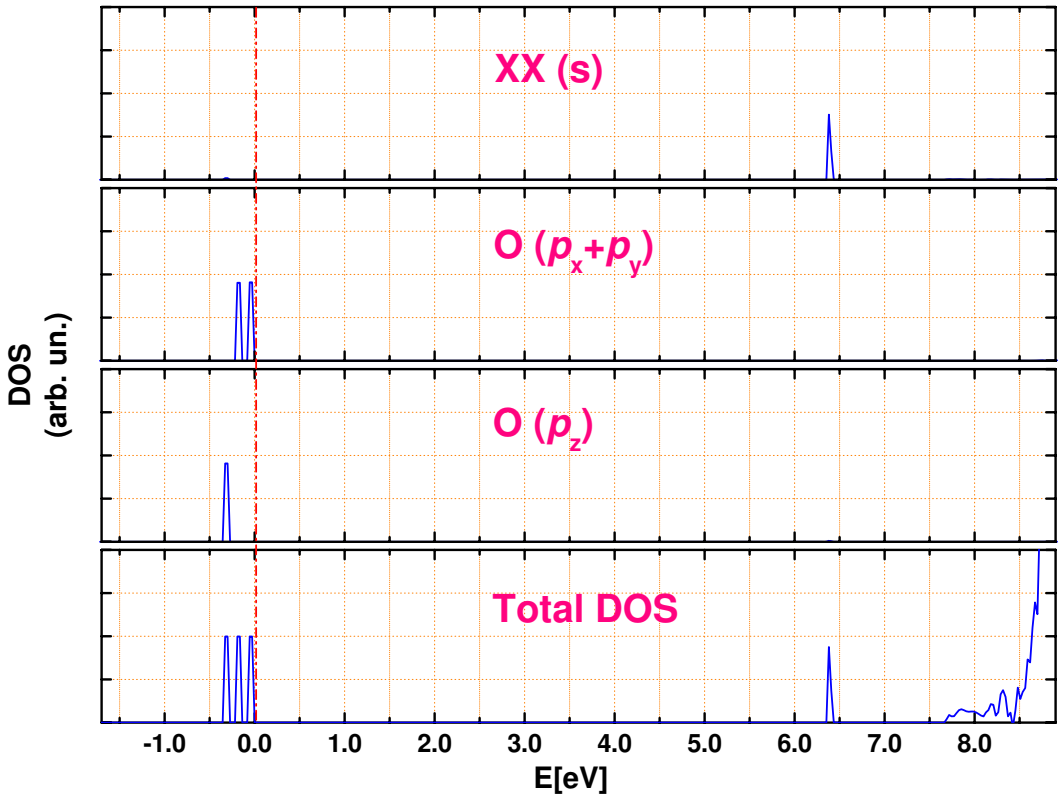

Figure 6.5: Density of states (DOS) of the OV center in the CaF_2 bulk.

the (100) axis in CaF_2. The optical band gap between conduction bands (CB) and valence bands (VB) for the CaF_2 96-atom supercell containing an oxygen impurity atom and a fluorine-site vacancy at the Γ point is 10.79 eV (see Table 6.1), which is slightly reduced with respect to the optical band gap of the perfect CaF_2 crystal (10.96 eV). According to my detailed effective charge and density of states (DOS) calculations, this reduction is mainly due to the p_z-orbitals of the F atom located below the vacancy. The empty defect level induced by the fluorine vacancy, and consisting mainly of s-orbitals of the vacancy is located 1.31 eV below the bottom of CB at the Γ point (see Figure 6.4). The three occupied defect levels, induced by the oxygen impurity atom are located 3.08 eV, 2.96 eV and 2.82 eV, respectively, above the VB top at the Γ point. The DOS of the OV center in CaF_2 is depicted in Figure 6.5. According to the

Table 6.1: Direct optical gaps ($\Gamma \rightarrow \Gamma$) of the *OV* center in the CaF_2 bulk. V indicates the vacancy band; O_1, O_2 and O_3 are three oxygen bands.

Optical gaps	$\Gamma \rightarrow \Gamma$ (eV)
$O_1 \rightarrow V$	6.40
$O_2 \rightarrow V$	6.52
$O_3 \rightarrow V$	6.66
VB $\rightarrow$ V	9.48
$O_1 \rightarrow$ CB	7.71
VB $\rightarrow$ CB	10.79

calculated DOS, oxygen *p*-orbitals are split into three bands near the Fermi-Energy due to the broken symmetry of the *OV* center. These three oxygen defect bands near the Fermi energy are separated by 0.26 eV, which is in the same energy range as the experimental separation interval of 0.48 eV [Mysovsky *et al.* (2004)]. My calculated optical absorption bands above the fluorine vacancy level at the Γ point are 6.40 eV, 6.52 eV and 6.66 eV, respectively, and very close to the complex experimental 6.7 eV absorption bands consisting of at least two elementary peaks with separation of 0.48 eV [Archangelskaya *et al.* (1980); Radzhabov & Figura (1986)]. The calculation of optical absorption bands simply as a difference between occupied and unoccupied one-electron energies, which is a very crude approximation, can be justified here, since my calculated optical band gap is in good agreement with the experiment. The separations of oxygen and vacancy levels induced by the defects in the gap, calculated by Mysovsky *et al.* (2004) (5.22 eV, 5.38 eV and 5.61 eV) are in qualitative agreement, but smaller than mine.

6.2.2 Aggregation of *OV* dipoles

Next, I calculated the aggregation of *OV* dipoles. I considered in my calculations a system which contains two oxygen impurity atoms and two vacancies (see Figure 6.6). Configuration 1, 2 and 3 are formed from the configuration

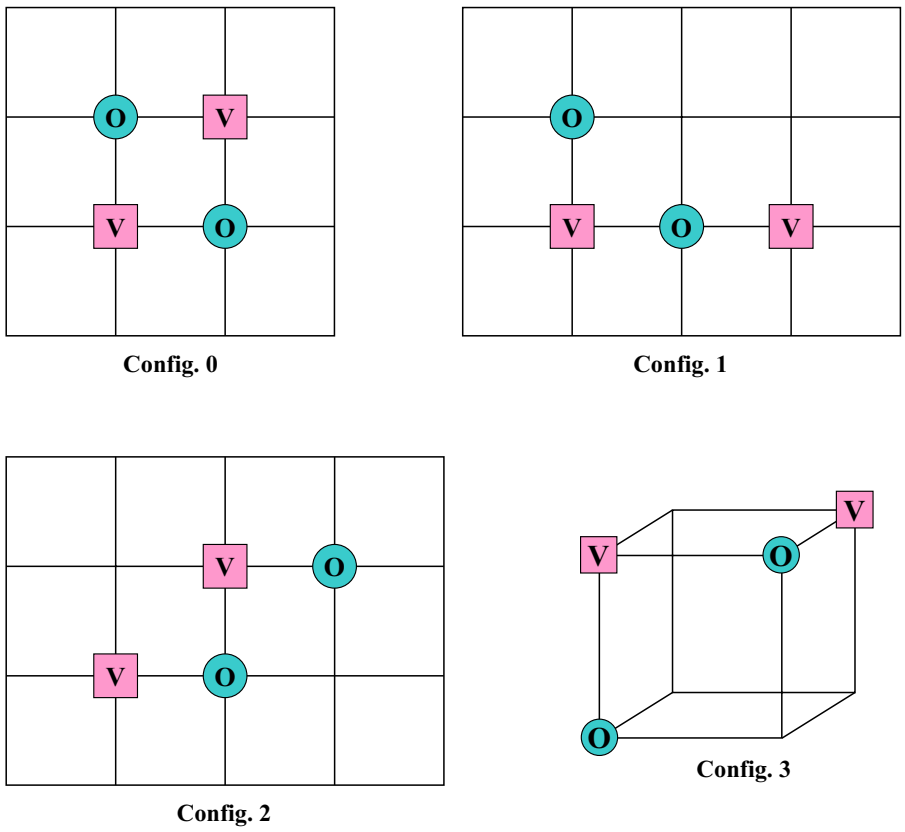

Figure 6.6: Configurations of aggregations of the OV dipoles in the CaF_2 bulk.

0 when one vacancy switches its position. I found, that the energetically most favorable $(OV)_2$-dimer orientation is configuration 0 (see Figure 6.6). The association energy of two dipoles in configuration 0 is 0.55 eV. This energy is the energy difference between the same two remote dipoles and the $(OV)_2$-dimer of configuration 0. So, we can see, that there is some attraction effect between two OV dipoles in a CaF_2 crystal. The interaction energy between the periodically repeated OV dipoles in our calculations is negligible. The association energy of two OV dipoles calculated by Mysovsky *et al.* (2004) (0.48 eV) is close to my result. The relative energies of configurations 1-3 are given in Table 6.2.

Table 6.2: Energies of three different $(OV)_2$-dimer mutual orientations with respect to configuration 0 (see Figure 6.6).

Configuration	My results (eV)	Theory [a] (eV)
1	+0.54	+0.375
2	+0.37	+0.361
3	+0.34	+0.307

[a]Reference Mysovsky *et al.* (2004)

6.3 OV centers at the CaF_2 (111) surface

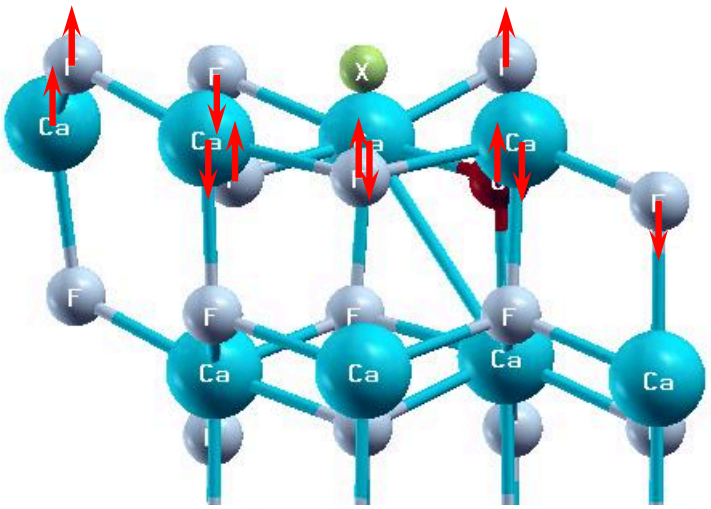

Figure 6.7: Side view of the OV center placed at the CaF_2 (111) surface. The directions of atomic displacements in the (111) axis are shown with arrows.

As an extension of my pervious study of OV dipoles in the CaF_2 bulk, I investigated the OV dipole placed at the CaF_2 (111) surface (see Figure 6.7), which is the most stable one among the (111), (110) and (100) terminated surfaces. As we can see in Figure 6.8, for the (111) slab, there are three sublayers in each layer from the side view. For the surface OV center, the oxygen impurity atom and

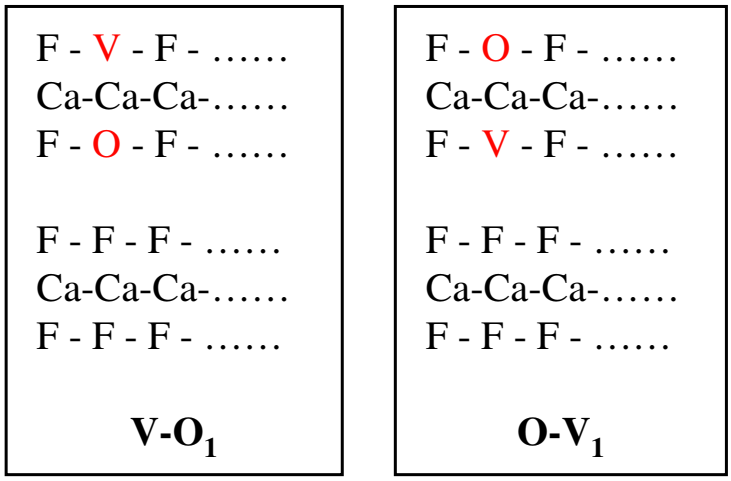

Figure 6.8: Sketch of the OV center placed at the CaF_2 (111) surface.

the fluorine vacancy occupy upper and lower fluorine sublayers, respectively. I found, that energetically the most favorable situation for the surface OV center is the situation V-O_1 (see Figure 6.8). The situation O-V_1 is energetically 0.42 eV less favorable, and finally the OV dipole in the CaF_2 bulk is less energetically favorable, as the surface configuration V-O_1 by 0.59 eV. So, it implicates a trend of OV dipoles to locate near the surface.

I also calculated the relaxation of the atoms near the (111) surface. According to my calculations, the distance between the fluorine-site vacancy and the oxygen impurity for the V-O_1 case is reduced by 0.046 Å (0.84% of a_0) with respect to the bulk OV-center case. For the O-V_1 case, the O-V distance decreases by 0.159 Å (2.89% of a_0). The effective charges of the OV center at the CaF_2 (111) surface for the V-O_1 case are -0.061 e for the vacancy and -1.608 e for the oxygen impurity. To compare with the OV center in the CaF_2 bulk (V: -0.082 e; O: -1.598 e), the vacancy charge increases by 0.021 e, and the O charge decreases by 0.010 e. Unlike the V-O_1 case, for the O-V_1 case in comparison with the OV center in the CaF_2 bulk, the oxygen impurity charge (-1.545 e) increases by 0.053 e, and the vacancy charge (-0.088 e) is reduced by 0.006 e. The bond population between

the fluorine-site vacancy and oxygen impurity in the CaF_2 (111) surface is +52 *me* for the V-O_1, which is comparable, but slightly weaker, as the corresponding bond population value in the CaF_2 bulk (+62 *me*). However, for the situation O-V_1, this bond population (+70 *me*) increases slightly by 8 *me*. According to my calculations of *OV* centers in deeper CaF_2 (111) layers, the differences such as O-V distance, effective charges and bond populations between V-O and O-V configurations become smaller and smaller, and finally disappear.

Table 6.3: Direct optical gaps (eV) ($\Gamma \rightarrow \Gamma$) of the *OV* center at the CaF_2 (111) surface. V indicates the vacancy band; O_1, O_2 and O_3 are three oxygen bands.

Optical gaps	V-O_1	O-V_1	Bulk
$O_1 \rightarrow$ V	7.22	6.06	6.40
$O_2 \rightarrow$ V	7.30	6.49	6.52
$O_3 \rightarrow$ V	7.38	6.54	6.66
VB $\rightarrow$ V	9.84	9.82	9.48
$O_1 \rightarrow$ CB	8.04	6.60	7.71
VB $\rightarrow$ CB	10.66	10.36	10.79

Next, I calculated the band structure for the *OV* center located at the CaF_2 (111) surface (see Figure 6.9). The optical band gaps for the surface *OV* center in CaF_2 are collected in Table 6.3. The band gap between CB and VB ($\Gamma \rightarrow \Gamma$) for the V-$O_1$ system (10.66 eV) is reduced with respect to the CaF_2 bulk *OV*-center case (10.79 eV). The narrowing of the surface band gap is in line with my previous studies of perfect slabs and surface *F* centers. The fluorine-site vacancy induces an empty vacancy level, which mainly consists of the vacancy *s*-orbitals, 9.84 eV above the VB top in the V-O_1 case and increases by 0.36 eV with respect to the bulk *OV*-center case (9.48 eV). The oxygen *p*-orbitals in the V-O_1 case are split into three bands near the Fermi energy. The splits are around 0.08 eV, smaller than in the bulk, and the separation between oxygen bands O_1 and O_3 is 0.16 eV. The three oxygen bands in the V-O_1 configuration at Γ point are located 2.62 eV, 2.54 eV and 2.46 eV above the top of VB and move toward the VB top with respect to the bulk case. In the configuration of O-V_1 at Γ point, the band

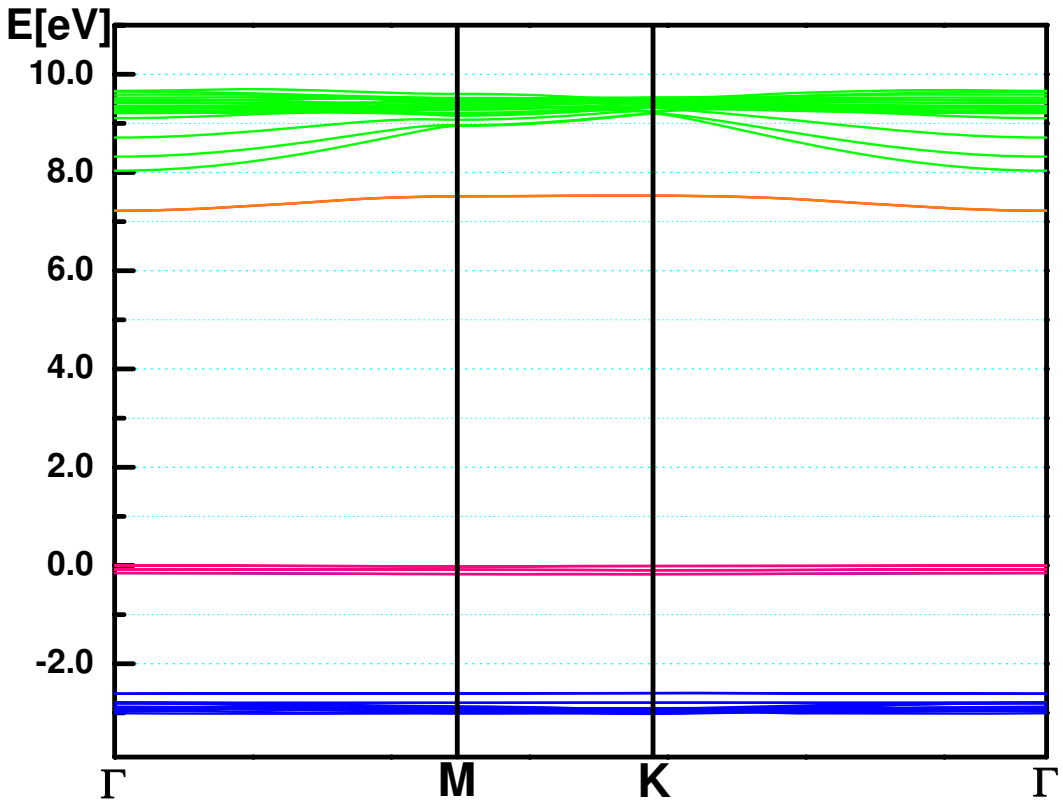

Figure 6.9: Band structure of the OV center at the CaF_2 (111) surface for the V-O_1 case.

gap between CB and VB (10.36 eV) is even more strongly reduced with respect to the CaF_2 bulk OV-center case and the three oxygen bands, unlike the V-O_1 case, slightly shift upward and are located 3.28 eV, 3.33 eV and 3.76 eV above the VB top.

Conclusions

According to my calculated results for the OV center in the CaF_2 bulk, the optical absorption bands at the Γ point are 6.40 eV, 6.52 eV and 6.66 eV, in good agreement with the experimental value (6.7 eV) for the complex absorption bands with separation interval of 0.48 eV. Several configurations of the $(OV)_2$-

dimer were calculated. The association energy for the most favorable one is 0.55 eV.

Chapter 7

Hydrogen centers in CaF_2 and BaF_2

Introduction

In this Chapter, I performed *ab initio* calculations to determine the electronic structure and atomic geometry of the hydrogen impurities in CaF_2 and BaF_2. Two kinds of hydrogen impurities, namely H_s^- centers and H_i^0 centers, defined detailedly in this Chapter, were calculated by means of the hybrid B3PW method. Firstly, I introduced the hydrogen centers in CaF_2 and BaF_2 bulks. In a second part of this Chapter, I presented the H_s^- centers in the CaF_2 and BaF_2 (111) surfaces.

7.1 Method of calculations

The calculations for the hydrogen centers in CaF_2 and BaF_2 crystals were performed using the hybrid B3PW method. The hybrid B3PW functional has been proved to yield remarkably accurate electronic and geometrical structures for CaF_2 and BaF_2 crystals, as well as for ABO_3 perovskites [Eglitis *et al.* (2004); Heifets *et al.* (2001); Piskunov *et al.* (2004)].

In this Chapter, I used the same basis sets for the Ca, Ba and F atoms as in my previous study, dealing with the CaF_2 and BaF_2 electronic structure and F

centers therein. For the H atom, I used the basis set developed by Dovesi *et al.* (1984). The reciprocal space integration was performed by sampling the Brillouin zone of the unit cell with the $8 \times 8 \times 8$ Pack-Monkhorst net [Monkhorst & Pack (1976)].

In this Chapter, like before, I used a *periodic supercell* model of the hydrogen center combined with a first-principles method for the calculations of its atomic and electronic structure. In order to calculate the hydrogen centers, for the H_s^- centers, I started with a 81-atom supercell with one of the fluorine atoms substituted by a H^- ion, and for the H_i^0 case, I inserted one hydrogen atom into an atomic interstitial site of the supercell. The 81-atom supercell is a primitive f.c.c unit cell which is extended three times along all three translation vectors. After the hydrogen atom substitutes or is inserted, the atomic configuration of the surrounding atoms is re-optimized via a search of the total energy minimum as a function of the atomic displacements from the regular lattice sites.

In previous discussion (Chapter 5) dealing with F centers in CaF_2 and BaF_2, I carefully investigated the effect of the supercell size on various defect properties. I found, that the F center formation energy converges for a supercell containing 48 atoms. The width of the defect band is very small. Because of the more localized electron of the hydrogen center, the interaction between the periodically repeated defects will be less than in the F-center case. Therefore, I believe that a 81-atom supercell is sufficient in the present case.

At this point, I should address the question of the stability of the hydrogen impurities. As mentioned in Chapter 2, experimental works have clearly shown that hydrogen impurities can be trapped in several local minima of the energy hypersurface and thus show metastability. Typical activation barriers for conversion from the fluorine site to the interstitial site are of the order of 0.37 eV for CaF_2 and 0.33 eV for BaF_2 [Hayes (1974)]. Therefore, quantum effect should be negligible and, within the Born-Oppenheimer approximation, it should be a sound procedure to treat the hydrogen as a classical particle. This is in accordance with other recent theoretical work, i.e. on interstitial hydrogen in $PbTiO_3$ [Park & Chadi (2000)].

7.2 Hydrogen centers in CaF_2 and BaF_2 bulks

7.2.1 Calculated results for the H_s^- centers in CaF_2 and BaF_2 bulks

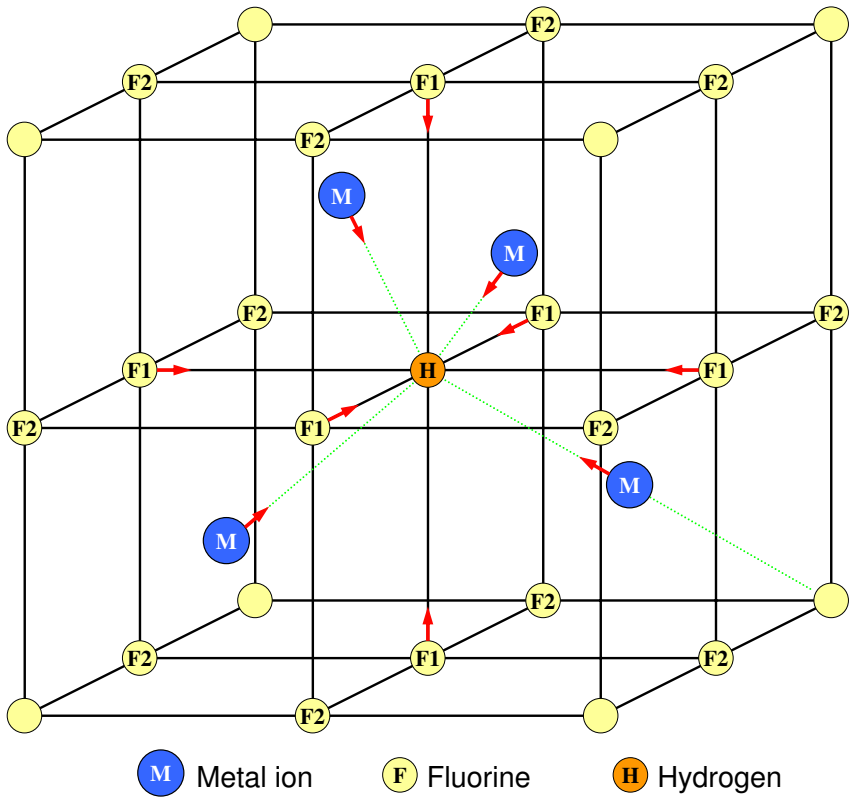

Figure 7.1: A view of the H_s^--center nearest-neighbor geometry with the indication of relaxation shifts. According to the symmetries of the atoms, different labels are defined in circles.

H_s^- center, a fluorine ion substituted with a H^- ion at an anion site in CaF_2 and BaF_2, was calculated by means of the hybrid B3PW method. Figure 7.1 shows the geometry relaxations of the atoms surrounding the H_s^- center in CaF_2 and BaF_2, see also Table 7.1. For the CaF_2 H_s^--center case, the conclusion is that, unlike the repulsive displacements of the four nearest Ca atoms surrounding

Table 7.1: Atomic relaxations of 10 atoms surrounding a H_s^- center in CaF_2 and BaF_2 81-atom supercells, (in percent of the lattice constants, a_0=5.50 Å for CaF_2 , a_0=6.26 Å for BaF_2). Positive signs indicate the outward movements of the H_s^- center.

		CaF_2	BaF_2
Atom	Number of atoms	D (% a_0)	D (% a_0)
M	4	-0.04	+0.09
F1	6	-0.13	-0.08

the F center in CaF_2 crystal, the Ca atoms are slightly displaced toward the H_s^- center. The six 2nd-nearest F atoms move also toward the hydrogen. For the BaF_2 H_s^--center system, the four nearest Ba atoms are displaced outward of the hydrogen and therefore have the opposite directions with respect to the CaF_2 case. According to my calculations, I found that all these relaxations are very small. This phenomenon can be explained by looking at the effective charges.

Table 7.2: The effective charges (Q(e)) of the H_s^- center and surrounding atoms in the CaF_2 and BaF_2 bulk. ΔQ(e) is the charge difference between the defective and perfect CaF_2/BaF_2 crystal. (For the CaF_2 bulk, Ca: +1.803 e, F: -0.902 e. For the BaF_2 bulk, Ba: +1.845 e, F: -0.923 e.)

		CaF_2		BaF_2	
Atoms	Number	Q (e)	ΔQ (e)	Q (e)	ΔQ (e)
H	1	-0.895	+0.007	-0.895	+0.028
M	4	+1.801	-0.002	+1.841	-0.004
F1	6	-0.902	0	-0.924	-0.001
F2	12	-0.901	+0.001	-0.923	0

The charge density map for the H_s^- center in CaF_2 bulk is shown in Figure 7.2. The H_s^- center for the BaF_2 crystal has a similar charge density map. Table 7.2 presents the effective charges of the H_s^- center and the surrounding atoms.

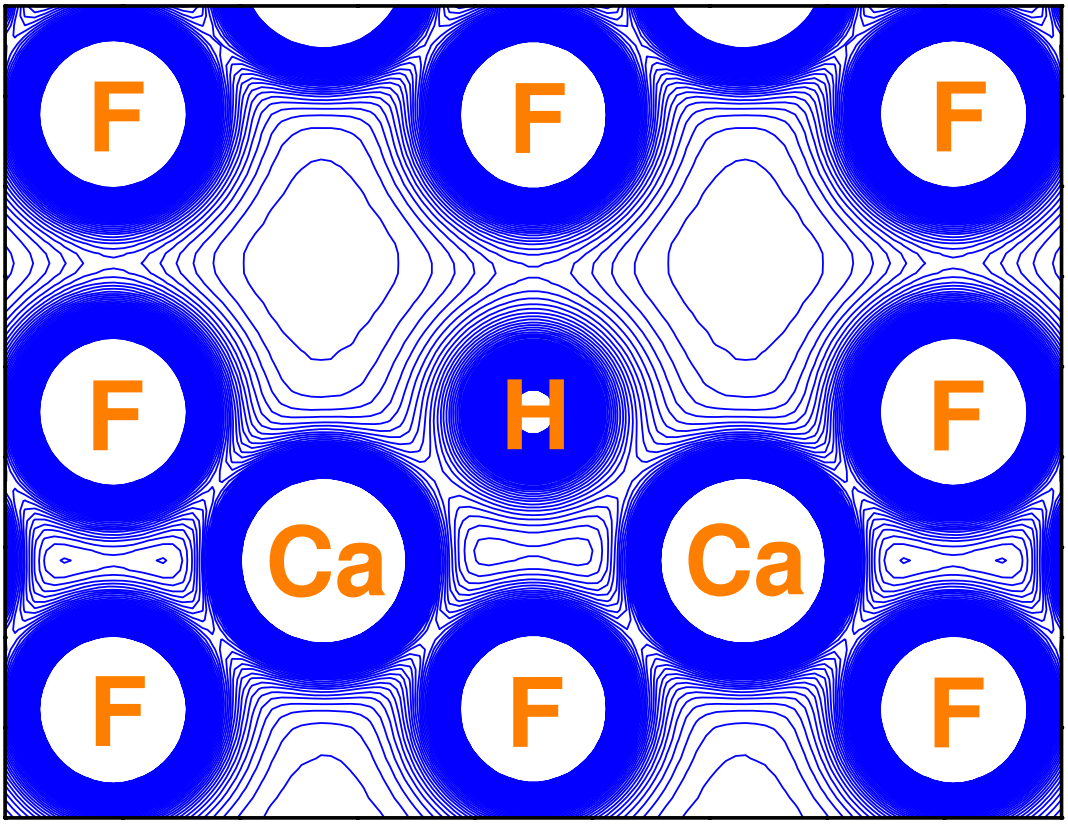

Figure 7.2: Charge density map of a CaF_2 crystal with the periodic H_s^- center from the (1 1 0) side view. Isodensity curves are drawn from 0 e/bohr^3 to 0.2 e/bohr^3 with an increment of 0.002 e/bohr^3.

The analysis shows that the effective charge of the hydrogen ion in CaF_2 and BaF_2 is close to the F ion charge in CaF_2 and BaF_2 perfect crystals. These calculated results explain the negligible relaxations of the atoms surrounding the H_s^- center. According to my calculations, although the F ion charges in CaF_2 are quite different from those in BaF_2, the effective charges (-0.895 e) of the H_s^- center are almost the same in both materials. However, further analysis of effective charges in each basis set shell shows that, the H_s^- center in CaF_2 is more localized than in BaF_2, though the Mulliken effective charges are almost the same, since more electrons occupy the outer s-orbital for BaF_2. For the charge transfer

from ions to ions, in the CaF_2 case, the charge difference (0.007 e) of the H_s^- center is almost localized on the four nearest Ca atoms; for the BaF_2 crystal, around -0.016 e and -0.006 e from the H_s^- are localized on the four nearest Ba atoms and the six 2nd-nearest neighbor fluorine atoms, respectively.

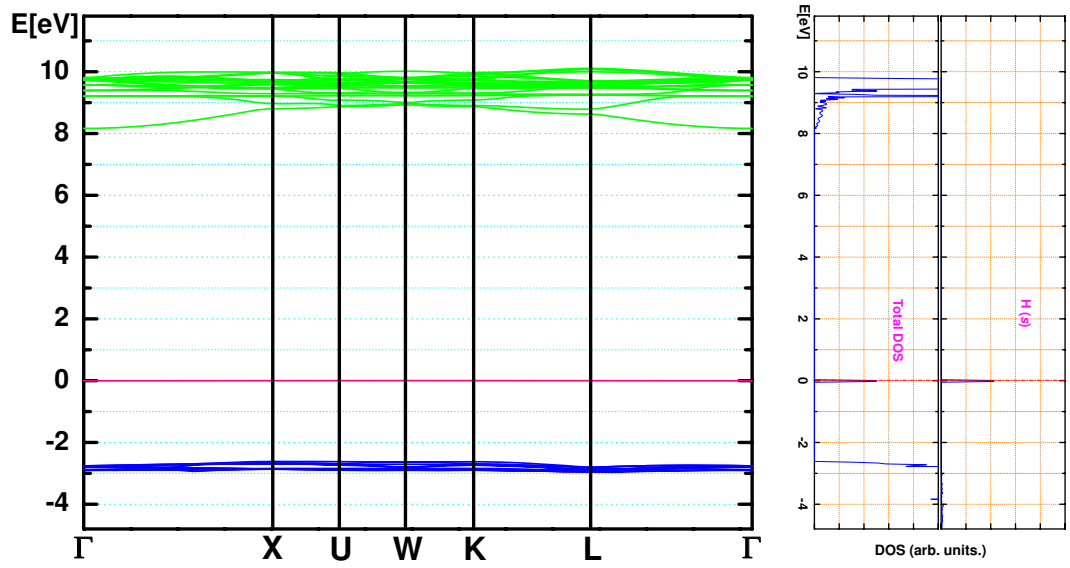

Figure 7.3: Calculated band structure and DOS (density of states) for the 81-atom supercell modeling the H_s^- center in CaF_2.

Table 7.3: Direct optical gaps (eV) ($\Gamma \rightarrow \Gamma$) of the H_s^- center in CaF_2 and BaF_2 bulks.

	CaF_2	BaF_2
$H_s^- \rightarrow$ CB	8.17	8.27
VB — H_s^-	2.75	3.07

Next, I calculated the band structure of the H_s^- center in CaF_2 and BaF_2 bulks. The defect-defect coupling due to the periodically repeated defects in my supercell model is negligible for the 81-atom supercell, since the widths of the defect bands are only 0.004 eV for the CaF_2 case and 0.0005 eV for the BaF_2 crystal. The H_s^- defect band at Γ point is located 2.75 eV for CaF_2 and

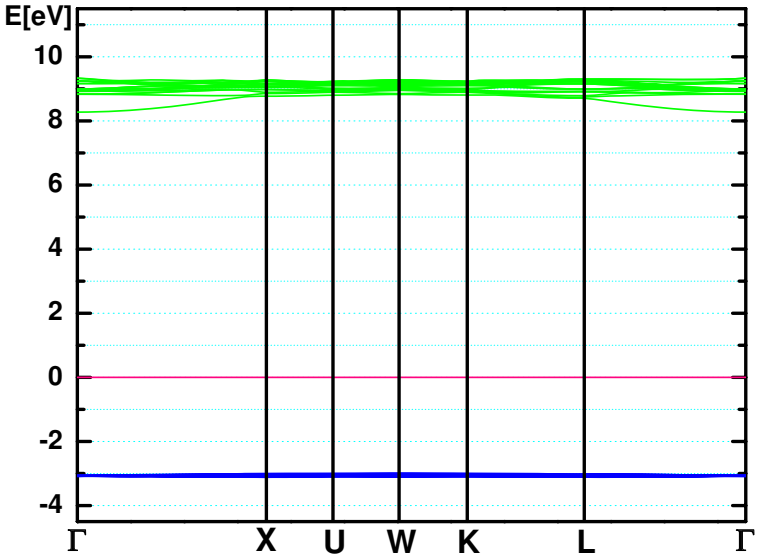

Figure 7.4: Calculated band structure for the 81-atom supercell modeling the H_s^- center in BaF_2.

3.07 eV for BaF_2 above the top of the valence band (VB) (see Figure 7.3 and 7.4). As mentioned in previous Chapters, I suggest a possible mechanism for the optical absorption. Though it is an approximation only, in the present case some justification can be drawn. The experimentally observable optical absorption could be due to an electron transfer from the H_s^--center ground state to the conduction band (CB) bottom. The corresponding calculated values for CaF_2 and BaF_2 are 8.17 eV and 8.27 eV, respectively. Experimentally, the transition energy of the H_s^- center in CaF_2 is 7.65 eV, and my calculated result is in agreement with the experiment [Beaumont *et al.* (1970)]. For the BaF_2 case, this experimental value is 6.00 eV [Beaumont *et al.* (1970)], and my calculation is reasonable but overestimates it by 2.27 eV. Additionally, the H_s^- band for BaF_2 lies higher than for CaF_2 above the VB top. It is due to the less localized electrons of the H_s^- center for BaF_2, as discussed before.

In comparison with previous studies dealing with F centers in CaF_2 and BaF_2, I found that the H_s^- bands are located not so high above the top of VB as for the F-center cases. The corresponding value of the F-center in the CaF_2 bulk

is 6.75 eV, much larger as for the H_s^- case (2.75 eV) (see Table 7.3). For BaF_2, the F center band lies 7.01 eV above the VB top, but the H_s^- band is located only 3.01 eV above the VB top. I suggest that this phenomenon is due to the localization difference of the effective charge between the H_s^- center and the F center. The effective charge of the F center in CaF_2 is -0.752 e and the H_s^-'s charge is -0.895 e, it means, that the H_s^- center is more localized. A similar effect was also observed for the oxygen-vacancy dipoles in CaF_2 in Chapter 6.

The total and partial density of states (DOS) of the H_s^- center in CaF_2 bulk are displayed in the right part of Figure 7.3. The results of my calculations show that the H_s^- s-orbitals do the most contributions to the H_s^- band. The F p-orbitals form the upper VB and the H_s^- defect level is primarily composed of hydrogen s-orbitals, whereas the CB bottom consists mainly of metal ion d-orbitals.

7.2.2 Calculated results for the H_i^0 centers in CaF_2 and BaF_2 bulks

Table 7.4: The effective charges (Q(e)) of the H_i^0 center and surrounding atoms in the CaF_2 and BaF_2 bulk. ΔQ(e) is the charge difference between the defective and perfect CaF_2/BaF_2 crystal. Spin (e) is expressed as (n_α - n_β).

		CaF_2			BaF_2		
Atoms	Number	Q (e)	ΔQ (e)	Spin (e)	Q (e)	ΔQ (e)	Spin (e)
H	1	-0.097	—	0.953	-0.061	—	0.956
F	8	-0.888	+0.014	0.004	-0.914	+0.009	0.004
M	6	+1.801	-0.002	0.001	+1.844	-0.001	0.001

I also investigated another kind of hydrogen centers in alkaline-earth fluorides, namely H_i^0 center, which is a hydrogen atom occupying an interstitial site (see Figure 7.5). The redistribution of the electrons after H_i^0-center formation in CaF_2 can be seen in Figure 7.6 for a supercell containing 82 atoms. The analysis of the effective charges shows that the H_i^0-center charge has a very small and negative

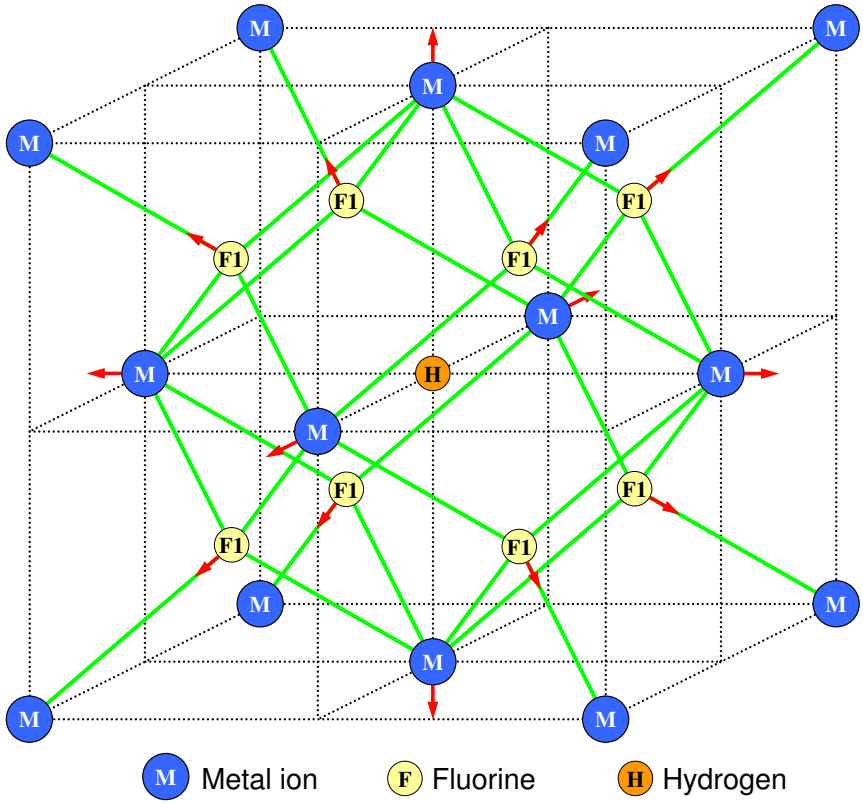

Figure 7.5: A view of the H_i^0-center nearest-neighbor geometry with the indication of relaxation shifts.

value (see Table 7.4). This charge arises mainly from the eight nearest fluorine ions. As we can see from Table 7.4, the charge change of the nearest fluorine ions is +0.014 e for CaF_2 and +0.009 e for BaF_2. Bond population analysis shows that the bond populations between the hydrogen impurity atom and the nearest fluorine ions (-26 me for CaF_2 and -2 me for BaF_2) are close to the F-F bond populations in the perfect crystal (-22 me for CaF_2 and -2 me for BaF_2). The localization of an unpaired electron at the H_i^0 center is clearly evident at the center of the spin map (Figure 7.6) and the spin polarization of the nearest neighboring F atoms is appreciable obviously. However, this spin polarization effect to the further atoms is very weak. The spin density of the nearest F ions

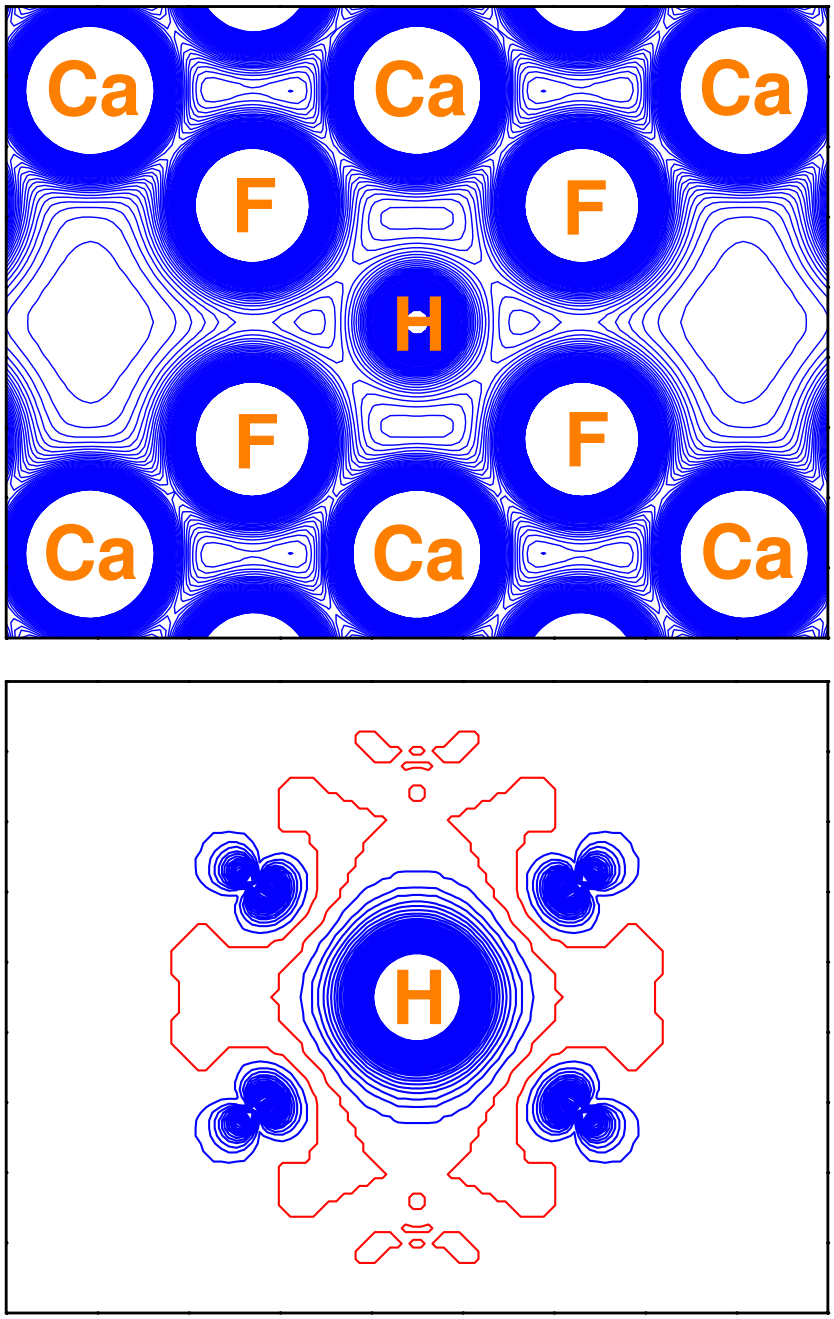

Figure 7.6: Electron charge (upper) and spin (lower) density map of a CaF_2 crystal with the periodic H_i^0 center from the (1 1 0) side view. Isodensity curves are drawn from 0 e/bohr^3 to 0.2 e/bohr^3 with an increment of 0.002 e/bohr^3 (charge) and drawn from -0.05 e/bohr^3 to 0.3 e/bohr^3 with an increment of 0.001 e/bohr^3 (spin). Blue and red lines in the spin density map denote positive and zero values, respectively.

and the second-nearest metal ions are only 0.004 e and 0.001 e, respectively (see Table 7.4).

Table 7.5: Atomic relaxations of the atoms surrounding a H_i^0 center in CaF_2 and BaF_2. Positive signs indicate the outward movements of the H_i^0 center.

		CaF_2	BaF_2
Atom	Number of atoms	D (% a_0)	D (% a_0)
F1	8	+0.36	+0.17
M	6	+0.08	$<$ +0.01

The relaxation of the atoms surrounding the H_i^0 center are shown in Figure 7.5. The conclusion is that the repulsions of the eight nearest F^- ions and the six second-nearest-neighbor metal ions from the H_i^0 center for both CaF_2 and BaF_2 are rather small (see Table 7.5). These small outward displacements of atoms surrounding the H_i^0 center can be explained by the fact that the H_i^0 charge is close to zero.

Table 7.6: Direct optical gaps (eV) ($\Gamma \rightarrow \Gamma$) of the H_i^0 center in CaF_2 and BaF_2 bulks.

	CaF_2		BaF_2	
Optical Gaps	α	β	α	β
$H_i^0 \rightarrow$ CB	9.15	3.54	10.52	4.54
VB $\rightarrow H_i^0$	1.80	7.44	0.81	6.81

To investigate the optical properties of H_i^0 centers in CaF_2 and BaF_2, I calculated the band structure of periodically repeated H_i^0 center in my supercell model (see Figure 7.7 and 7.8). The inserted hydrogen atom has only one electron, so there is an unpaired electron in each supercell. As mentioned in previous study dealing with F center in Chapter 5, the bound unpaired electron level lies in the band gap; the corresponding unoccupied level appears in the β-spin structure, again in the gap, but at positive energies. Following the previous F-center

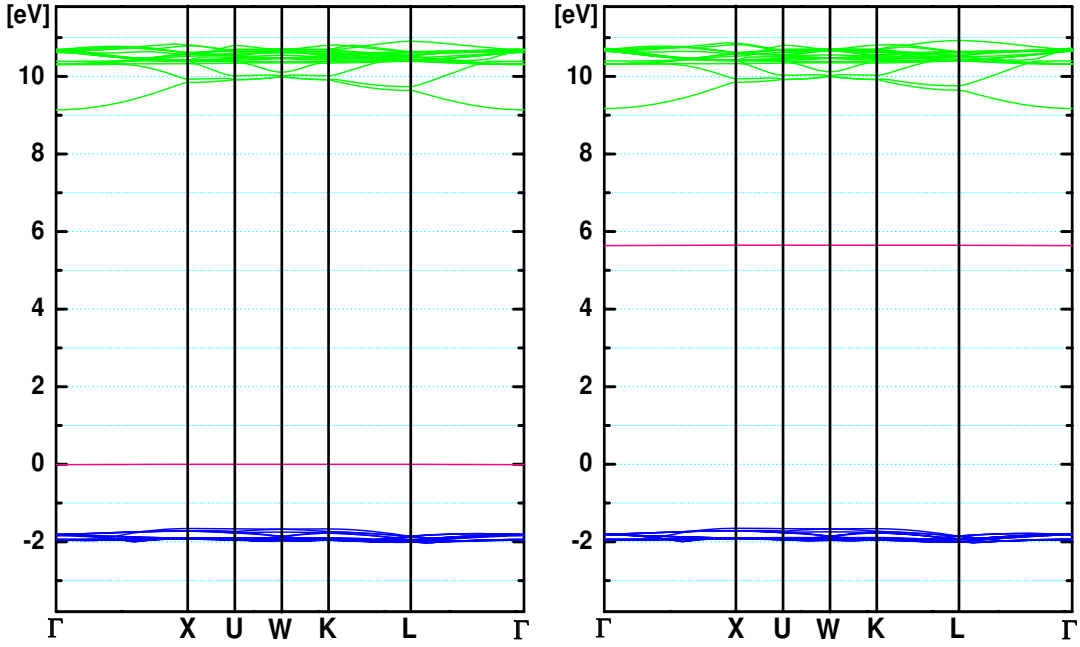

Figure 7.7: Calculated band structure for the 82-atom supercell modeling the H_i^0 center in CaF_2. α (left) and β (right) denote the up- and down-spin states, respectively.

discussion, I can now suggest a possible mechanism for the optical absorption of H_i^0-center systems. In the ground state, the defect band is occupied in the α-spin system and unoccupied in the β-spin system (see Figure 7.7 and 7.8). The optical absorption corresponds to an electron transition from the H_i^0-center ground state to the CB. Because of the selection rules, the electron transition from the α occupied band to the β unoccupied band is forbidden. My calculated optical gap between the α band and the CB is 9.15 eV and 10.52 eV for the CaF_2 and BaF_2 cases, respectively (see Table 7.6). These values are larger than for H_s^- case. Unfortunately, I did not find any experimental data for the H_i^0-center optical absorption in literature.

The calculated total and partial density of states (DOS) of the H_i^0 center in CaF_2 bulk are displayed in Figure 7.9. The results of my calculations show, like H_s^- case, that the hydrogen s-orbitals do the most contributions to the defect

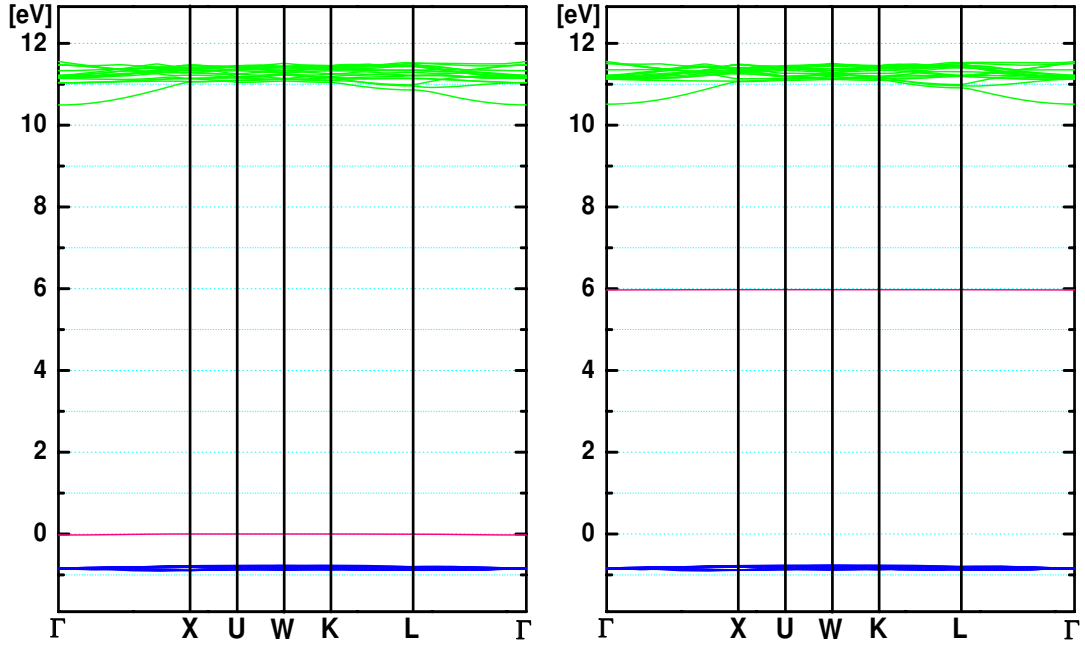

Figure 7.8: Calculated band structure for the 82-atom supercell modeling the H_i^0 center in BaF_2. α (left) and β (right) denote the up- and down-spin states, respectively.

bands (α band and β band).

Similar to the F-center case, due to the presence of an unpaired electron and the interaction between the unpaired spin and the spin of neighboring nuclei, a hyperfine structure of the EPR spectra also can be detected in H_i^0-center system. My calculated hydrogen and the nearest fluorine hyperfine parameters are compared with experiment in Table 7.7 and are in excellent agreement with experiment.

7.3 Surface H_s^- centers in CaF_2 and BaF_2

As an extension of my study dealing with H_s^- centers in CaF_2 and BaF_2 bulk, I investigated the H_s^- center placed at the (111) surface, which is the most stable one among the (100), (110) and (111) terminated surfaces for CaF_2 and

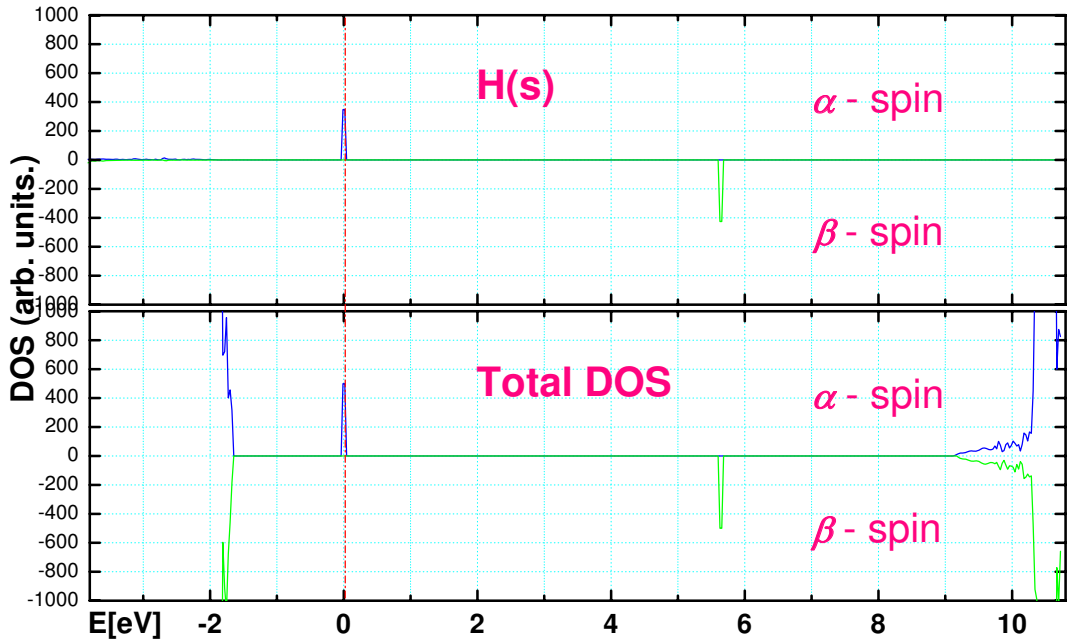

Figure 7.9: Total and projected density of states (DOS) for the H_i^0 center in CaF_2 bulk. α and β denote the up- and down-spin states, respectively.

BaF_2. In this Chapter, I performed my surface H_s^- center calculations for a slab containing four layers. Each layer consists of three sublayers, containing nine atoms. Therefore, the supercell used in my calculations contains 108 atoms.

The relaxations of the atoms near the (111) surface are presented in Table 7.8 and Figure 7.8. The hydrogen ions at the surface move outward by 1.02% of a_0 for CaF_2 and by 0.81% of a_0 for BaF_2. Otherwise, the six neighbor F atoms at the same upper sublayer move inward. The relaxations of the three neighbor metal ions at the middle sublayer of the surface layer, moving inward for CaF_2 and outward for BaF_2, are in qualitative agreement with my previous studies about the perfect (111) slabs for CaF_2 and BaF_2. The H_s^--M (metal ion) distance increases by 0.62% of a_0 for CaF_2 and by 0.15% of a_0 for BaF_2 with respect to the corresponding value of bulk H_s^- case. In comparison with the bulk H_s^--center case, for the surface H_s^--center system, we can conclude that the atoms surrounding the H_s^- center show a stronger repulsion to the hydrogen ion located at the surface.

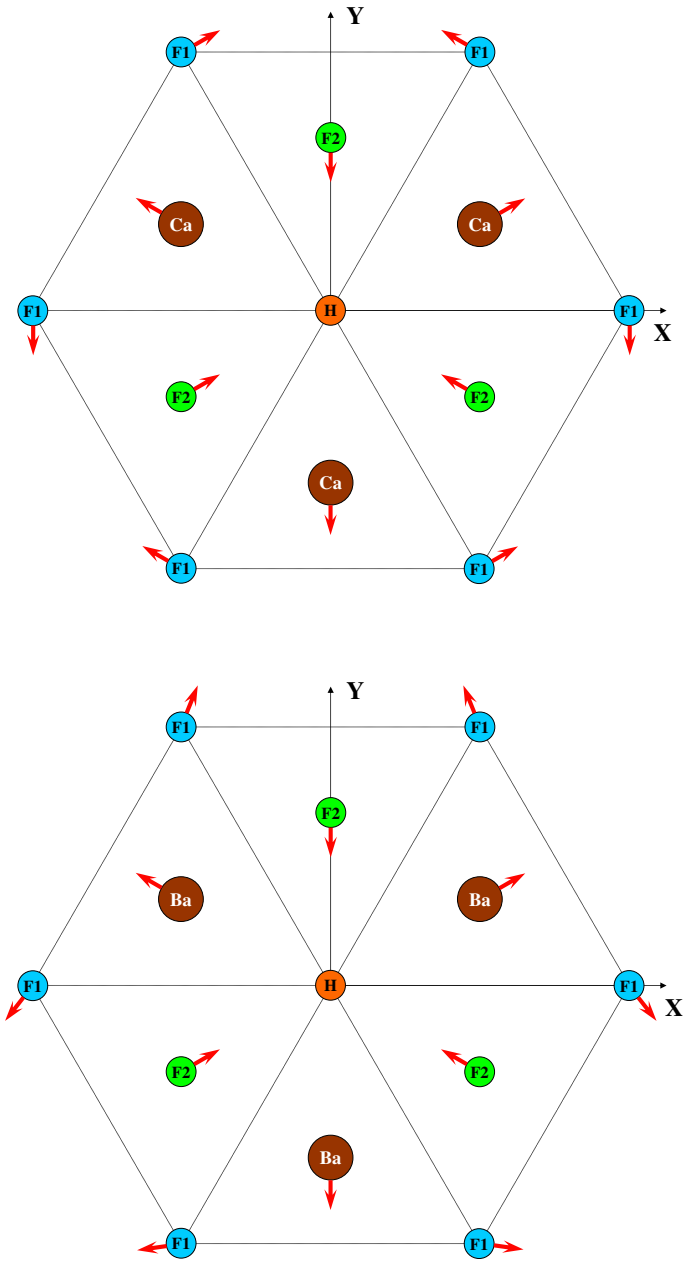

Figure 7.10: A top view of the surface H_s^--center nearest-neighbor geometry with the indication of the atomic displacement directions. F1 indicates the fluorine atoms located at the upper sublayer, and F2 means the fluorine atoms located at the lower sublayer.

Table 7.7: Observed and calculated isotropic hyperfine constants a and anisotropic hyperfine constants b (MHz) for the H_i^0 center in CaF_2 and BaF_2.

	CaF_2		BaF_2	
Hyperfine constants	My results	Expt[a]	My results	Expt[b]
a	99.5	104	38.6	41
b	35.2	34.93	20.9	21

[a]Reference Hall & Schumacher (1962)
[b]Reference Bessent *et al.* (1969)

Table 7.8: Atomic relaxation of the CaF_2 or BaF_2 slab containing an H_s^- center located at the (111) surface (as a percentage of the lattice constant). Positive signs correspond to outward atomic displacements (toward the vacuum). The directions of atomic displacements in the XY-plane are indicated in Figure 7.8.

		CaF_2		BaF_2	
Atoms	Number	XY (% a_0)	Z (% a_0)	XY (% a_0)	Z (% a_0)
H_s^-	1	—	+1.02	—	+0.81
F1	6	0.16	-0.59	0.25	-0.48
M(Ca/Ba)	3	0.12	-0.35	0.17	+0.55
F2	3	0.32	-0.52	0.51	-0.02

With respect to the electronic structure of the surface H_s^- center, the effective charge analysis shows that the electronic density around it is slightly more delocalized than that corresponding to the bulk H_s^--center case. Table 7.9 presents the effective charge values of the surface H_s^- center and surrounding atoms. The effective charge of the H_s^- center is -0.877 e, 0.018 e less than for the bulk H_s^- center in CaF_2 (see Table 7.9). Otherwise, the BaF_2 surface H_s^- charge value is -0.894 e, only 0.001 e less than in the bulk. The charges of the nearest metal ions of the surface H_s^- center (+1.794 e for CaF_2 and +1.834 e for BaF_2) are reduced by 0.007 e and 0.007 e in comparison with the charges of the relevant Ca ions (+1.801 e) and Ba ions (+1.841 e). Bond populations between the surface H_s^-

Table 7.9: The effective charges (Q(e)) of the surface H_s^- center and surrounding atoms. ΔQ(e) is the charge difference between the defective slab and perfect CaF_2/BaF_2 bulk.

		CaF_2		BaF_2	
Atoms	Number	Q (e)	ΔQ (e)	Q (e)	ΔQ (e)
H_s^-	1	-0.877	+0.025	-0.894	+0.029
F1	6	-0.891	+0.011	-0.918	+0.005
M(Ca/Ba)	3	+1.794	-0.009	+1.834	-0.011
F2	3	-0.907	-0.005	-0.924	-0.001

center and the nearest metal ions were also calculated. The major effect observed here is, like surface F-center case mentioned in Chapter 5, a strengthening of the surface H_s^- and M chemical bond. The surface H_s^--Ca bond population is +6 me and larger than the corresponding value in the bulk by 18 me. For the BaF_2 case, there is a similar, but weaker, strengthening effect of H_s^--Ba bond. The surface H_s^--Ba bond population equals to -30 me, which is larger than the relevant value in bulk by 6 me.

Table 7.10: Direct optical gaps (eV) ($\Gamma \rightarrow \Gamma$) of the (111) surface H_s^- center in CaF_2 and BaF_2.

	CaF_2	BaF_2
$H_s^- \rightarrow$ CB	7.91	7.94
VB — H_s^-	2.87	2.86

The band structures of the surface H_s^- center for CaF_2 and BaF_2 are shown in Figure 7.11. The defect energy band is located 2.87 eV (0.12 eV higher than in the bulk H_s^--center case) for CaF_2 and 2.86 eV (0.21 eV lower than in the bulk H_s^--center case) for BaF_2 above the VB top and is separated from the CB bottom by 7.91 eV and 7.94 eV for CaF_2 and BaF_2, respectively (see Table 7.10). Because of the surface effect, according to my calculations, this gap is smaller than the corresponding value in the bulk H_s^--center case (8.17 eV) by 0.26 eV for CaF_2.

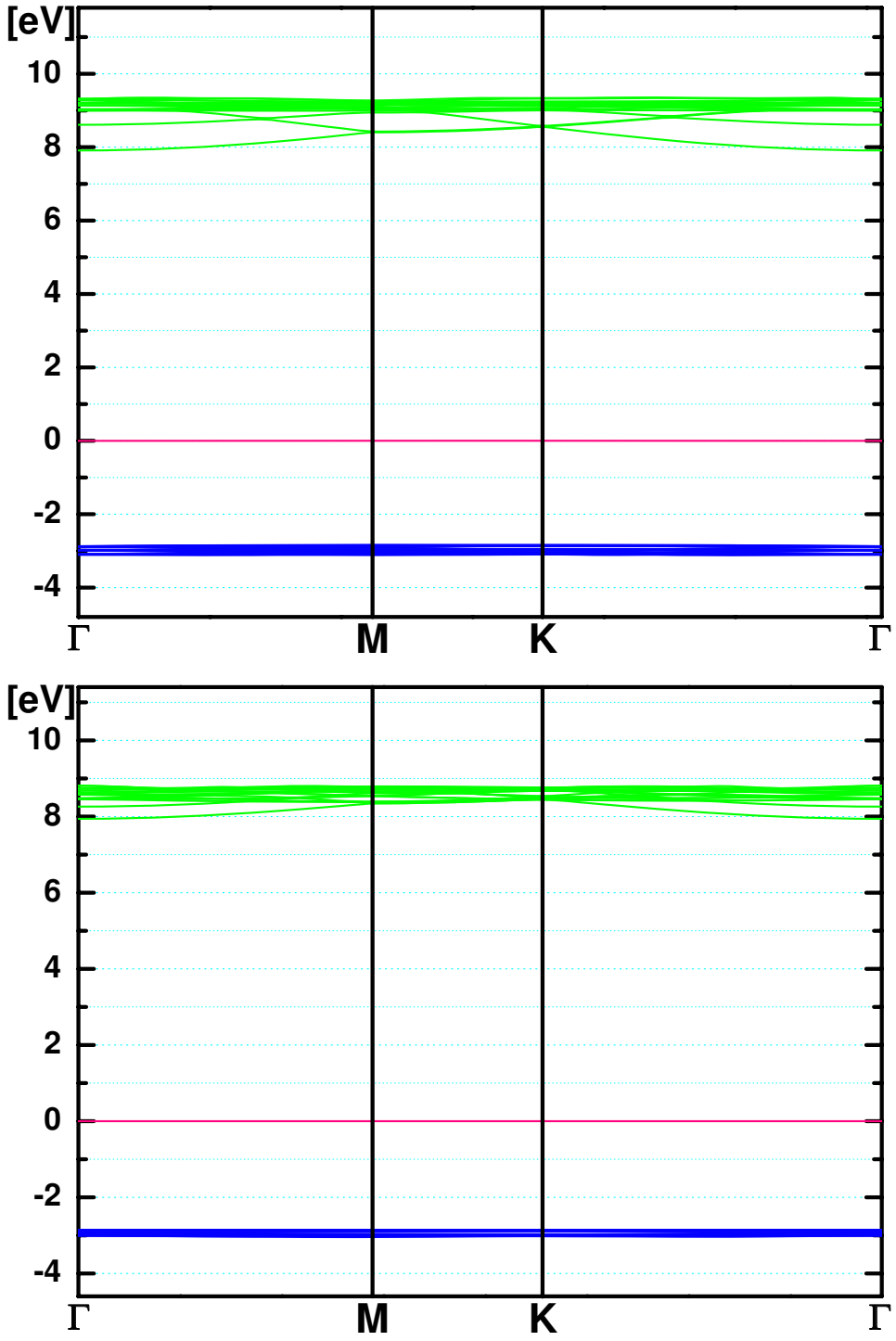

Figure 7.11: Calculated band structure for the 108-atom supercell modeling the H_s^- center in the CaF_2 (upper) and BaF_2 (lower) (111) slabs.

For BaF_2, this gap is reduced by 0.33 eV with respect to the value of the bulk H_s^-center (8.27 eV). The negligible dispersion effect of the defect band for a 108-atom supercell means that the defect-defect interaction is practically eliminated, thus approaching the desired isolated single H_s^--center limit.

Further analysis of the layer-resolved DOS on an expanded energy scale shows the existence of an electronic surface state near the top of the VB. It is found that the DOS of the *p*-orbitals of the surface F ions moves towards higher energies and in this way splits off the bulk continuum. This mechanism is in fact the main reason for the narrowing of the gap at the (111) surface and it happens on both ideal and defective surfaces (see Chapter 4).

Conclusions

My calculated optical absorption energy for hydrogen impurities (H_s^- centers) in CaF_2 (8.17 eV) is close to the experimental result of 7.65 eV, but is overestimated for the BaF_2 crystal. I found, that the defect band induced by hydrogen impurities in CaF_2 and BaF_2 is much more close to the VB top as it was for the F centers in CaF_2 and BaF_2. The hydrogen impurity band in CaF_2 and BaF_2 crystals is located 2.75 eV and 3.07 eV respectively, above the VB.

My calculations show, that the relaxation of the atoms around the hydrogen impurity in CaF_2 and BaF_2 bulk is very small, but the relaxation of surrounding atoms is not any more negligible for a hydrogen impurity located at CaF_2 and BaF_2 surfaces.

I also observed strengthening of the surface H_s^- and M (metal ion) chemical bond. The surface H_s^--Ca bond population is +6 *me* and larger than the corresponding value in bulk by 18 *me*. A similar effect, strengthening of the F center-metal ion bond populations near the surfaces, was also observed in previous studies.

Chapter 8

H centers in CaF_2 and BaF_2

Introduction

In this Chapter, the atomic geometry and electronic structures of the H center in CaF_2 and BaF_2 bulks are presented.

8.1 Method of calculations

I performed calculations for H centers in CaF_2 and BaF_2 bulks using the hybrid B3PW method, which gives the best agreement with experiment for the lattice constants, bulk moduli and optical band gaps for CaF_2 and BaF_2 crystals.

In this Chapter, I used the same basis sets for Ca, Ba and F atoms as in my previous study, dealing with the CaF_2 and BaF_2 electronic structures and F centers therein. The reciprocal space integration was performed by sampling the Brillouin zone of the unit cell with the $6 \times 6 \times 6$ Pack-Monkhorst net [Monkhorst & Pack (1976)]. The calculation thresholds N (i.e., the calculation of integrals with an accuracy of 10^{-N}) where chosen as a compromise between the accuracy of the calculations and the large computational time for the large cells. They are 7, 7, 7, 7 and 14 for the Coulomb overlap, Coulomb penetration, exchange overlap, the first exchange pseudo-overlap and the second exchange pseudo-overlap, respectively [Pisani (1996)].

In this Chapter, I used a *periodic supercell* model of the H center combined with a first-principles method for the calculation of its atomic and electronic structure. The 81-atom supercell is a primitive f.c.c unit cell which is extended three times along all three translation vectors. In order to calculate the H center, I inserted one fluorine atom into the 81-atom supercell. After the fluorine atom is inserted, the atomic configuration of the surrounding atoms is re-optimized via a search of the total energy minimum as a function of the atomic displacements from the regular lattice sites. According to my discussion about the effect of supercell size in previous chapters, I am sure that the 81-atom supercell used in my current H-center calculations is large enough to catch the basic physics of H centers in CaF_2 and BaF_2 bulks.

8.2 Calculated results for the H centers in CaF_2 and BaF_2bulks

H center, a hole trapped at an interstitial anion site (see Figure 8.1), in CaF_2 and BaF_2 bulks, was calculated by means of the hybrid B3PW method. Firstly, I performed calculations of different configurations for the H centers in CaF_2 and BaF_2 bulks. Considering the symmetry of the geometric structure of alkaline-earth fluorides, I calculated two simple configurations in which the H center orients along (100) and (111), respectively. According to my calculations, I found that the energetically more favorable configuration of the H center is the (111) oriented molecular ion. This theoretical conclusion is in agreement with experiment [Hayes (1974)]. For the CaF_2 H center, the total energy of the (100) configuration is higher than the corresponding value of the (111) case by 0.69 eV. For the BaF_2 H center, the (111) total energy is reduced by 0.89 eV with respect to the (100) configuration. Therefore, I focus this Chapter on the investigation of the (111) H center.

Next, I present the geometry relaxation of the atoms surrounding the H center in CaF_2 and BaF_2 (see Figure 8.1). The calculated atomic displacements of the H center and surrounding atoms are listed in Table 8.1. For the CaF_2 H-center case, firstly, the three Ca1 atoms and one Ca2 atom are repulsed from the H

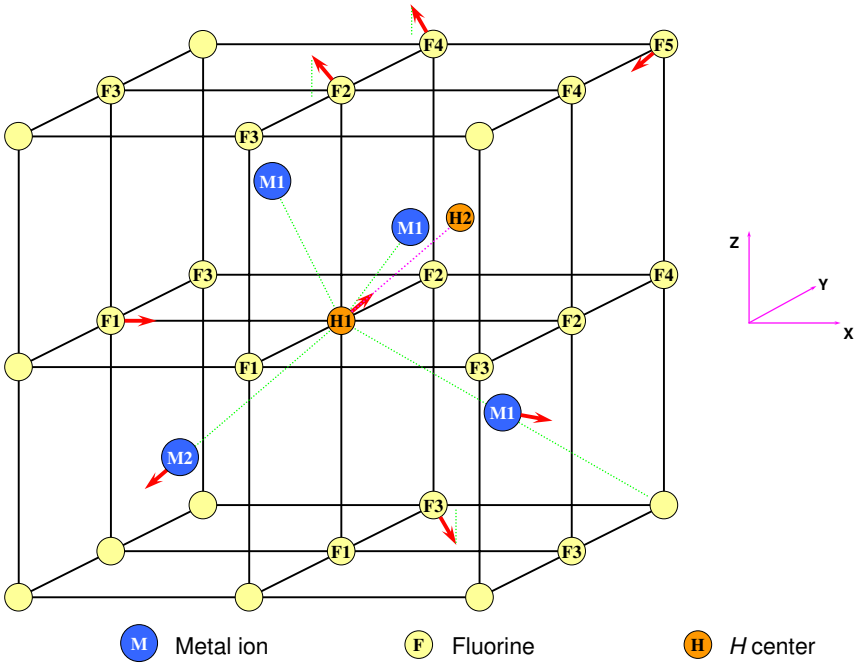

Figure 8.1: H center oriented along the (111) axis. The arrows show the directions of the atomic displacements surrounding the H center. According to the symmetries of the atoms, different labels are defined in circles.

center by 0.97% and 0.77% of the lattice constant (a_0), respectively. F2 and F4 atoms also shift backward the H center and their displacements are 2.37% and 1.07% of a_0, respectively. Oppositely, F1 and F5 atoms are attracted to the H center slightly by 0.74% and 0.40% of a_0, respectively. And finally, the fluorine atom of H1 moves from the anion site towards the H2 atom by 0.67% of a_0. The distance between the H1 and H2 (or named the length of the H center) is 1.98 Å and much shorter than the F-F distance (2.75 Å). The analysis of the relaxation of the H center and surrounding atoms in CaF_2 shows that the relaxation is slightly stronger than for the F-center case in CaF_2 and F2 atoms have considerable movements. This phenomenon can be explained by the forthcoming effective charge discussion. For BaF_2, as we can see in Figure 8.1 and Table 8.1, the relaxation manner of the H center and surrounding atoms is similar to the CaF_2 case. The length of the H center in BaF_2 is 1.98 Å and

Table 8.1: Atomic relaxation of an H center oriented along the (111) axis in the CaF_2 or BaF_2 81-atom supercell (in percent of the lattice constants, a_0=5.50 Å for CaF_2 , a_0=6.26 Å for BaF_2). The shell labels have been defined in Figure 8.1.

	CaF_2	BaF_2
Shells	D (a_0 %)	D (a_0 %)
H1	0.67	0.22
M1	0.97	0.99
M2	0.77	0.71
F1	0.74	0.59
F2	2.37	1.72
F3	0.39	0.27
F4	1.07	0.70
F5	0.40	0.17

essentially the same as the H-center length in CaF_2. I also calculated the length of the H center in SrF_2 and the value (1.97 Å) is very close to the CaF_2 and BaF_2 cases.

The charge density map for the H center in the CaF_2 bulk is shown in Figure 8.2. The H center for the BaF_2 crystal has a similar charge density map. Table 8.2 presents the effective charges of the H center and surrounding atoms for the CaF_2 and BaF_2 bulks. The analysis of the effective charges shows that the total effective charge of the H center in CaF_2 or BaF_2 is close to the single F charge in the CaF_2 or BaF_2 perfect crystal. These calculated results can explain the weak relaxations of the atoms surrounding the H center in CaF_2 or BaF_2. For the CaF_2 case, the total charge of the H center is -0.946 e and is larger than the fluorine charge in the perfect CaF_2 bulk (-0.902 e) by 0.044 e . The H1 charge is -0.664 e and larger than H2 charge (-0.282 e) by a factor of two. For the BaF_2 crystal, calculated H-center charge equals -0.959 e and is also more than the fluorine charge in the perfect BaF_2 bulk (-0.923 e) by 0.036 e. The absolute value of the H1 charge is also much larger than the corresponding value of H2 and

Table 8.2: The effective charges (Q(e)) of the H center and surrounding atoms in CaF_2 and BaF_2 bulks. ΔQ(e) is the charge difference between the defective and perfect CaF_2/BaF_2 crystal. (For the CaF_2 bulk, Ca: +1.803 e, F: -0.902 e. For the BaF_2 bulk, Ba: +1.845 e, F: -0.923 e.)

	CaF_2		BaF_2	
Shells	Q (e)	ΔQ (e)	Q (e)	ΔQ (e)
H1	-0.664	+0.238	-0.623	+0.300
H2	-0.282	+0.620	-0.336	+0.587
M1	+1.799	-0.004	+1.843	-0.002
M2	+1.792	-0.011	+1.842	-0.003
F1	-0.900	+0.002	-0.924	-0.001
F2	-0.895	+0.007	-0.915	+0.008
F3	-0.900	+0.002	-0.922	+0.001
F4	-0.894	+0.008	-0.916	+0.007
F5	-0.890	+0.012	-0.919	+0.004

has an approximate factor of two. Therefore, for the CaF_2 or BaF_2 crystal, the total charge of the H center is not distributed equally between two F atoms. Hall *et al.* (1969) and Beaumont *et al.* (1970) demonstrated that the hole is located on the interstitial fluorine. My calculations of effective charges are in qualitative agreement with their measurements.

The localization of the unpaired electron at the H center is clearly shown in the spin density maps for CaF_2 (see Figure 8.3). From Figure 8.3, we can see that the spin density around the nearest F5 atom is remarkable, the spin density around the nearest F1 and F4 atoms is much weaker and the spin polarization of other neighbor atoms almost disappear (see Figure 8.3 (upper)). According to my calculations, the F5 spin charge (n_α-n_β) is 0.014 e, the F4 and F2 spin charges are 0.005 e and 0.002 e, respectively. The spin charge for H1 0.299 e and H2 0.667 e is also in accordance with the fact that the hole is primarily located on the interstitial fluorine.

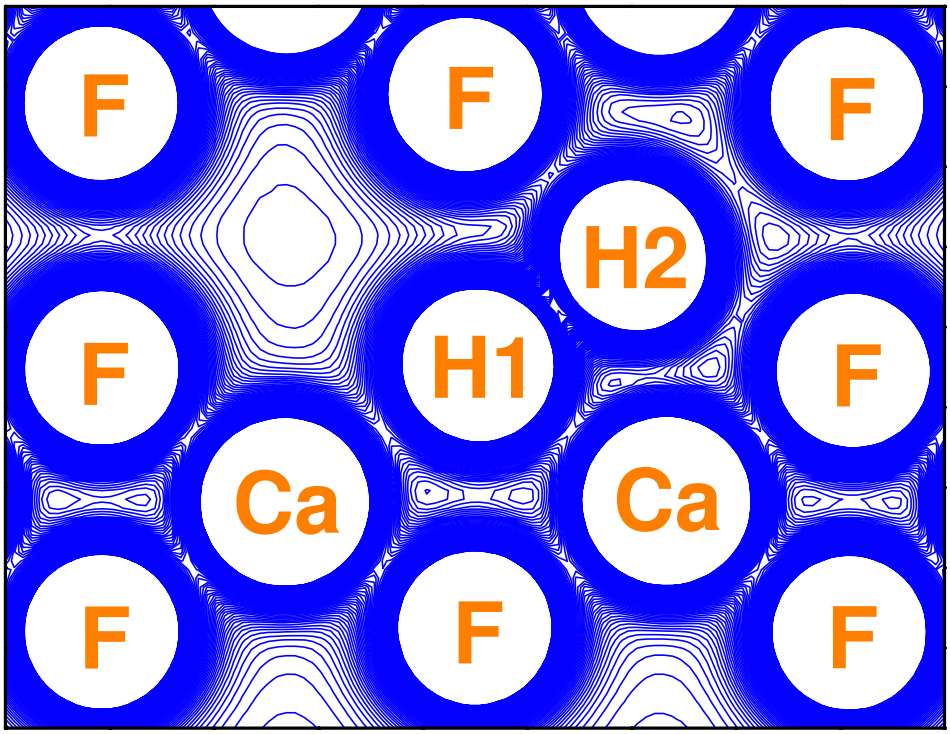

Figure 8.2: Charge density map of a CaF_2 crystal with the periodic H center from the (1 1 0) side view. Isodensity curves are drawn from 0 e/bohr^3 to 0.1 e/bohr^3 with an increment of 0.001 e/bohr^3.

Next, I calculated the band structures of the H center in CaF_2 and BaF_2 bulks. CaF_2 and BaF_2 with H centers exhibit optical absorption, centered around 4.03 eV and 3.76 eV, respectively [Beaumont *et al.* (1970)]. My results for defect levels (see Figure 8.4) allow to explain this experimentally observed optical absorption. In the one-electron approximation scheme, the experimentally observed optical absorption could be due to an electron transfer from the H-center ground state, to the empty band at β-spin induced by a hole localized on the H center (see Figure 8.4). The corresponding calculated values are 2.97 eV for CaF_2 and 2.93 eV for BaF_2, which are reasonable, however, are underestimated with respect to the experimental results.

The presence of an unpaired electron is also revealed by the band structure

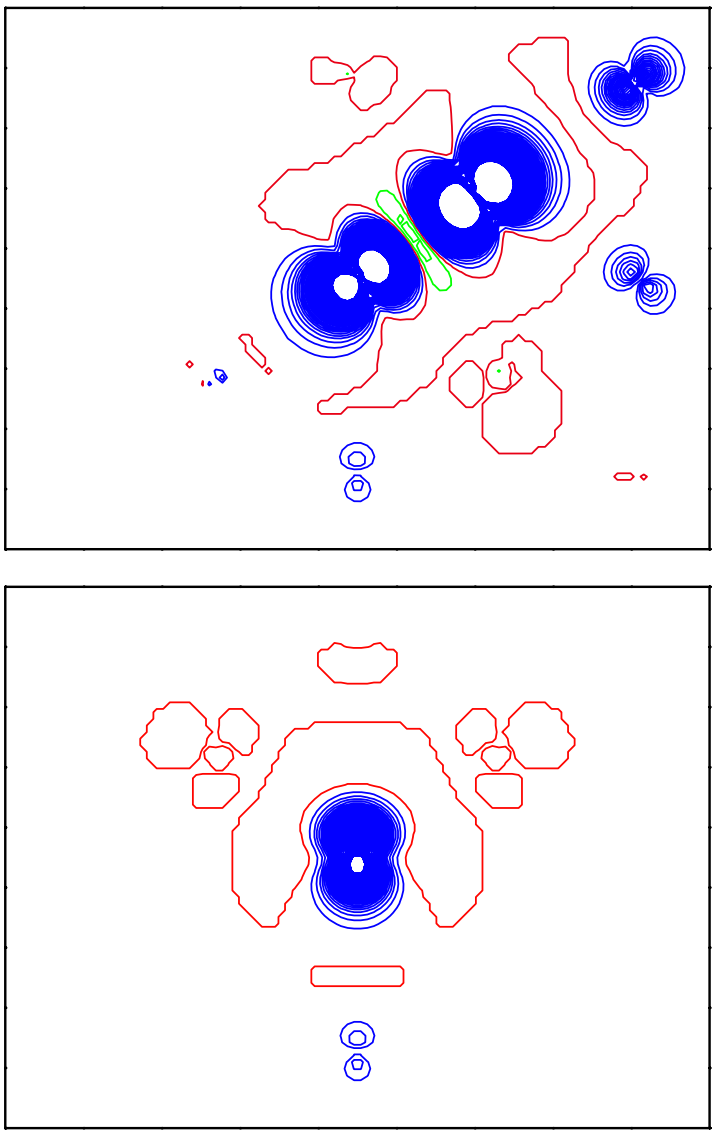

Figure 8.3: Spin density maps of a CaF_2 crystal with the periodic H center from the (1 1 0) (upper) and (1 -1 0) (lower) side views. Isodensity curves are drawn from -0.01 e/bohr^3 to 0.1 e/bohr^3 with an increment of 0.001 e/bohr^3. Blue, green and red lines denote positive, negative and zero values, respectively.

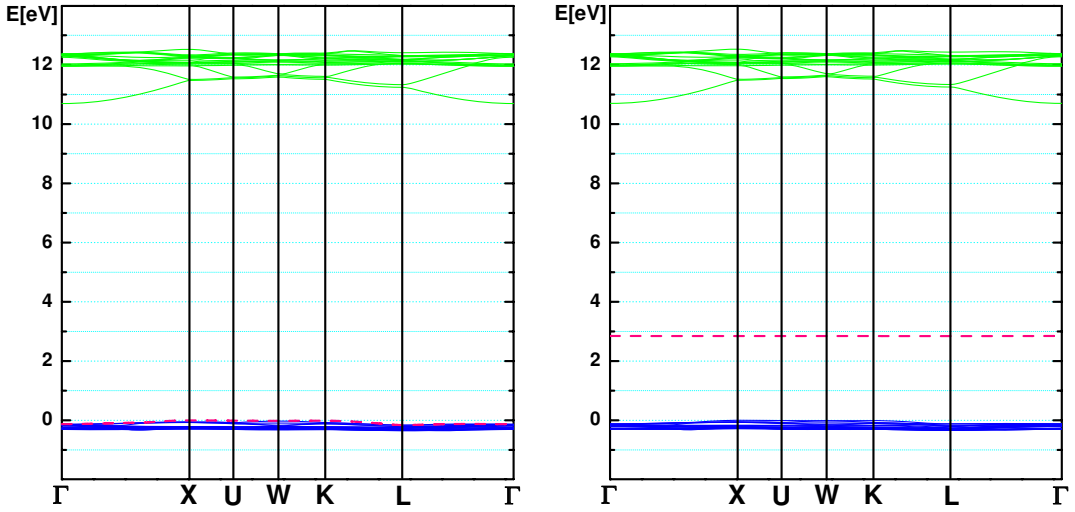

Figure 8.4: Calculated band structure for the 81-atom supercell modeling the H center in CaF_2. α (left) and β (right) denote the spin-up and spin-down states, respectively.

of the defective system given in Figure 8.4. Unlike the F-center case, the bound unpaired electron level labeled α band lies in the gap, but very closes to the top of VB, as we can see in the α-spin band structure in Figure 8.4. The empty level induced by a hole localized on the H center appears in the β-spin band 2.97 eV above the VB top. Because of the selection rules, the electron transition from the α occupied band to the β unoccupied band is forbidden. Therefore, optical absorption mentioned before could be due to an electron transfer from the β-VB top to the empty level, induced by a hole localized on the H center. The band

Table 8.3: Direct optical band gaps (eV) ($\Gamma \rightarrow \Gamma$) for H centers in CaF_2 and BaF_2 bulks.

	CaF_2		BaF_2	
Gaps	α	β	α	β
VB $\rightarrow$ H	—	2.97	—	2.93
VB $\rightarrow$ CB	10.83	10.82	11.11	11.10

gaps (distance between VB and CB) for the CaF_2 crystal containing H centers at Γ point are 10.83 eV and 10.82 eV for the α- and β-spin states, respectively, which are very close to each other and slightly reduced with respect to the band gap of the perfect CaF_2 crystal (10.96 eV). For the defective BaF_2 system, the band gaps between VB and CB at Γ point (11.11 eV for α and 11.10 eV for β) are also slightly smaller than the value in the perfect BaF_2 crystal (11.30 eV).

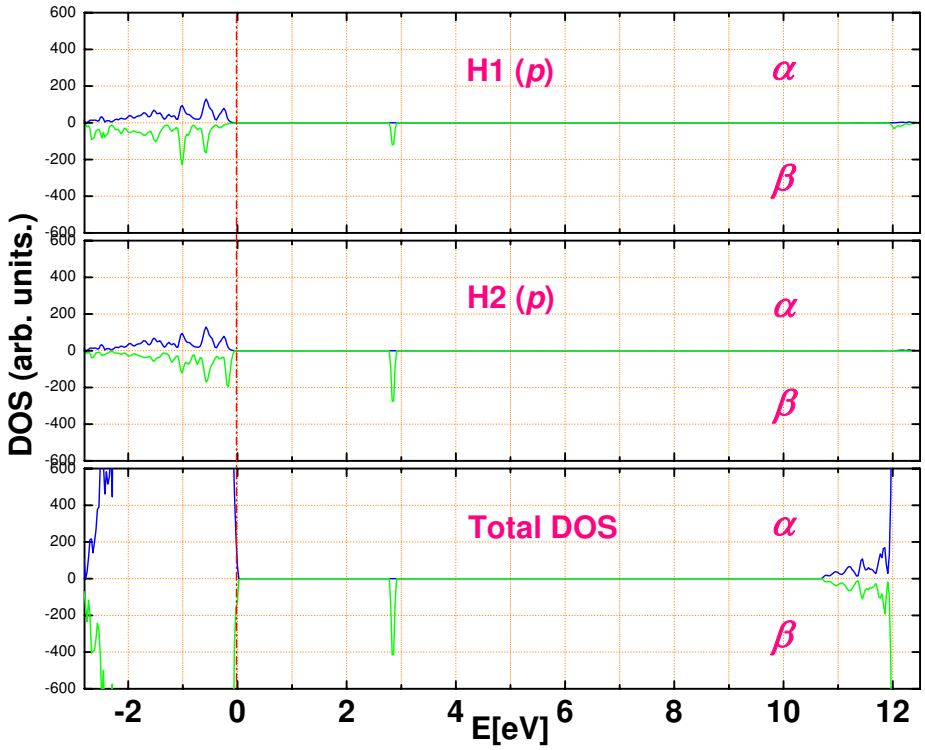

Figure 8.5: Total and projected density of states (DOS) for the H center in the CaF_2 bulk.

The total and partial density of states (DOS) of the H center in the CaF_2 bulk are displayed in Figure 8.5. The results of my calculations show that the H1 and H2 p-orbitals form the β band and the H2 does the major contribution. There are also some contributions from the H-center p-orbitals to the top of valence bands, as we can see from Figure 8.5. According to my previous work and current discussion, we can conclude that the F p-orbitals form the upper valence bands

and the β-spin defect level is mainly composed of H-center p-orbitals , whereas the CB bottom consists mainly of metal ion d-orbitials.

In comparison with other defects investigated before, the defect level induced by H centers in the α band structure is extremely close to the VB top. I suggest that it is due to this α defect level also consisting mainly of F p-orbitals, which form the VB top in both perfect and defective crystals. However, other kinds of defect bands, unlike the H-center case, are induced by other impurity species, such as *ghost* electrons, hydrogen atoms and oxygen atoms.

Conclusions

My calculations show that the creation of H centers in CaF_2 and BaF_2 crystals is accompanied with a stronger lattice relaxation around it, as I found previously for the F-center case. The results of my calculations show, that the H-center oriented in the (111) direction in CaF_2 and BaF_2 crystals is the energetically most favorable one, in agreement with experiment, and by 0.69 eV and 0.89 eV more favorable than the H-center orientation in the (100) direction. According to my calculations, the hole is mainly localized on the interstitial fluorine, in agreement with the experimental observations, and induces the empty level in the β-spin band gaps of CaF_2 and BaF_2 crystals, located 2.97 eV and 2.93 eV above the VB top, respectively. My calculations allow to explain theoretically an absorption band of the H center peaking at about 4.03 eV in CaF_2 and at about 3.76 eV in BaF_2 [Beaumont *et al.* (1970)].

Chapter 9

Conclusions

In this Thesis, I performed *ab initio* calculations to investigate the defect structures and optical properties of alkaline-earth fluorides, such as CaF_2 and BaF_2. The electronic structures of perfect crystals and slabs, F centers, M centers, oxygen and hydrogen impurities, and H centers were calculated. In order to obtain a good theoretical method for further calculations on defective systems, the bulk and electronic properties of CaF_2 and BaF_2 crystals have been calculated by seven different methods. The comparison of these seven types of Hamiltonians shows that the best agreement with the experimental results for the lattice constant, bulk modulus, as well as the band structure, is obtained by the hybrid technique (B3PW).

The calculations on perfect slabs show that the direct optical band gaps for CaF_2 and BaF_2 bulks are narrowed for the (111), (110) and (100) surfaces. The (111) surface energy is the smallest one among these three terminations, indicating that the (111) surface is the most stable one, in good agreement with the available experimental result. The relaxation of F atoms in the upper sublayer of the top (111) surface layer is inwards and is comparable with the LEED experimental results.

The data obtained in F-center DFT-B3PW calculations show that an unpaired electron is well localized inside the vacancy (V_F); the relaxation of atoms surrounding the F center is small; the creation of a neutral V_F in CaF_2 and BaF_2 results in a new F-center defect band located at the Γ point 6.75 eV and 7.01 eV, respectively, above the VB top. The β band absorption in alkaline-earth

fluorides is predominantly due to the presence of M centers. According to my calculations, the direct optical gap ($\Gamma \rightarrow \Gamma$) for M centers in CaF_2 is 2.22 eV, which is in good agreement with the experimental value of 2.38 eV, and much smaller than the corresponding value in the F-center case. The relevant optical gap in the BaF_2 M-center case is 1.38 eV and is also much smaller than in the F-center case. The formation energy for the (111) surface F center is smaller than in the bulk. The lower formation energy for a surface F center implicates the preference for F centers located near the surface.

The electronic structures of the OV dipoles in CaF_2 calculated using the hybrid B3PW method have been compared with the known experimental results and the theoretical work performed by Mysovsky *et al.* (2004). The optical absorption bands at the Γ point are in good agreement with the experimental value. Several configurations of the $(OV)_2$-dimer were calculated. The conclusion is a presence of the aggregation of OV dipoles and the association energy for the most favorable one is 0.55 eV.

In order to study the other kind of important doped atoms, hydrogen impurities, I performed the hybrid B3PW calculations. My calculated optical absorption energy for hydrogen impurities (H_s^- centers) is in qualitative agreement with the experimental results. I found, that the defect band induced by hydrogen atoms is much more close to the VB top than it was for the F-center case. The relaxation of the atoms around the hydrogen impurity in the bulk is very small, but the relaxation of surrounding atoms is not any more negligible for a hydrogen impurity located at surfaces. I also observed a strengthening of the surface H_s^- and M (metal ion) chemical bond. A similar effect, strengthening of the F center-metal ion bond populations near the surfaces, was also observed.

My calculations using the hybrid B3PW method on H centers show that the creation of H centers in CaF_2 and BaF_2 crystals is accompanied with a stronger lattice relaxation around it. The H-center oriented in the (111) direction in CaF_2 and BaF_2 crystals is the energetically most favorable one, in agreement with experiment. According to my calculations, the hole is mainly localized on the interstitial fluorine, fitting to the experimental observations, and induces empty level in the β-spin band gaps of CaF_2 and BaF_2 crystals, located 2.97 eV and 2.93 eV above the VB top, respectively.

Appendix A

Spin-restricted/unrestricted Hartree-Fock theory

A.1 The energy of a general polyelectronic system

For a N-electron system, the Hamiltonian (in atomic units $m = \hbar = e^2 = 1$) takes the following general form:

$$\mathscr{H} = \left(-\frac{1}{2}\sum_{i=1}^{N} \nabla_i^2 - \frac{1}{r_{1A}} - \frac{1}{r_{1B}} \cdots + \frac{1}{r_{12}} + \frac{1}{r_{13}} + \cdots \right) \tag{A.1}$$

where r is the distance between two charged particles (electron or nucleus). The nuclei are labeled using capital letters A, B, C, etc., and the electrons are labeled 1, 2, 3, $\cdots$.

Recall that a system of N electrons in N spin orbitals, χ_i, can be written as a Slater determinant (see Chapter 3). Each term in the determinant can thus be written $\chi_i(1)\chi_j(2)\chi_k(3)\cdots\chi_u(N-1)\chi_v(N)$, where i, j, k, ..., u, v is a series of N integers.

The energy can be calculated from:

$$\begin{aligned}\int \Psi \mathscr{H} \Psi \;\; = \;\; & \int \cdots \int d\tau_1 d\tau_2 \cdots d\tau_N \Bigg\{ [\chi_i(1)\chi_j(2)\chi_k(3)\cdots] \\ & \times \left(-\frac{1}{2}\sum_{i=1} \nabla_i^2 - (1/r_{1A}) - (1/r_{1B}) \cdots + (1/r_{12}) + (1/r_{13}) + \cdots \right) \\ & \times [\chi_i(1)\chi_j(2)\chi_k(3)\cdots] \Bigg\} \end{aligned} \tag{A.2}$$

It is more convenient to write the energy expression in a concise form that recognizes the three types of interaction that contribute to the total electronic energy of the system.

First, there is the kinetic and potential energy of each electron moving in the field of the nuclei. The energy associated with this contribution for the molecular orbital χ_i is often written H_{ii}^{core} and for M nuclei is given by:

$$H_{ii}^{\text{core}} = \int d\tau_1 \chi_i(1) \left(-\frac{1}{2}\nabla_i^2 - \sum_{A=1}^{M} \frac{\mathrm{Z}_A}{r_{iA}} \right) \chi_i(1) \tag{A.3}$$

For N electrons in N molecular orbitals, this contribution to the total energy is:

$$E_{\text{total}}^{\text{core}} = \sum_{i=1}^{N} \int d\tau_1 \chi_i(1) \left(-\frac{1}{2}\nabla_i^2 - \sum_{A=1}^{M} \frac{\mathrm{Z}_A}{r_{iA}} \right) \chi_i(1) = \sum_{i=1}^{N} H_{ii}^{\text{core}} \tag{A.4}$$

Here we have followed convention and have used the label $'1'$ wherever there is an integral involving the coordinates of a single electron, even though the actual electron may not be $'$electron 1$'$. Similarly, when it is necessary to consider two electrons then the labels 1 and 2 are conventionally employed. H_{ii}^{core} makes a favorable (i.e. negative) contribution to the electronic energy.

The second contribution to the energy arises from the electrostatic repulsion between pairs of electrons. This interaction depends on the electron-electron distance and, as we have seen, is calculated from integrals such as:

$$J_{ij} = \iint d\tau_1 d\tau_2 \chi_i(1)\chi_j(2) \left(\frac{1}{r_{12}} \right) \chi_i(1)\chi_j(2) \tag{A.5}$$

The symbol J_{ij} is often used to represent this Coulomb interaction between electrons in spin orbitals i and j, and is unfavorable (i.e. positive). The total Coulomb

contribution to the electronic energy of the system is obtained as a double summation over all electrons, taking care to count each interaction just once:

$$E_{\text{total}}^{\text{Coulomb}} = \sum_{i=1}^{N} \sum_{j=i+1}^{N} \int d\tau_1 d\tau_2 \chi_i(1)\chi_i(1) \frac{1}{r_{12}} \chi_j(2)\chi_j(2) = \sum_{i=1}^{N} \sum_{j=i+1}^{N} J_{ij} \qquad \text{(A.6)}$$

The third contribution to the energy is the exchange 'interaction'. This has no classical counterpart and arises because the motions of electrons with parallel spins are correlated: whereas there is a finite probability of finding two electrons with opposite (i.e. paired) spins at the same point in space, where the spins are the same then the probability is zero. This can be considered a manifestation of the Pauli principle, for if two electrons occupied the same region of space and had parallel spins then they could be considered to have the same set of quantum numbers. Electrons with the same spin thus tend to 'avoid' each other, and they experience a lower Coulombic repulsion, giving a lower (i.e more favorable) energy. The exchange interaction involves integrals of the form:

$$K_{ij} = \iint d\tau_1 d\tau_2 \chi_i(1)\chi_j(2) \left(\frac{1}{r_{12}}\right) \chi_i(2)\chi_j(1) \qquad \text{(A.7)}$$

This integral is only non-zero if the spins of the electrons in the spin orbitals χ_i and χ_j are the same. The energy due to exchange is often represented as K_{ij}. The total exchange energy is calculated thus:

$$E_{\text{total}}^{\text{exchange}} = \sum_{i=1}^{N} \sum_{j'=i+1}^{N} \int d\tau_1 d\tau_2 \chi_i(1)\chi_j(2) \frac{1}{r_{12}} \chi_i(2)\chi_j(1) = \sum_{i=1}^{N} \sum_{j'=i+1}^{N} K_{ij} \qquad \text{(A.8)}$$

The prime on the counter j' indicates that the summation is only over electrons with the same spin as electron i.

A.2 Closed-shell systems

A.2.1 The energy of a closed-shell system

In molecular modeling we are usually concerned with the ground states of molecules, most of which have closed-shell configurations. In a closed-shell system containing N electrons in $N/2$ orbitals, there are two spin orbitals associated with each

spatial orbital ψ_i: $\psi_i\alpha$ and $\psi_i\beta$. The electronic energy of such a system can be calculated in the following manner. First, there is the energy of each electron moving in the field of the bare nuclei. For an electron in a molecular orbital χ_i, this contributes an energy H_{ii}^{core}. If there are two electrons in the orbital then the energy is $2H_{ii}^{\text{core}}$ and for $N/2$ orbitals the total contribution to the energy will be: $\sum_{i=1}^{N/2} 2H_{ii}^{\text{core}}$.

If we consider the electron-electron terms, the interaction between each pair of orbitals ψ_i and ψ_j involves a total of four electrons. There are four ways in which two electrons in one orbital can interact in a Coulomb sense with two electrons in a second orbital, thus giving $4J_{ij}$. However, there are just two ways to obtain paired electrons from this arrangement, giving a total exchange contribution of -$2K_{ij}$. Finally, the Coulomb interaction between each pair of electrons in the same orbital must be included; there is no exchange interaction because the electrons have paired spins. The total energy is thus given as:

$$\begin{aligned} E &= 2\sum_{i=1}^{N/2} H_{ii}^{\text{core}} + \sum_{i=1}^{N/2}\sum_{j=i+1}^{N/2}(4J_{ij} - 2K_{ij}) + \sum_{i=1}^{N/2} J_{ii} \\ &= 2\sum_{i=1}^{N/2} H_{ii}^{\text{core}} + \sum_{i=1}^{N/2}\sum_{j=1}^{N/2}(2J_{ij} - K_{ij}) \end{aligned} \tag{A.9}$$

A.2.2 Linear combination of atomic orbitals (LCAO) in Hartree-Fock theory

Direct solution of the Hartree-Fock equations is not a practical proposition for molecules and so it is necessary to adopt an alternative approach. The most popular strategy is to write each spin orbital as a linear combination of single electron orbitals:

$$\psi_i = \sum_{\nu=1}^{K} c_{\nu i}\phi_\nu \tag{A.10}$$

The one-electron orbitals ϕ_ν are commonly called *basis functions* and often correspond to the atomic orbitals. In the case of Equation (A.10) there are K basis functions and we should therefore expect to derive a total of K molecular orbitals (although not all of these will necessarily be occupied by electrons). The smallest

number of basis functions for a molecular system will be that which can just accommodate all the electrons in the molecule. More sophisticated calculations use more basis functions than a minimal set. At the *Hartree-Fock limit* energy of the system can be reduced no further by the addition of any more basis functions; however, it may be possible to lower the energy below the Hartree-Fock limit by using a function form of the wave function that is more extensive than the single Slater determinant.

In accordance with the variation theorem we require the set of coefficients $c_{\nu i}$ that gives the lowest-energy wave function, and some scheme for changing the coefficients to derive that wave function. For a given basis set and a given functional form of the wave function (i.e. a Slater determinant) the best set of coefficients is that for which the energy is a minimum, at which point $\partial E/c_{\nu i} = 0$ for all coefficients $c_{\nu i}$. The objective is thus to determine the set of coefficients that gives the lowest energy for the system.

A.2.3 The Roothaan-Hall equations

The derivation of the Hartree-Fock equations for a closed-shell system was first proposed by Roothaan (1951) and (independently) by Hall (1951). The resulting equations are known as the Roothaan equations or the Roothaan-Hall equations. Unlike the integro-differential form of the Hartree-Fock equations, Roothaan and Hall recast the equations in matrix form, which can be solved using standard techniques and can be applied to systems of any geometry.

We now introduce the atomic orbital expansion for the orbitals ψ_i and substitute for the corresponding spin orbital χ_i into the Hartree-Fock equation, $\mathscr{F}_i(1)\chi_i(1) = \varepsilon_i\chi_i(1)$:

$$\mathscr{F}_i(1)\sum_{\nu=1}^{K} c_{\nu i}\phi_\nu(1) = \varepsilon_i \sum_{\nu=1}^{K} c_{\nu i}\phi_\nu(1) \tag{A.11}$$

Pre-multiplying each side by $\phi_\mu(1)$ (where ϕ_μ is also a basis function) and integrating gives the following matrix equation:

$$\sum_{\nu=1}^{K} c_{\nu i} \int d\upsilon_1 \phi_\mu(1)\mathscr{F}_i(1)\phi_\nu(1) = \varepsilon_i \sum_{\nu=1}^{K} c_{\nu i} \int d\upsilon_1 \phi_\mu(1)\phi_\nu(1) \tag{A.12}$$

$\int d\upsilon_1 \phi_\mu(1)\phi_\nu(1)$ is the overlap integral between the basis functions μ and ν, written $S_{\mu\nu}$. Unlike the molecular orbitals, which will be required to be orthonormal, the overlap between two basis functions is not necessarily zero (for example, they may be located on different atoms).

The elements of the *Fock matrix* are given by:

$$F_{\mu\nu} = \int d\upsilon_1 \phi_\mu(1) \mathscr{F}_i(1) \phi_\nu(1) \tag{A.13}$$

The elements of the Fock matrix can thus be written as the sum of core, Coulomb and exchange contributions. For a closed-shell system, the substitution of Equation (A.11) for $\mathscr{F}_i(1)$ leads the elements of the Fock matrix to be written as:

$$F_{\mu\nu} = H_{\mu\nu}^{\text{core}} + \sum_{\lambda=1}^{K}\sum_{\sigma=1}^{K} P_{\lambda\sigma}[(\mu\nu|\lambda\sigma) - \frac{1}{2}(\mu\lambda|\nu\sigma)] \tag{A.14}$$

$H_{\mu\nu}^{\text{core}}$ is the core contribution, the two terms in the summation are the Coulomb and exchange contributions, respectively. Where $\mathbf{P}$, the *charge density matrix*, whose elements are defined as:

$$P_{\lambda\sigma} = 2\sum_{i=1}^{N/2} c_{\lambda i} c_{\sigma i} \tag{A.15}$$

and the shorthand notation $(\mu\nu|\lambda\sigma)$ means:

$$(\mu\nu|\lambda\sigma) = \int d\upsilon_1 d\upsilon_2 \phi_\mu(1)\phi_\nu(1)\frac{1}{r_{12}}\phi_\lambda(2)\phi_\sigma(2) \tag{A.16}$$

Note that the summation of the P formula is over the $N/2$ occupied orbitals. Other properties can be calculated from the density matrix; for example, the electronic energy is:

$$E = \frac{1}{2}\sum_{\mu=1}^{K}\sum_{\nu=1}^{K} P_{\mu\nu}(H_{\mu\nu}^{\text{core}} + F_{\mu\nu}) \tag{A.17}$$

The electron density at a point $\mathbf{r}$ can also be expressed in terms of the density matrix:

$$\rho(\mathbf{r}) = \sum_{\mu=1}^{K}\sum_{\nu=1}^{K} P_{\mu\nu}\phi_\mu(\mathbf{r})\phi_\nu(\mathbf{r}) \tag{A.18}$$

Equation (A.14) is the standard form for the expression for the Fock matrix in the Roothaan-Hall equations.

Recall that a Hartree-Fock calculation provides a set of orbital energies, ε_i. The energy of an electron in a spin orbital is calculated by adding the core interaction H_{ii}^{core} to the Coulomb and exchange interactions with the other electrons in the system:

$$\varepsilon_i = H_{ii}^{\text{core}} + \sum_{j=1}^{N/2}(2J_{ij} - K_{ij}) \tag{A.19}$$

The total electronic energy of the ground state is given by Equation (A.9) and is therefore not equal to the sum of the individual orbital energies but is related as follows:

$$E = \sum_{i=1}^{N}\varepsilon_i - \sum_{i=1}^{N/2}\sum_{j=1}^{N/2}(2J_{ij} - K_{ij}) \tag{A.20}$$

The reason for the discrepancy is that the individual orbital energies include contributions from the interaction between that electron and all other electrons in the system. The Coulomb and exchange interactions between pairs of electrons are therefore counted twice when summing the individual orbital energies.

A.3 Open-shell systems

The Roothaan-Hall equations are not applicable to open-shell systems, which contain one or more unpaired electrons. Radicals are, by definition, open-shell systems as are some ground-state molecules such as NO and O_2. Two approaches have been devised to treat open-shell systems. The first of these is *spin-restricted* Hartree-Fock (RHF) theory, which uses combinations of singly and doubly occupied molecular orbitals. The closed-shell approach that we have developed thus far is a special case of RHF theory. The doubly occupied orbitals use the same spatial functions for electrons of both α and β spin. The orbital expansion Equation (A.10) is employed together with the variational method to derive the optimal value of the coefficients. The alternative approach is the *spin-unrestricted Hartree-Fock* (UHF) theory of Pople & Nesbet (1954), which uses two distinct sets of molecular orbitals: one for electrons of α spin and the other for electrons of β spin. Two Fock matrices are involved, one for each type of spin, with elements

as follows:

$$F_{\mu\nu}^{\alpha} = H_{\mu\nu}^{\text{core}} + \sum_{\lambda=1}^{K}\sum_{\sigma=1}^{K}[[P_{\lambda\sigma}^{\alpha} + P_{\lambda\sigma}^{\beta}](\mu\nu|\lambda\sigma) - P_{\lambda\sigma}^{\alpha}(\mu\lambda|\nu\sigma)]$$
$$F_{\mu\nu}^{\beta} = H_{\mu\nu}^{\text{core}} + \sum_{\lambda=1}^{K}\sum_{\sigma=1}^{K}[[P_{\lambda\sigma}^{\alpha} + P_{\lambda\sigma}^{\beta}](\mu\nu|\lambda\sigma) - P_{\lambda\sigma}^{\beta}(\mu\lambda|\nu\sigma)] \tag{A.21}$$

UHF theory also uses two density matrices, the full density matrix being the sum of these two:

$$P_{\mu\nu}^{\alpha} = \sum_{i=1}^{\alpha_{occ}} c_{\mu i}^{\alpha} c_{\nu i}^{\alpha} \qquad P_{\mu\nu}^{\beta} = \sum_{i=1}^{\beta_{occ}} c_{\mu i}^{\beta} c_{\nu i}^{\beta} \tag{A.22}$$

$$P_{\mu\nu} = P_{\mu\nu}^{\alpha} + P_{\mu\nu}^{\beta} \tag{A.23}$$

The summations in Equations (A.22) and (A.23) are over the occupied orbitals with α and β spin as appropriate. Thus, $\alpha_{\text{occ}} + \beta_{\text{occ}}$ equals the total number of electrons in the system. In a closed-shell Hartree-Fock wave function the distribution of electron spin is zero everywhere because the electrons are paired. In an open-shell system, however, there is an excess of electron spin, which can be expressed as the spin density, analogous to the electron density. The spin density $\rho^{\text{spin}}(\mathbf{r})$ at a point $\mathbf{r}$ is given by:

$$\rho^{\text{spin}}(\mathbf{r}) = \rho^{\alpha}(\mathbf{r}) - \rho^{\beta}(\mathbf{r}) = \sum_{\mu=1}^{K}\sum_{\nu=1}^{K}[P_{\mu\nu}^{\alpha} - P_{\mu\nu}^{\beta}]\phi_{\mu}(\mathbf{r})\phi_{\nu}(\mathbf{r}) \tag{A.24}$$

Clearly, the UHF approach is more general and indeed the RHF approach is a special case of UHF. Figure A.1 illustrates the conceptual difference between the RHF and the UHF models.

Following the previous calculations of the orbital energies for closed-shell systems, for a open-shell system that has p α-spin orbitals and q β-spin orbitals (and $p > q$), the energy of an electron in a spin orbital is given by:

$$\varepsilon_i^{\alpha(\beta)} = H_{ii}^{\alpha(\beta)} + \sum_{j=1}^{p(q)}(J_{ij} - K_{ij}^{\alpha(\beta)}) + \sum_{j=1}^{q(p)} J_{ij} \tag{A.25}$$

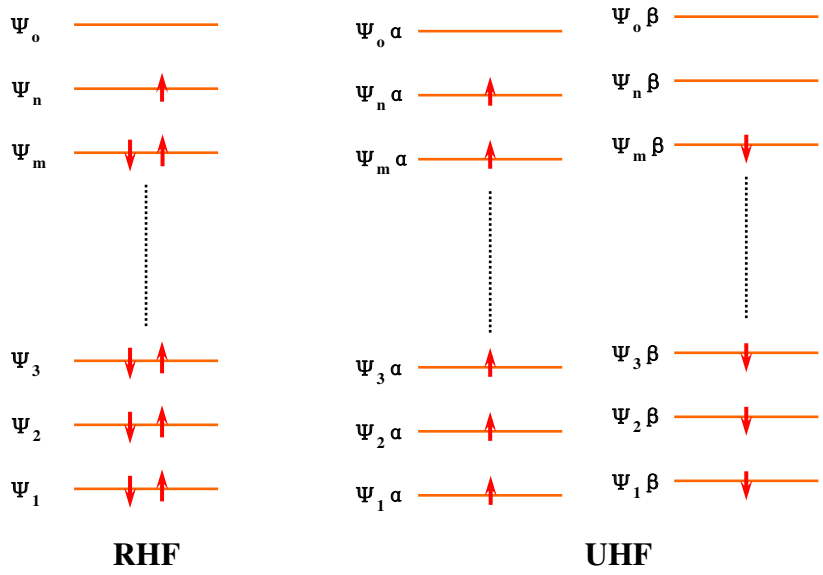

Figure A.1: The conceptual difference between the RHF and the UHF models.

Where, $K_{ij}^{\alpha(\beta)}$ indicate the exchange energies between the electrons that have the same spin. The total energy can then be expressed as:

$$E = \frac{1}{2}\sum_{i=1}^{p}(\varepsilon_i^{\alpha} + H_{ii}^{\alpha}) + \frac{1}{2}\sum_{i=1}^{q}(\varepsilon_i^{\beta} + H_{ii}^{\beta}) \tag{A.26}$$

A.4 A tentative explanation to polarized band structures

As mentioned in Chapter 5, there is a band-gap difference between α and β states. Here, I try to give a qualitative explanation in the HF scheme. The explanation should also be available in the DFT framework. The reason of the band-gap difference between α and β states is that there is more exchange energy for the α case due to the more number of the α-spin electrons.

Let's consider the F-center case as an example. The one-electron spin orbital energies in the valence band top (V), the F-center band ($F = V + 1$) and the conduction band bottom ($C = V + 2$) can be expressed as:

$$\begin{aligned}
\varepsilon_V^{\alpha} &= H_{VV}^{\alpha} + \sum_{j=1}^{V+1}(J_{Vj} - K_{Vj}^{\alpha}) + \sum_{j=1}^{V} J_{Vj} \\
\varepsilon_F^{\alpha} &= H_{FF}^{\alpha} + \sum_{j=1}^{V+1}(J_{Fj} - K_{Fj}^{\alpha}) + \sum_{j=1}^{V} J_{Fj} \\
\varepsilon_C^{\alpha} &= H_{CC}^{\alpha} + \sum_{j=1}^{V+1}(J_{Cj} - K_{Cj}^{\alpha}) + \sum_{j=1}^{V} J_{Cj}
\end{aligned} \tag{A.27}$$

$$\begin{aligned}
\varepsilon_V^{\beta} &= H_{VV}^{\beta} + \sum_{j=1}^{V}(J_{Vj} - K_{Vj}^{\beta}) + \sum_{j=1}^{V+1} J_{Vj} \\
\varepsilon_F^{\beta} &= H_{FF}^{\beta} + \sum_{j=1}^{V}(J_{Fj} - K_{Fj}^{\beta}) + \sum_{j=1}^{V+1} J_{Fj} \\
\varepsilon_C^{\beta} &= H_{CC}^{\beta} + \sum_{j=1}^{V}(J_{Cj} - K_{Cj}^{\beta}) + \sum_{j=1}^{V+1} J_{Cj}
\end{aligned} \tag{A.28}$$

Because there is an unpaired electron occupying the F-center band in the α-spin state, extra terms of $-K^{\alpha}_{V(C),V+1}$, the exchange interactions between the electron in the VB top orbital or the CB bottom orbital and the electron in the F-center band orbital, present in Equation (A.27). Therefore, the band-gap difference is mainly due to these extra exchange interactions. For the energies $\varepsilon_F^{\alpha(\beta)}$, since $-K^{\alpha}_{F,V+1}$, the extra exchange energy, is negative, the F-center band for α spin is lower than for β spin.

A. SPIN-RESTRICTED/UNRESTRICTED HARTREE-FOCK THEORY

Main Publications

- H. Shi, R.I. Eglitis and G. Borstel. *Ab initio calculations of the CaF_2 electronic structure and F centers.* Phys. Rev. B 72, 045109 (2005).
- R.I. Eglitis, H. Shi and G. Borstel. *First-principles calculations of the CaF_2 (111), (110) and (100) surface electronic and band structure.* Surface Review and Letters 13, 149 (2006).
- H. Shi, R.I. Eglitis and G. Borstel. *Ab initio calculations of the oxygen-vacancy dipoles and M centers in CaF_2.* Comput. Mat. Science, 2006 (accepted).
- H. Shi, R.I. Eglitis and G. Borstel. *Ab initio calculations of the BaF_2 bulk and surface F centers.* J. Phys. Condensed Matter 18, 8367 (2006).
- H. Shi, R.I. Eglitis and G. Borstel. *Ab initio calculations of the hydrogen centers in CaF_2 and BaF_2.* J. Phys. Condensed Matter 19, 056007 (2007).

A. SPIN-RESTRICTED/UNRESTRICTED HARTREE-FOCK THEORY

Acknowledgements

I would like to express my deep gratitude to my research supervisor Prof. Dr. Gunnar Borstel for many fruitful scientific discussions and his constant support in solving various administrative problems.

I am greatly indebted to Dr. Robert Eglitis for many his invaluable support, encouragement, and patience. Without his help this work would have never been done.

My special thanks are due to my colleague, Latvian friends, Oleg Sychev and Sergejs Piskunovs, for many explanations and helpful discussions in the beginning of my study.

I am indebted to Werner Nienhüser, who gave me a lot of helps for managing the computers in our group.

I am very thankful to my Chinese friends Ran Jia, Lun Yue, Huahai Tan, Dr. Yuchen Ma and Zhijun Yi for their essential moral support and scientific discussions, as well as I am much obliged to my Turkey friend Mehmet Kadiroglu for many useful and interesting communications.

Finally, I am very grateful to my parents for their omnifarious support during my Ph.D study.

A. SPIN-RESTRICTED/UNRESTRICTED HARTREE-FOCK THEORY

References

Adamo, C., Ernzerhof, M. & Scuseria, G.E. (2000). The meta-GGA functional: Thermochemistry with a kinetic energy density dependent exchnge-correlation functional. *Journal of Chemical Physics*, **112**, 2643. 15

Adler, H. & Kveta, I. (1957). *S.B. Österreich Akad. Wiss. Math.-Nature.* Klasse. Abt. II, **166**, 199. 11, 88

Archangelskaya, V.A., Reyterov, V.M. & Trofimova, L.M. (1980). *Zh. Prikl. Spektroskopii*, **32**, 103. 11, 95

Arends, J. (1964). Color centers in additively colored CaF_2 and BaF_2. *Physica Status Solidi*, **7**, 805–815. 8, 9, 67

Ayala, A.P. (2001). Atomicstic simulations of the pressure-induced phase transitions in BaF_2 crystals. *Journal of Physics: Condensed Matter*, **13**, 11741–11749. 4

Balik, C.M., Tripathy, S.K. & Hopfinger, A.J. (1982). Epitaxial morphologies of polyoxymethylene .I. electron-microscopy. *Journal of Polymer Science Part B: Polymer Physics*, **20**, 2003–2016. 59

Barth, J., Johnson, R.L., Cardona, M., Fuchs, D. & Bradshaw, A.M. (1990). Dielectric function of CaF_2 between 10 and 35 eV. *Physical Review*, **B 41**, 3291–3294. 3

Bartram, R.H., Harmer, A.L. & Hayes, W. (1971). Theory of F centres in alkaline earth fluorides. *Journal of Physics Part C: Solid State Physics*, **4**, 1665. 73, 74

Beaumont, J.H., Hayes, W., Kirk, D.L. & Summers, G.P. (1970). An investigation of trapped holes and trapped excitons in alkaline earth fluorides. *Proceedings of the Royal Society of London Series A: Mathematical and Physical Sciences*, **315**, 69. 9, 10, 109, 127, 128, 132

Becke, A.D. (1988a). Correlation energy of an inhomogeneous electron gas: A coordinate-space model. *Journal of Chemical Physics*, **88**, 1053. 8, 31

Becke, A.D. (1988b). Density-functional exhange-energy approximation with correct asymptotic behaviour. *Physical Review*, **A 38**, 3098–3100. 33, 36

Becke, A.D. (1992). Density-functional thermochemistry. i. the effect of the exchange-only gradient correction. *Journal of Chemical Physics*, **96**, 2155–2160. 31

Becke, A.D. (1993a). Density-functional thermochemistry. III. the role of exact exchange. *Journal of Chemical Physics*, **98**, 5648–5652. 32, 36

Becke, A.D. (1993b). A new mixing of hartree-fock and local density-functional theories. *Journal of Chemical Physics*, **98**, 1372–1377. 15, 32

Bennewitz, R., Smith, D. & Reichling, M. (1999). Bulk and surface processes in low-energy-electron-induced decomposition of CaF_2. *Physical Review*, **B 59**, 8237. 3

Bessent, R.G., Hayes, W. & Hodby, J.W. (1967). Paramagnetic resonance and electron nuclear double resonance of substitutional hydrogen atoms in CaF_2. *Proceedings of the Royal Society of London Series A: Mathematical and Physical Sciences*, **297**, 376. 11

Bessent, R.G., Hayes, W. & Smith, J.W.H.P.H.S. (1969). An investigation of effects of X-rays on undoped and on hydrogen doped alkaline earth fluorides. *Proceedings of the Royal Society of London Series A: Mathematical and Physical Sciences*, **309**, 69. 11, 118

Bill, H. & Lacroix, R. (1966). Preliminary results on a centre in CaF_2 crystals. *Physics Letters*, **21**, 257. 11

Bochicchio, R.C. & Reale, H.F. (1993). On the nature of crystalline bonding: Extension of statistical population analysis to 2-dimensional and 3-dimensional crystalline systems. *Journal of Physics B: Atomic Molecular and Optical Physics*, **26**, 4871–4883. 39

Bontinck, W. (1958a). Colour centers in synthetic fluorite crystals. *Physica*, **24**, 639–649. 11

Bontinck, W. (1958b). The hydrolysis of solid CaF_2. *Physica*, **24**, 650–658. 10, 11, 88

Bottin, F., Finocchi, F. & Noguera, C. (2003). Stability and electronic structure of the (1×1) $SrTiO_3$ (110) polar surfaces by first-principles calculations. *Physical Review*, **B 68**, 035418. 37

Bruch, H., Görlich, P., Karras, H. & Lehmann, R. (1964). Zur diffusion von gasen in hochreine CaF_2-kristalle und SrF_2-kristalle. *Physica Status Solidi*, **4**, 685–696. 11

Burke, J.P.P.K. & Ernzerhof, M. (1996). Generalized gradient approximation made simple. *Physical Review Letters*, **77**, 3865. 36

Burnett, J.H., Levine, Z.H. & Shirley, E.L. (2001). Intrinsic birefringence in calcium fluoride and barium fluoride. *Physical Review*, **B 64**, 241102. 4

Carrasco, J., Gomes, J.R.B. & Illas, F. (2004). Theoretical study of bulk and surface oxygen and aluminum vacancies in alpha-Al_2O_3. *Physical Review*, **B 69**, 064116. 80

Catlow, C.R.A. & Stoneham, A.M. (1983). Ionicity in solids. *Journal of Physics C: Solid State Physics*, **16**, 4321–4338. 39

Catlow, C.R.A., Comins, J.D., Germano, F.A., Harley, R.T. & Hayes, W. (1978). Brillouin-scattering and theoretical studies of high-temperature disorder in fluorite crystals. *Journal of Physics C: Solid State Physics*, **11**, 3197–3212. 17

Catti, M., Dovesi, R., Pavese, A. & Saunders, V.R. (1991). Elastic-constants and electronic-structure of fluorite (CaF_2) - an *ab initio* Hartree-Fock study. *Journal of Physics: Condensed Matter*, **3**, 4151–4164. 3, 7, 36, 43

Causa, M. & Zupan, A. (1994). Density-functional LCAO calculation of periodic-systems: A-posteriori correction of the hartree-fock energy of covalent and ionic-crystals. *Chemical Physics Letters*, **220**, 145–153. 36

Cavenett, B.C., Hayes, W., Hunter, I.C. & Stoneham, A.M. (1969). Magneto optical properties of F centres in alkaline earth. *Proceedings of the Royal Society of London Series A: Mathematical and Physical Sciences*, **309**, 53. 9

Ceperley, D.M. & Alder, B.J. (1980). Ground state of the electron gas by a stochastic method. *Physical Review Letters*, **45**, 566–569. 30

Ching, W.Y., GAN, F.Q. & Huang, M.Z. (1995). Band theory of linear and nonlinear susceptibilities of some binary ionic insulators. *Physical Review*, **B 52**, 1596–1611. 3, 17

Curtiss, L.A., Raghavachari, K., Redfern, P.C. & Pople, J.A. (1997). Assessment of gaussian-2 and density functional theories for the computation of entalpies of formation. *Journal of Chemical Physics*, **106**, 1063. 15

Curtiss, L.A., Redfern, P.C., Raghavachari, K. & Pople, J.A. (1998). Assessment of gaussian-2 and density functional theories for the computation of ionization potentials and electron affinities. *Journal of Chemical Physics*, **109**, 42. 15

de Leeuw, N.H. & Cooper, T.G. (2003). A computational study of the surface structure and reactivity of calcium fluoride. *Journal of Materials Chemistry*, **13**, 93–101. 3

de Leeuw, N.H., Purton, J.A., Parker, S.C., Watson, G.W. & Kresse, G. (2000). Density functional theory calculations of adsorption of water at calcium oxide and calcium fluoride surfaces. *Surface Science*, **452**, 9–19. 3

den Hartog, H.W. & Arends, J. (1967). *F*-centers in SrF_2. *Physica Status Solidi*, **22**, 131. 9

Dirac, P.A.M. (1930). Exchange phenomena in the Thomas atom. *Proc. Camb. Phil. Soc.*, **26**, 376. 29, 36

Dovesi, R., Ermondi, C., Ferrero, E., Pisani, C. & Roetti, C. (1984). Hartree-fock study of lithium hydride with the use of a polarizable basis set. *Physical Review*, **B 29**, 3591–3600. 104

Eglitis, R.I., Piskunov, S., Heifets, E., Kotomin, E.A. & Borstel, G. (2004). Ab initio study of the $SrTiO_3$, $BaTiO_3$ and $PbTiO_3$ (001) surfaces. *Ceramics International*, **30**, 1989–1992. 36, 37, 55, 103

El'kin, F.S., Tsiok, O.B., Khvostantsev, L.G. & Brazhkin, V.V. (2005). Precise in situ study of the kinetics of pressure-induced phase transition in CaF_2 including initial transformation stages. *Journal of Experimental and Theoretical Physics*, **100**, 971–976. 4

Elliott, R.J., HAYES, W., Jones, G.D. & Sennett, H.F.M.C.T. (1965). Localized vibrations of H^- and D^- ions in alkaline earth fluorides. *Proceedings of the Royal Society of London Series A: Mathematical and Physical Sciences*, **289**, 1. 10

Evarestov, R.A., Murin, I.V. & Petrov, A.V. (1989). Electronic-structure of fluorite-type crystals. *Journal of Physics: Condensed Matter*, **1**, 6603–6609. 43

Feltham, P. (1967). *F*-centres in alkaline earth fluorides. *Physica Status Solidi*, **20**, 675. 9

Feltham, P. & Andrews, J. (1965). Colour centres in alkaline earth fluorides. *Physica Status Solidi*, **10**, 203. 11

Fermi, E. (1928). A statistical method for the determination of some atomic properties and the application of this method to the theory of the periodic system of elements. *Z. Phys.*, **48**, 73. 29

Foster, A.S., Barth, C., Shluger, A.L., Nieminen, R.M. & Reichling, M. (2002). Role of tip structure and surface relaxation in atomic resolution dynamic force microscopy: CaF_2(111) as a reference surface. *Physical Review*, **B 66**, 235417. 3

Gan, F.Q., Xu, Y.N., Huang, M.Z., Ching, W.Y. & Harrison, J.G. (1992). Optical-properties of a CaF_2 crystal. *Physical Review*, **B 45**, 8248–8255. 3, 8

Gerward, L., Olsen, J.S., Steenstrup, S., Malinowski, M., Asbrink, S. & Waskowska, A. (1992). X-ray-diffraction investigations of CaF_2 at high-pressure. *Journal of Applied Crystallography*, **25**, 578–581. 4, 17

Gilman, J.J. (1960). Direct measurements of the surface energies of crystals. *Journal of Applied Physics*, **31**, 2208–2218. xiv, 12, 58, 59

Gunnarsson, O. & Lundqvist, B.I. (1976). Exchange and correlation in atoms, molecules, and solids by the spin-density-functional formalism. *Physical Review*, **B 13**, 4274–4298. 30

Hall, G.G. (1951). The molecular orbital theory of chemical valency viii. a method for calculating ionisation potentials. *Proceedings of the Royal Society (London)*, **A205**, 541–552. 139

Hall, J.L. & Schumacher, R.T. (1962). Electron spin resonance of hydrogen atoms in CaF_2. *Physical Review*, **127**, 1892. 10, 118

Hall, T.P.P., Leggeat, A. & Twidell, J.W. (1969). Structure of some trapped hole centres in CaF_2 .I. *Journal of Physics C: Solid State Physics*, **2**, 1590. 9, 127

Hay, P.J. & Wadt, W.R. (1985). Ab initio effective core potentials for molecular calculations: Potentials for K to Au including the outermost core orbitals. *Journal of Chemical Physics*, **82**, 299–310. 36

Hayes, W. (1974). *CRYSTALS WITH THE FLUORITE STRUCTURE - ELECTRONIC, VIBRATIONAL, AND DEFECT PROPERTIES*. CLARENDON PRESS, OXFORD. 7, 9, 12, 74, 77, 79, 104, 124

Hayes, W. & Stoneham, A.M. (1985). *Defects and Defect Processes in Nonmetallic Solids*. John Wiley & Sons, New York. 9

Hayes, W. & Stott, J.P. (1967). Electron nuclear double resonance of F centre in CaF_2. *Proceedings of the Royal Society of London Series A: Mathematical and Physical Sciences*, **301**, 313. 9

Hayes, W. & Twidell, J.W. (1962). Self-trapped hole in CaF_2. *Proceedings of the Royal Society of London*, **79**, 1295. 9

Hayes, W., Lambourn, R.F. & Stott, J.P. (1974). H centers in alkaline-earth fluorides. *Journal of Physics C: Solid State Physics*, **7**, 2429–2433. 10

Heifets, E., Eglitis, R.I., Kotomin, E.A., Maier, J. & Borstel, G. (2001). Ab initio modeling of surface structure for $SrTiO_3$(100) perovskite crystals. *Physical Review*, **B 64**, 235417. 53, 55, 103

Heifets, E., Eglitis, R.I., Kotomin, E.A., Maier, J. & Borstel, G. (2002). First-principles calculations for $SrTiO_3$(100) surface structure. *Surface Science*, **513**, 211–220. 15, 55

Ho, P.S. & Ruoff, A.L. (1967). Pressure dependence of elastic constants and an experimental equation of state for CaF_2. *Physical Review*, **161**, 864. 17

Hofmann, C. (1992). *Mater. Design*, **13**, 167. 12

Hohenberg, P. & Kohn, W. (1964). Inhomogeneous electron gas. *Physical Review*, **B 136**, 864–871. 25

Huisinga, M., Puchin, V.E. & Reichling, M. (1998). Photoemission from pure and electron irradiated CaF_2. *Nuclear Instruments & Methods in Physics Research Section B: Beam Interactions with Materials and Atoms*, **141**, 528–532. 12

Jiang, H.T., Pandey, R., Darrigan, C. & Rerat, M. (2003). First-principles study of structural, electronic and optical properties of BaF_2 in its cubic, orthorhombic and hexagonal phases. *Journal of Physics: Condensed Matter*, **15**, 709–718. 8, 17

Jockisch, A., Schroder, U., Dewette, F.W. & Kress, W. (1993). Relaxation and dynamics of the (111) surfaces of the fluorides CaF_2 and SrF_2. *Journal of Physics: Condensed Matter*, **5**, 5401–5410. 3, 14

Jones, R.O. & Gunnarsson, O. (1989). The density functional formalism, its applications and prospects. *Reviews of Modern Physics*, **61**, 689–746. 68

Kanchana, V., Valtheeswaran, G. & Rajagopalan, M. (2003a). Pressure induced structural phase transitions and metallization of BaF_2. *Journal of Alloys and Compounds*, **359**, 66–72. 17

Kanchana, V., Valtheeswaran, G. & Rajagopalan, M. (2003b). Structural phase stability of CaF_2 and SrF_2 under pressure. *Physica B: Condensed Matter*, **328**, 283–290. 4, 17

Katrusiak, A. & Nelmes, R.J. (1986). A test of the accuracy of high-pressure measurements using a merrill-bassett diamond-anvil cell. *Journal of Applied Crystallography*, **19**, 73–76. 17

Kawano, K., Ohya, T., Tsurumi, T., Katoh, K. & Nakata, R. (1999). X-ray excitation fluorescence spectra of the Eu^{2+}-stabilized V_k center in alkaline-earth fluoride mixed-crystal systems. *Physical Review*, **B 60**, 11984–11992. 3

Kazumata, Y. (1969). Esr of neutron-irradiated BaF_2 crystals. *Physica Status Solidi*, **34**, 377. 9

Khenata, R., Daoudi, B., Sahnoun, M., Baltache, H., Rerat, M., Reshak, A.H., Bouhafs, B., Abid, H. & Driz, M. (2005). Structural, electronic and optical properties of fluorite-type compounds. *European Physical Journal*, **B 47**, 63–70. 4, 8, 17, 43

Kohn, W. & Sham, L.J. (1965). Self-consistent equations including exchange and correlation effects. *Physical Review*, **A 140**, 1133–1138. 26

Langreth, D.C. & Perdew, J.P. (1980). Theory of nonuniform electronic systems. i. analysis of the gradient approximation and a generalization that works. *Physical Review*, **B 21**, 5469. 31

Leach, A.R. (2001). *Molecular Modelling: Principles and Applications*. PEARSON Prentice Hall, 2nd edn. 20

Lee, C., Yang, W. & Parr, R.G. (1988). Development of the colle-salvetti correlation energy formula into a functional of the electron density. *Physical Review*, **B 37**, 785–789. 31, 33, 36

Leger, J.M., Haines, J., Atouf, A. & Schulte, O. (1995). High-pressure x-ray-diffraction and neutron-diffraction studies of BaF_2 - An example of a coordination-number of 11 in AX_2 compounds. *Physical Review*, **B 52**, 13247–13256. 4, 17, 38

Letz, M. & Parthier, L. (2006). Charge centers in CaF_2: Ab initio calculation of elementary physical properties. *Physical Review*, **B 74**, 064116. 3

Levine, Z.H., Burnett, J.H. & Shirley, E.L. (2003). Photoelastic and elastic properties of the fluorite structure materials, LiF, and Si. *Physical Review*, **B 68**, 155120. 17

Lide, D.R. (1991). *Handbook of Chemistry and Physics*. CRC Press, Boston, 72nd edn. 72

Mattila, T., Pöykkö, S. & Nieminen, R.M. (1997). Ab initio study of point defects in CdF_2. *Physical Review*, **B 56**, 15665–15671. 62

Merawa, M., Llunell, M., Orlando, R., Gelize-Duvignau, M. & Dovesi, R. (2003). Structural, electronic and elastic properties of some fluoride crystals: an *ab initio* study. *Chemical Physics Letters*, **368**, 7–11. 4, 17

Messier, D.R. (1968). Kinetics of hydrolysis of single crystal CaF_2 from 1000 to 1120 °C. *Journal of the Electrochemical Society*, **115**, 397. 11, 88

Monkhorst, H.J. & Pack, J.D. (1976). Special points for Brillouin-zone integrations. *Physical Review*, **B 13**, 5188–5192. 61, 87, 104, 123

Muscat, J., Wander, A. & Harrison, N.M. (2001). On the prediction of band gaps from hybrid functional theory. *Chemical Physics Letters*, **342**, 397–401. 42, 43

Mysovsky, A.S., Radzhabov, E.A., Reichling, M., Shluger, A.L. & Sushko, P.V. (2004). Optical properties and transformation mechanism of oxygen centres and their aggregates in CaF_2 crystals. *Physica Status Solidi*. 11, 88, 90, 95, 96, 97, 134

Nepomnyashchikh, I., Radzhabov, E.A., Egranov, A.V., Ivashechkin, V.F. & Istomin, A.S. (2002). Defect formation and vuv luminescence in BaF_2. *Radiation Effects and Defects in Solids*, **157**, 715–719. 9, 67

Nicolav, M. (2000). *J. Cryst. Growth*, **218**, 62. 38

Noguera, C. (2000). Polar oxide surfaces. *Journal of Physics: Condensed Matter*, **12**, R367–R410. 37

Padilla, J. & Vanderbilt, D. (1997). Ab initio study of $BaTiO_3$ surfaces. *Physical Review*, **B 56**, 1625–1631. 55

Padilla, J. & Vanderbilt, D. (1998). Ab initio study of $SrTiO_3$ surfaces. *Surface Science*, **418**, 64–70. 55

Park, C.H. & Chadi, D.J. (2000). Effect of Interstitial Hydrogen Impurities on Ferroelectric Polarization in $PbTiO_3$. *Physical Review Letters*, **84**, 4717. 104

Parr, P.G. (1983). Density functional theory. *Annual Review of Physical Chemistry*, **34**, 631–656. 25

Pendas, A.M., Recio, J.M., Florez, M., Luana, V. & Bermejo, M. (1994). Static simulations of CaF_2 polymorphs. *Physical Review*, **B 49**, 5858–5868. 4, 17

Perdew, J.P. & Wang, Y. (1986). Accurate and simple density functional for the electronic exchange energy: Generalized gradient approximation. *Physical Review*, **B 33**, 8800. 31, 36

Perdew, J.P. & Wang, Y. (1992). Accurate and simple analytic representation of the electronic-gas correlation energy. *Physical Review*, **B 45**, 13244. 8, 31, 33, 36

Perdew, J.P. & Zunger, A. (1981). Self-interaction correction to density-functional approximations for many-electron systems. *Physical Review*, **B 23**, 5048–5079. 30

Pisani, C. (1996). Ouantum-Mechanical Ab initio Calculations of the Properties of Crystalline Materials, Lecture Notes in Chemistry, Vol.67 (Springer, Berlin). 37, 42, 123

Piskunov, S., Heifets, E., Eglitis, R.I. & Borstel, G. (2004). Bulk properties and electronic structure of $SrTiO_3$, $BaTiO_3$, $PbTiO_3$ perovskites: an ab initio HF/DFT study. *Computational Materials Science*, **29**, 165–178. 36, 37, 103

Pojani, A., Finocchi, F. & Noguera, C. (1999). Polarity on the $SrTiO_3$ (111) and (110) surfaces. *Surface Science*, **442**, 179–198. 37

Pople, J.A. & Nesbet, R.K. (1954). Self-consistent orbitals for radicals. *Journal of Chemical Physics*, **22**, 571–572. 28, 141

Puchin, V.E., Puchina, A.V., Huisinga, M. & Reichling, M. (2001). Theoretical modelling of steps on the CaF_2(111) surface. *Journal of Physics: Condensed Matter*, **13**, 2081–2094. 4, 12, 14, 46, 58

Puchina, A.V., Puchin, V.E., Kotomin, E.A. & Reichling, M. (1998). *Ab initio* study of the *F* centers in CaF_2: Calculations of the optical absorption, diffusion and binding energies. *Solid State Communications*, **106**, 285–288. 4, 9

Radzhabov, E. & Figura, P. (1986). Optical-properties of oxygen-vacancy centers in fluorite. *Physica Status Solidi B: Basic Research*, **136**, K55–K59. 11, 95

Reichling, M. (1998). Laser ablation in optical components and thin films. *Experimental Methods in the Physical Sciences*, **30**, 573. 12

Reichling, M., Sils, J., Johansen, H. & Matthias, E. (1999). *Appl. Phys. Suppl.*, **A 69**, S743. 12

Roothaan, C.C.J. (1951). New developments in molecular orbital theory. *Reviews of Modern Physics*, **23**, 69–89. 23, 139

Rubloff, G.W. (1972). Far ultraviolet reflectance spectra and electronic-structure of ionic-crystals. *Physical Review*, **B 5**, 662. vii, xiii, 4, 6, 7, 8, 40, 42, 43

Sata, N., Eberman, K., Eberl, K. & Maier, J. (2000). Mesoscopic fast ion conduction in nanometre-scale planar heterostructures. *Nature*, **408**, 946–949. 3

Saunders, V.R., Dovesi, R., Roetti, C., Causa, M., Harrison, N.M., Orland, R. & Zicovich-Wilson, C.M. (2003). *CRYSTAL-2003 User Manual*. University of Torino, Italy. 36, 70, 87

Schmalzl, K., Strauch, D. & Schober, H. (2003). Lattice-dynamical and ground-state properties of caf$_2$ studied by inelastic neutron scattering and density-functional methods. *Physical Review*, **B 68**, 144301. 4

Seifert, K.F. (1966). Strukturumwandlungen von halogeniden des typus ax2 unter hoheren drucken. *BERICHTE DER BUNSEN-GESELLSCHAFT FUR PHYSIKALISCHE CHEMIE*, **70**, 1041. 4

Slater, J.C. (1974). *Quantum Theory of Molecules and Solids Volume 4: The Self-consistent Field for Molecules and Solids*. McGraw-Hill, New York. 30

Speziale, S. & Duffy, T.S. (2002). Single-crystal elastic constants of fluorite (CaF_2) to 9.3 GPa. *Physics and Chemistry of Minerals*, **29**, 465–472. 4, 17

Stankievicz, B. & Kisiel, W. (1994). Influence of fluorine desorption on electronic-structure of CaF_2-LCAO slab calculations. *Vacuum*, **45**, 209–210. 14

Stankiewicz, B. & Modrak, P. (1995). Surface electronic-structure calculation of CaF_2. *Surface Science*, **333**, 1441–1445. 14

Starostin, N.V. (1969). Zone structure of fluoride-type crystals. *Soviet Physics Solid State*, **11**, 1317. 6

Stoneham, A.M., Hayes, W., Smith, P.H.S. & Stott, J.P. (1968). Hyperfine interactions of F centres in alkaline earth fluorides. *Proceedings of the Royal Society of London Series A: Mathematical and Physical Sciences*, **306**, 369. 9, 73, 74

Tasker, P.W. (1979). Stability of ionic-crystal surfaces. *Journal of Physics C: Solid State Physics*, **12**, 4977–4984. 37

Tasker, P.W. (1980). *J. Physique Coll.*, **41**, C6 488. 14

Taurian, O.E. & Kai, A.H.T. (1987). Calculation of optical-absorption energies and hyperfine interactions of F-centers in alkaline-earth fluorides. *Journal of Physics and Chemistry of Solids*, **48**, 513–516. 9

Thomas, L.H. (1927). The calculation of atomic fields. *Proc. Camb. Phil. Soc.*, **23**, 542. 29

Togawa, S. (1964). Experimental study on x-ray scattering factors of calcium fluoride. *Journal of the Physical Society of Japan*, **19**, 1696. 6

Tzalmona, A. & Pershan, P.S. (1969). Irradiation damage in SrF_2 and BaF_2. *Physical Review*, **182**, 906. 9

Verstraete, M. & Gonze, X. (2003). First-principles calculation of the electronic, dielectric, and dynamical properties of caf_2. *Physical Review*, **B 68**, 195123. 4, 8

Vogt, J., Henning, J. & Weiss, H. (2005). The structure of $CaF_2(111)$ and $BaF_2(111)$ single crystal surfaces: A tensor low energy electron diffraction study. *Surface Science*, **578**, 57–70. 14, 46, 48

Vosko, S.H., Wilk, L. & Nusair, M. (1980). Accurate spin-dependent electron liquid correlation energies for local spin density calculations: A critical analysis. *Canadian Journal of Physics*, **58**, 1200–1211. 30, 36

Warren, B.E. (1961). Anomalous temperature behavior of 200 reflection of fluorite. *Acta Crystallographica*, **14**, 1095. 6

Weast, R.C. (1976). *CRC Handbook of Chemistry and Physics*. CRC Press, Boca Raton. 38

Weil, J.A., Bolton, J.R. & Wertz, J.E. (1994). *Electron Paramagnetic Resonance*. Wiley, New York. 72

Weiss, A., Witte, H. & Wölfel, E. (1957). *Z. Phys. Chem.*, **10**, 98. 6

Westin, E., Rosén, A. & Matthias, E. (1990). Molecular cluster calculations of the electronic structure of the (111) surface of CaF_2. *Springer Series in Surface Science*, **19**, p 316. 14

Wickersheim, K.A. & Hanking, B.M. (1959). Infrared absorption in calcium fluoride. *Physica*, **25**, 569–570. 10

Wimmer, E. (1997). *Electronic Structure Methods*. NATO ASI Series C498, Dordrecht, Kluwer. 25

Wu, X., Wu, Z.Y., Guo, L., Liu, C.M., Liu, J., Li, X.D. & Xu, H.B. (2005). Pressure-induced phase transformation in controlled shape ZnO nanorods. *Solid State Communications*, **135**, 780–784. 17

Wu, X., Qin, S. & Wu, Z.Y. (2006). First-principles study of structural stabilities, and electronic and optical properties of CaF_2 under high pressure. *Physical Review*, **B 73**, 134103. 4, 17

Wyckoff, R.W.G. (1982). *Crystal sturctures,* 2nd edn., vol. 1. Interscience Publisher, New York. 17

Zhang, S.B. & Northrup, J.E. (1991). Chemical-potential dependence of defect formation energies in GaAs: Application to Ga self-diffusion. *Physical Review Letters*, **67**, 2339–2342. 62

Eidesstattliche Erklärung

Hiermit erkläre ich an Eides Statt, daß ich die vorliegende Dissertation selbständig verfaßt, keine anderen als die angegebenen Hilfsmittel verwendet und noch keinen Promotionsversuch unternommen habe.

Osnabrück, den 5. February 2007

Shi Hongting